EVALUATION AND QUANITIFICATION OF OPTIC FIBER DISTRIBUTED SENSOR RESPONSE IN AIR AND WATER ENVIRONMENTS

A Dissertation

by

DAVID MICHAEL HOLLER

Submitted to the Office of Graduate and Professional Studies of
Texas A&M University
in partial fulfillment of the requirements for the degree of

DOCTOR OF PHILOSOPHY

Co-Chair of Committee,	Yassin Hassan
Co-Chair of Committee,	Rodolfo Vaghetto
Committee Members,	Maria King
	William Marlow
Head of Department,	John Hurtado

August 2019

Major Subject: Nuclear Engineering

Copyright 2019 David Michael Holler

ABSTRACT

Dense and accurate experimental data are continuously sought after, especially for validation of computer codes. Codes can often produce dense calculations, and need equally dense experimental results for comparison. Optic fiber distributed sensors can provide the dense and accurate data desired. While this sensing technology is mature, the responses of these sensors need to be fully characterized for all experimental conditions.

This study performed multiple analyses and experimentation with optic fiber distributed temperature sensors (DTS) in air and water environments. Multiple correction curves and calibration efforts were undertaken in order to quantify the response of DTS in these environments. Uncertainty was estimated for a common type of DTS installation, which can be applied to many experiments.

The cooling panel temperature profile in a 1:23 scale Water-cooled Reactor Cavity Cooling System (WRCCS) was measured with optic fiber DTS. The temperature profile of a riser (water) column was also investigated, during both steady and transient conditions. Fiber DTS were installed in the upper plenum of a 1:16 scale High-Temperature Gas-cooled Reactor (HTGR) facility. Sensor response and boiling detection analyses were performed in a simple boiling apparatus, and may lead to future refined efforts towards boiling detection with distributed optic fiber DTS.

Optic fiber DTS are capable of producing high-resolution data in a multitude of applications. Since the fiber and coating used are inert to air and water, almost any environment within coating temperature limits can be investigated. The most severe limitations are from the fiber, its hygroscopic coating (polyimide), and the sensor installation efforts required. Isolation from mechanical strain must be achieved when taking Rayleigh backscatter DTS measurements. Fiber coating effects also must also be accounted for, especially for hygroscopic coatings such as polyimide.

ACKNOWLEDGMENTS

Many thanks to the committee members, Drs. Yassin Hassan, Rodolfo Vaghetto, William Marlow, and Maria King. Thank you to Special Appointment Dr. Darius Lisowski for his mentoring during an internship at Argonne National Laboratory and throughout my doctoral studies. The mentoring and education received is irreplaceable. Thanks also to Drs. Steve Lomperski and Craig Gerardi and to the support staffs at LUNA Technologies, OFS Optics, and FiberOptic.com for their help and expertise. Finally, thank you to my family and friends for their continued, unrelenting support.

CONTRIBUTORS AND FUNDING SOURCES

Contributors

This work was supported by a dissertation committee consisting of: Professor Yassin Hassan, Assistant Research Professor Rodolfo Vaghetto, and Professor Emeritus William Marlow of the Department of Nuclear Engineering; and Research Associate Professor Maria King of the Department of Biological and Agricultural Engineering. Darius Lisowski, Special Appointment and Reactor Safety Testing Analysis Section Manager of Argonne National Laboratory, also supported this work and maintained an advisory role.

Funding Sources

The majority of student funding was provided by teaching and research assistant appointments from Texas A&M University. The latter type was supported under the U.S. Department of Energy Nuclear Engineering University Program, Project Number DE-NE0008552.

The remainder of student funding and research data was provided during an internship at the Argonne National Laboratory, managed by UChicago Argonne, LLC. Argonne is a U.S. Department of Energy Office of Science laboratory, operated under Contract No. DE-AC02-06CH11357.

NOMENCLATURE

Acronyms

DI	De-ionized
DTS	Distributed Temperature Sensor
DUT	Device Under Test
EMI	Electro-Magnetic Interference
FBG	Fiber Bragg Grating
FEA	Finite Element Analysis
FMCW	Frequency Modulated Continuous Wave
FSI	Flow-Structure Interaction
HTGR	High-Temperature Gas-Cooled Reactor
LDA	Laser-Doppler Anemometry
LIF	Laser Induced Fluorescence
LWR	Light Water Reactor
MSIF	Multi-mode Step Index Fiber
NA	Numerical Aperture
NI	National Instruments
NPT	National Pipe Taper
ODiSI	Optical Distributed Sensor Interrogator
OM	Order of Magnitude
OFDR	Optical Frequency Domain Reflectometry
OTDR	Optical Time Domain Reflectometry
PIV	Particle Image Velocimetry
PTFE	Poly-Tetra-Fluoro-Ethylene
RCCS	Reactor Cavity Cooling System
RH	Relative Humidity
RTD	Resistance Temperature Detector
RW	Regular Wall
SC	Signal Conditioner
SCXI	Signal Conditioning EXtensions for Instrumentation
SMF	Single-Mode Fiber
SMR	Small Modular Reactor
SOC	Splice-On Connector
SS	Stainless Steel
SWI	Swept Wavelength Interferometry
TC	Thermocouple
TLS	Tunable Laser Source
UV	Ultra-Violet
VI	Virtual Instrument

Symbols

n	Refractive Index
ϵ	Strain
θ, ϕ	Incident Angles
λ_B	Bragg Wavelength
Λ	Grating Period
I	Intensity
α	Polarizability
ω	Optical Signal Frequency
τ	Signal Time Delay
K_T	Temperature Coefficient
K_ϵ	Strain Coefficient

Subscripts

$ref.$	Reference
$rep.$	Repeatability

TABLE OF CONTENTS

Page

LIST OF FIGURES

LIST OF TABLES

TABLE Page

1. INTRODUCTION

Optic fiber was developed in response to a growing demand for a medium that could transmit light signals. Higher speeds and bandwidths were known to be possible with light signals, but a transmission medium with an acceptable attenuation did not exist until 1970. The attenuation of optic fiber had to be less than or equal to 20 decibels per kilometer. This corresponds to a signal loss of 99% after 1 km, which was the current equivalent in copper wire telephone lines. Since then, optic fiber has been improved to the point where attenuations of 0.25 decibels per kilometer are achievable.

1.1 Optic Fiber

Optic fibers transmit light signals via total internal reflection. The signal is reflected (and refracted, resulting in losses) at the interface of the core and cladding. Fig. 1.1 illustrates the light path in an optic fiber due to total internal reflection. The single-mode fiber (SMF) used in this work has a core diameter of 4.6 μm, while the cladding and coating have outer diameters of 125 μm and 155 μm, respectively.

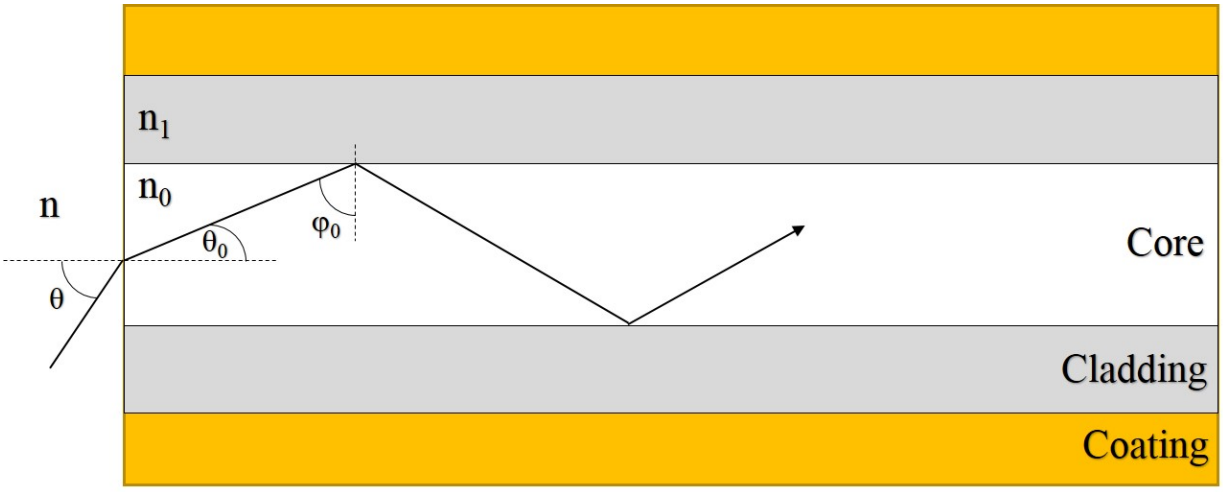

Figure 1.1: Light path in optic fiber. Not to scale.

Snell's law of refraction (Eq. 1.1) governs the path of light as it passes from one medium to another. Indices of refraction (n) and incident angles (θ, ϕ) are labeled. A light path such as the one in Fig. 1.2 can occur when two criteria are met: $n_0 > n_1$ and $\phi_0 > \phi_c$. This last parameter, ϕ_c, is the critical angle of the interface for two adjacent mediums with different indices of refraction. The critical angle is dependent upon the value of both refraction indices.

$$\begin{aligned} nsin\theta &= n_0 sin\theta_0 \\ &= n_0 sin\left(\tfrac{\pi}{2}\right) \\ &= n_0\sqrt{1-(n_1-n_0)^2} \\ &= \sqrt{{n_0}^2-{n_1}^2} \end{aligned} \tag{1.1}$$

The final term in Eq. 1.1 is also known as numerical aperture, or NA. The use of NA in industry simplifies the classification and selection of optic fibers. According to Krohn et al [1], the value of NA is directly related to the amount of light an optic fiber can collect. Large values of NA and core diameter give fibers the highest light-collection efficiency. The SMF proposed for the current study has an NA of 0.21.

1.2 Advantages of Optic Fiber

Optic fiber has several key advantages over metal wire, and most of them are due to the inherent properties of the fiber itself.

Transmission speed, size, and weight are the main advantages of optic fiber. These advantages would have the largest impact on their most common usage, which is general communication. Speeds of 40 gigabits per second (Gbps) are commonplace today and will only increase in the future. Large diameter copper wires can achieve these speeds, but the high cost of copper prevents this from happening. The requirement of large copper cable for high speed transmission highlights the size and weight advantage of optic fiber.

Interference resistance is another key advantage of optic fibers. Since the carried signal is made of neutral photons, it is not changed by any electric or magnetic fields near the cable. Silica is also a poor electrical conductor, so any intruding electric signals would have difficulty reaching the core

of the fiber. Optic fiber is also resistant to radiation, but the effects of strong ionizing radiation are not fully understood.

Security of transmission lines is paramount for many applications. Standard copper wire can be easily infiltrated by crossing the wire with another of matching impedance. However, it is currently impossible to splice into an optic fiber cable without detection. A change in the original transmission medium causes an easily detectable change in the signal at its destination. Non-security issues such as fiber cable breaks or failures are also detectable. This ability to detect changes along a fiber led to its usage as a platform for distributed sensing.

1.3 Applications of Distributed Fiber Optic Sensors

Various industries have incorporated distributed fiber optic sensors, including the petroleum, civil, aerospace, and energy sectors. The sensing techniques are dominated by Raman and Brillouin scattering, which allow long-distance measurements. Sensors of 30 km or greater can be interrogated for temperature and / or strain, depending on application. Long sensors are preferable in large-scale applications, where global measurements are more meaningful. Undersea applications have been developed with distributed temperature and acoustic measurement techniques.

Petroleum applications of distributed fiber optic sensors are dominated by bore hole measurements, but other useful applications exist as well. The down hole temperature profile influences the required viscosity of drilling mud for efficient crude oil extraction. Since space is very limited in a bore hole, the size and weight of fiber sensors are also beneficial.

Civil structures such as bridges undergo a great deal of analysis and testing to confirm their safety, and strain measurements are a key part of that analysis. Distributed fiber sensors offer their inherent size and weight advantage to civil applications, but also offer simplicity when compared to the use of conventional strain gauges. Hundreds, if not thousands of strain gauges would be needed to provide the same resolution as a distributed fiber sensor. Each strain gauge also has to be wired to the data acquisition unit, but the optic fiber is only one cable. One interrogation unit and one fiber sensor are typically used in civil applications. This is far simpler to implement than thousands of strain gauges.

Large aircraft and their components also benefit from the use long, continuous sensors. Distributed strain measurement of metal components remains a critical application of optic fiber sensors. These sensors benefit the aerospace industry in much the same way as the civil engineering sector, in that they provide efficient and high-resolution strain profiles of large components. Aerospace applications are typically much smaller than civil structures, and different photon scattering mechanisms can be used to take measurements.

The energy sector applications of distributed fiber optic sensors include almost every means of energy production. Notable applications include global temperature profiles of power plants and geothermal wells. Efforts towards leak detection with distributed fiber sensors have also been made and show the potential of these sensors to detect other parameters than temperature or strain.

The short distance techniques described in the current study are more specialized, and have a smaller user base. Since sensor length is restricted to 20 meters (50 meters for some systems), complete measurement of a large structure such as an oil well is not possible. However, small scale experiments, i.e. the facilities in the Texas A&M Thermal Hydraulics Research Laboratory, can benefit from the high-resolution measurements offered by the proposed short-distance techniques.

2. MOTIVATION FOR RESEARCH

Several motivations exist for the development of distributed optic fiber sensors. Most of the motivations described rely on the physical properties and sensing characteristics of these sensors.

2.1 Statistical Characterization of Data Population

Highly-detailed, high-resolution experimental results are always sought after, regardless of application or field of study. Public opinion polls, medical studies, and laboratory experiments all benefit from large data populations. Some laboratory experiments can benefit from efficient method design, but they require well-developed and understood techniques.

One reason to obtain as many measurements as possible is to fully characterize the statistical distribution of the data. Figure 2.1 shows a logarithmic distribution of random numbers alongside the student's t-distribution, and both are compared to the normal distribution of the data. The scales are arbitrary, and ν denotes the degrees of freedom in the student's t-distribution.

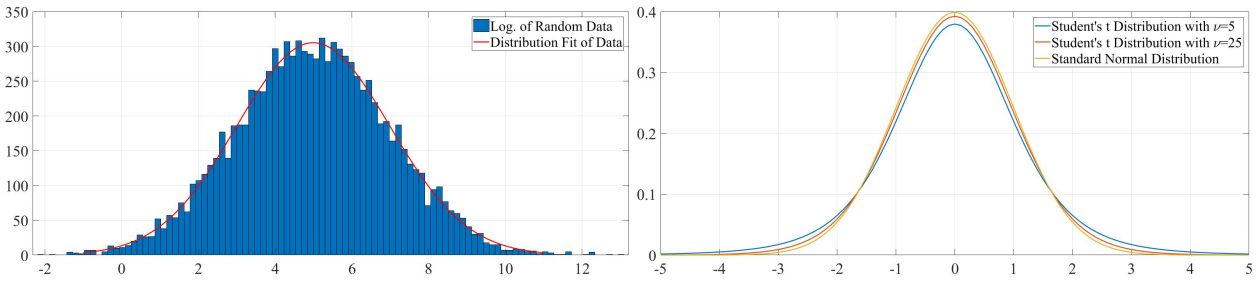

(a) (b)

Figure 2.1: Logarithmic distribution of random numbers (a) and student's t-distribution for ν=5 and 25.

The importance of complete data population collection is highlighted in these two plots. Missing data affects the calculation of the mean and other statistical parameters, which define the data population. Advanced measurement techniques can collect these complete data populations, especially

if they have high sampling rates and high spatial resolution. Optic fiber distributed sensors can provide accurate, high-resolution strain and temperature data that is otherwise unavailable using conventional techniques. This data can be spatially and temporally dense, with sensing point linear densities of up to 1600 m^{-1} and sampling rates up to 250 Hz. These resolutions are not possible with conventional strain and temperature sensors, i.e. strain gauges and thermocouples. Not only do high-resolution data provide more detail about the phenomena occurring during an experiment, they are useful for validation exercises as well.

2.2 Restrictive Environments

Optic fiber is inherently useful for both extrinsic and intrinsic measurement purposes. The small diameter and weight of optic fiber are advantageous over larger, heavier sensors made from other materials. The fiber itself is strong in the axial direction; the product used for this work was proofed to 100 kpsi (689 MPa). The fiber is weak in the radial direction, but flexible coating (such as the polyimide coating used in this work) and additional barriers address that concern.

High-temperature environments often require specific instrumentation. Optic fiber is usable in temperatures up to $\sim$650°C, where the signal degradation becomes the major limiting factor. The melting point of fused silica is well over 1000°C, but the sensor would become useless after signal degradation.

Optic fiber is also immune to electromagnetic interference (EMI), making it a prime candidate for use in noisy environments. However, the interrogation hardware must be isolated from noisy environmnents, since it relies on traditional electronic technology.

3. RESEARCH OBJECTIVES

This study has three main objectives:

1. *Measure and quantify fiber response to air and water environments.*

   All sensing techniques require calibration to reference measurements, and fiber DTS are no exception. The only reason for DTS calibration stems from the fiber coating used. The polyimide coating used for the sensors in this study is sensitive to heat cycling and humidity. Separate effects tests must be performed for both temperature and humidity when these fibers are used. Bare fibers do not require calibration, but it is still suggested for completeness.

2. *Perform temperature measurements in current facilities.*

   While many of the facilities in the Texas A&M Thermal Hydraulics Lab are already instrumented with high-resolution measurement equipment, fiber DTS can still benefit each facility (provided DTS installation is practical). In particular, the Water-cooled Reactor Cavity Cooling System (WRCCS) and the High-Temperature Gas-cooled Reactor (HTGR) Upper Plenum facilities would both benefit from use of fiber DTS. All heated experiments would benefit from the reliability and robustness of fiber DTS. Any isothermal experiments that involve flow-structure interaction (FSI) would benefit from the high-resolution strain measurements that fibers can provide.

3. *Expand sensing capability to other parameters.*

   Air and water environments are well-understood and relatively predictable, but two-phase environments tend to be more chaotic. A variety of sensing techniques are available for two-phase investigations, but they are either low-resolution (mesh sensors, probes) or require transparent enclosures (cameras). Distributed fiber sensors can provide high-resolution strain and temperature measurements in opaque or remote environments that are impractical for other methods. The current study aims to apply distributed sensors to two-phase conditions

and determine the feasibility of this approach. This environment will be achieved with a simple heated pipe apparatus.

4. LITERATURE REVIEW

4.1 Distributed Fiber Optic Sensing

Optic fibers were first recognized as promising future sensors nearly 50 years ago [2]. Fiber optic sensors (FOS) have been reviewed [3, 4, 5, 6, 7, 8, 9, 10, 11, 12, 13, 14, 15, 16, 17, 18, 19, 20] and developed ever since. Experiments with fiber sensors were conducted [21, 22, 23] which led to developments in single-point fiber sensors [24, 25]. These sensors used interferometry techniques developed around the same time [26, 27]. The extrinsic sensors described by these authors led to the development of distributed intrinsic sensors, which are the focus of the current study.

One of the earliest DTS experiments was performed by Hartog [28]. The author used optical time domain reflectometry (OTDR) to estimate the Rayleigh backscatter sensitivity of liquid core fibers under thermal strain. Hartog achieved a temperature senstivity of 0.023 dB / °C, and a spatial resolution of 1 meter. The author also reported an accuracy of 1°C, which was based on the signal-to-noise ratio of the DTS used. This value is unusually low, especially for fibers with polyimide coatings.

Dakin et al [29] conducted experiments with Raman distributed temperature sensors using a similar OTDR technique. Measurement resolution was quite low; spatial resolution was 3 meters and temperature resolution was 10°C. However, the scope of this study was to show the efficacy of a new semiconductor laser and its use in distributed fiber measurement techniques.

Stierlin et al [30] conducted another early study with Raman DTS. The focus of this study was long-range monitoring of optic fiber cables, which is what most Raman sensors are used for to this day. The temporal resolution obtained in this study was between 1 and 3 minutes, while the temperature resolution was 1 - 4°C. Spatial resolution was as low as 0.1 meters. These values are of the same magnitude as their modern counterparts.

Juskaitis et al [31] used a frequency-modulated continuous-wave (FMCW) approach, resulting in a spatial resolution of 0.7 meters. This approach is based on Rayleigh backscatter, but analyzed

in a different way than other methods. At the time, optical interrogation hardware that used the time delay within a fiber to detect perturbations was too noisy, so these authors selected the FMCW technique. This technique reduces the required signal processing load, but with modern electronics it is not necessary.

Horiguchi et al [32] developed two distributed fiber sensors using Brillouin backscatter. One sensor was evaluated using optical time domain analysis (OTDA), while the other used a modified coherent OTDR method. The objective of this study was to develop Brillouin scattering based sensors with common, unmodified optic fiber. The authors achieved a spatial resolution of 100 meters in each sensor type. Each sensor had strain accuracies of $\pm 1.5 \text{x} 10^{-4} \epsilon$ and $\pm 6 \text{x} 10^{-5} \epsilon$, respectively. It is unclear whether these values represent true accuracy or resolution. Modern systems have resolutions a few orders of magnitude better than these values.

Distributed sensors have also found use in acoustic measurements. Kurmer et al [33] developed a Sagnac interferometer for the purpose of leak detection via acoustic waves. The authors successfully demonstrated this concept with a hydrophone in a 1-meter drum, where the sensor displayed a sensitivity of 20 dB per order of magnitude of acoustic pressure. These authors also propose that this sensitivity justifies the application of this sensor concept to pipelines in an effort towards leak detection.

Much like Horiguchi et al [32], Bao et al [34] also developed a Brillouin scattering-based distributed sensor for long-range applications. This sensor was a 22-kilometer long fiber sensor with strain and temperature resolutions of 20 $\mu\epsilon$ and 2°C, respectively. Spatial resolution was approximately 5 meters. The authors also contributed some of the earliest arguments towards the separation of mechanical and thermal strain, both of which contribute to a total strain measurement via Brillouin backscatter. This argument is also valid for all studies involving Rayleigh backscatter-based measurements, including the current study.

Rathod et al [35] continued previous work on Rayleigh backscatter-based measurements [31] by subjecting a distributed fiber sensor to a finely-controlled environment. These authors achieved a much higher spatial resolution, which was better than 0.15 m. Temporalt temperature sensitivity

was measured at 0.014 K/s, but the authors were unclear about fiber installation. The fiber was likely installed loosely to minimize any mechanical strain effects.

Gambing and Hartog [36] developed an ultra-long range Raman backscatter fiber sensor, which proved to be useful in commercial applications. The authors successfully deployed their 10-kilometer DTS in several applications, and achieved an accuracy of 0.3°C. Since Raman scattering can be interrogated for thermal strain only, this accuracy is likely true.

Hurtig et al [37] also developed a Raman backscatter-based DTS, but focused on borehole applications. The authors successfully logged temperature along a borehole during static and dynamic conditions and compare them with high-precision borehole temperature measurements. Temporal and spatial resolutions of 1 minute and 1 meter were available, and are quite sufficient for boreholes that are hundreds of meters deep.

Fiber Bragg grating (FBG) sensors can offer high-resolution measurements, but are inherently quasi-distributed due to their imposed sensing points. Froggatt and Moore [38] developed a 1.75 meter FBG sensor with 2.7 cm-gage gratings. The response from the fiber sensor were confirmed with foil strain gauges, but the authors note several possible sources of error, including fiber material properties. The hardware at the time of this study limited FBG sensors to static measurements.

Lawrence et al [39] also developed a FBG sensor, and used two sensors with 5 mm spatial resolutions to measure strain in two directions. The authors also found good agreement between finite element analysis (FEA) and their results, further justifying the use of FBG sensors for high-resolution measurements.

A study by Sakaguchi [40] investigated Rayleigh scattering loss in optic fiber, but not specifically for measurement purposes. This author investigated the time-dependent effects of high-temperature (>1000°C) heat treatment on optic fiber, and found that Rayleigh scattering could be reduced by up to 15%. This finding may not be directly applicable to current fiber production techniques, but the initial heat-cycle effect will be shown and discussed in the current work.

De Souza and Newson [41] improved a Brillouin scattering-based sensor by implementing an optical preamplifier system, while keeping the sensor at a long length (23 kilometers). The authors

also achieved spatial and temporal resolutions of 1.8 meters and 9 minutes, respectively.

Kimura et al [42] investigated the effects of radiation on a Raman DTS installed in a fast nuclear reactor facility. The fiber received a dose of more than 7.7 x 10^3 C / kg (3.0 x 10^7R), which the author notes is close to the operational lifetime dose in a light water reactor system. The fiber error due to radiation also displayed saturation, which allowed a correction to be applied.

Kher et al [43] also developed a Raman scattering-based DTS. The authors achieved theoretical spatial and temperature resolutions of 8.5 m and 4°C, respectively, which were below commercially available systems at the time. However, the authors proved that a capable system could be developed without using commercially available sensing equipment.

Leak detection is an application that holds a great deal of potential for distributed fiber sensors. MacLean et al [44] successfully designed and tested a chemical sensor which employed a distributed fiber sensor. The authors used OTDR to confirm the presence of chemicals at specific points along the fiber. This technique was made possible by using a fiber coating that swelled when exposed to certain chemicals. The resulting decrease in backscatter in the fiber was obvious in the results presented.

Another application of leak detection with distributed fiber sensors was described by Weiss et al [45]. In this study, the authors installed a Raman DTS on the perimeter of a waste landfill site. The fact that dry and wet soil have different thermal conductivities justified this temperature measurement as leak detection, but also required the sensor to have a sufficient time response. Ultimately, the authors resolved water moisture changes above approximately 6%.

Raman scattering and FBG sensors have the distinct advantage of being potentially insensitive to temperature, which is not the case for Rayleigh and Brillouin scattering. Zhu et al [46] exploited this phenomena and developed a temperature-insensitive FBG sensor. The authors used a chirped laser and evaluated the signal packet width as it passed through the sensor. This yielded a separation of mechanical and thermal strain signals.

High-temperature applications of distributed sensing continue to be investigated and published. Lee et al [47] developed a FBG sensor using sapphire fiber, which can withstand temperatures up to

2000°C. This sensor was designed to monitor a boiler's temperature distribution, which can also give insight to the emissions being produced from combustion. Still, a sensor like this is not a common glass fiber and may not be economical.

Soller et al [48] developed an OFDR system capable of evaluating fiber sensors in the tens to hundreds of meters-long range. The authors took advantage of recent improvements in communication and data acquisition technology, and developed a sensing system that is similar to the system used in the current study.

Stoddart et al [49] investigated the aging effects of a DTS by evaluating both the Raman and Rayleigh backscatter in a heat cycled fiber. A short section of the fiber sensor was heated to approximately 290°C to study these aging effects, and the authors determined that their methods were insufficient to fully quantify aging of optical fiber. However, the authors did identify phenomena that must be accounted for when using glass fiber DTS, especially in high-temperature cycling applications.

Distributed chemical sensing with optic fibers continues to be investigated. Instead of using a reactive coating, Caron et al [50] manufactured an optic fiber with a capillary hole in the cladding, near the fiber core. The authors developed a technique to interrogate this fiber to determine the position of chemical droplets in this capillary hole. The eventual goal of this study was to determine chemical composition of droplets within the fiber. This type of sensor could then be used to determine the positions of chemical layers in separation processes such as gas chromatography.

Yuan and Yang [51] investigated techniques for embedding FBG sensors into concrete structures. These "smart structures" are attractive solutions for strain monitoring, because embedded sensors can provide measurements from within the material. The authors also developed this system to be passive, which would greatly reduce the cost by not requiring the use of a light source.

Train rails are also important structures that could benefit from strain monitoring. Fan et al [52] developed a methodology for measuring the strain on the underside of a rail using grating-based fiber sensors. While not distributed sensors, this application demonstrates the usefulness of fiber strain sensors. The authors also reported that these measurements could shed light on wheel symmetry,

which subsequently affects rail lifetime.

Matta et al [53] also applied distributed fiber sensing to a civil structure for strain monitoring. The authors installed a 1.16 km long Brillouin scattering-based sensor on the girders of a bridge. This sensor returned strain and displacement measurements. The results also confirmed that strain levels were well below the design limit.

Sang et al [54] performed high-resolution fiber measurements in a nuclear reactor environment. The goal of this study was to perform temperature measurements, but the authors also quantified radiation effects on the fiber sensors. Several different fibers - which vary mostly by material composition - were evaluated in a high-radiation environment. The authors found a direct relationship between neutron fluence and spectral shift within the fiber. Temperature effects were also observed, but the spectral shifts were inversely related to changes in temperature.

Fiber reliability during testing is paramount for reliable measurements to take place. Stolov et al [55] investigated the thermal stability of several different optic fibers under heat and strain cycling. The authors identified three criteria of the most importance for determining fiber stability, two of which are independent. Failure criterion and continuous use time were found to be independent, while a fiber's upper use temperature could be determined using the two independent criteria.

Similar to Soller et al [48], Dai et al [56] developed a mid-range distributed fiber sensor using OFDR. However, the latter authors used a polarization-maintaining fiber and report a theoretical maximum sensor length of 100 km. A spatial resolution of 5 cm is reported, but the results sugggest that this is a conservative value.

Feng et al [57] investigated the use of fiber optic sensors to determine the coefficient of thermal expansion (CTE) of a material. This fundamental material property must be accurately measured in order for a non-isothermal system to perform effectively. The authors propose a correction to account for the thermo-optic and strain-optic effects that occur when fiber sensors are used.

Hsu et al [58] applied coherent Raman scattering-based methods towards measurement of reacting flows. Similar to structure monitoring, combustion measurements provide insight into a phenomena and can make system designs more effective. The authors of this study developed a

complete measurement system and characterized a multitude of fiber types for use in combustion environments. The results show 100% silica multimode step-index fibers (MSIFs) provide the highest efficiency for these measurements and were authors' overall fiber choice.

Another study towards structural health monitoring by Liehr and Krebber [59] showed the ability of FBG sensors to detect displacement. The authors used a simple cantilever beam experiment to show the practicality of their sensors, but the presented results seem to have a significant level of noise. There was also no uncertainty quantification in this study, but the accuracy of displacement measurements in a simple experiment like this can be easily confirmed.

Reinsch and Henninges [60] characterized a selection of commercially-available fibers for use in geothermal well monitoring. According to the authors, "temperature is a key parameter in understanding fundamental processes within a wellbore" [60]. This study had a specific application goal, but shed light on heat-cycling effects on different fiber coatings. Polyimide was reported to be the most stable coating, especially in an inert atmosphere.

A study by Kasinathan et al [61] investigated the behavior of Raman DTS in a sodium leak experiment. Leak monitoring is especially important when liquid metals are involved due to their high temperatures and chemical reactions outside their intended environments. The authors of this study built a simple test stand that purposely imposed a leak of liquid sodium into the insulation around a steel pipe. The presented results show expected behavior of a deliberate high-temperature leak, but more importantly provide proof of the applicability of DTS for liquid sodium leak monitoring. A later study by Kasinathan et al [62] investigated the same topic but with more developed techniques. More recently, another study by Kasinathan et al [63] further developed the previous leak-detection methods but used water instead of sodium.

Wylie et al [64] developed a Brillouin OTDR-based displacement sensor and a supplementary method for structure shape reconstruction. The fiber sensing technique devloped displayed insensitivity to temperature, removing the requirement of temperature correction. The authors also reported a displacement error of 45 cm, which is simply too large for quantitative measurements to considered accurate.

Lomperski et al [65] performed a preliminary study to measure jet temperatures with Rayleigh scattering-based DTS. These sensors were interrogated in a similar manner to those in the current study, but with a previous interrogator model by LUNA Technologies. The authors reported trade-offs between vibration / noise reduction and temperature measurement accuracy, along with an uncertainty related to the temperature coefficient K_T used in LUNA DTS systems. A later study by the same authors [66] provided complete results from DTS measurements of air jets, along with a practical approach to uncertainty quantification in polyimide-coated DTS. The DTS data were presented alongside PIV and thermal-imaging results, further characterizing the two-jet apparatus used for experimentation.

Mirzaei et al [67] published an extensive study describing the heat transfer and distributed temperature measurement for oil pipelines. The authors used numerical predictions to influence experiment design, and characterized system response to small leaks. Actual leaks would lead to much shorter time responses, which the authors state are within the sensing abilities of both Raman and Brillouin scattering-based sensing techniques.

Wang et al [68] developed a technique to amplify and evaluate Raman scattering in fiber sensors. The authors calibrated their sensor in an oven, and deployed a 2-kilometer sensor into an oil well. While Raman DTS typically have low spatial resolution, this sensor was able to resolve inclined wells present in the main vertical well. The inclined wells were indicated by increases in temperature along the DTS.

Similar to a previous study on optic fiber stability by Reinsch and Henninges [60], Wood et al [69] and Lisowski et al [70] performed further studies on the heat cycling stabilities of different fiber types. The former studied fewer types of fiber during heat cycles up to 1000°C, and provided insight into practical limitations of these fibers in high-temperature environments. The latter of these studies investigated heat cycling at lower temperatures (up to $\sim$600°C) but provided data on more types of fiber coatings. The interrogation units used in both of these studies were manufactured by LUNA Technologies, limiting these studies to single mode fibers (SMFs) only. Polyimide-coated fibers were once again shown to be the most stable during cycling, provided the maximum temperatures

do not go above the limits of the polymer itself. Uncoated, bare glass fibers displayed the best stability, but are extremely fragile and impractical for most applications.

Jin et al [71] studied the performance of irradiated optic fiber DTS. These fibers are unique since they are irradiated before use, as opposed to previous studies that quantified radiation effects on standard fiber. Irradiated fiber contains more absorption bands than standard fiber, likely due to radiation damage. The authors reported a low spatial resolution with the fiber they tested, but acknowledge better resolutions and accuracies could be accomplished.

Xu et al [72] evaluated the strain of a full-scale bridge with both Brillouin and Raman scattering-based DTS. The Brillouin DTS was deployed to capture relatively high-resolution strain measurements (0.05 m), and the Raman DTS was added to provide temperature compensation data. The authors loaded the bridge with trucks in two different configurations, demonstrating the practicality of dense strain measurements of large structures.

Similar to Yuan and Yang [51], Hoff [73] developed a passive optic fiber for distributed sensing applications. In this case, however, the author applied this technique to rollers and conveyor belts in an effort to detect hot spots and potential fire hazards. While this study did not go into detail about sensing theory, it did provide preliminary results from a few different fiber configurations. Thermal imaging and acoustic sensing results were also presented, furthering the case for temperature monitoring of conveyor belt systems.

One of the most recent Rayleigh DTS studies was performed by Lomperski et al [74]. This study measured the 3-dimensional temperature profile of a wire-wrapped tube bundle, which was a scale model of a nuclear fuel bundle. Uncertainty estimation was not presented, but the scope of this study was feasibility and design verification. The installation of Rayleigh based-DTS continues to be a challenge, and this challenge was addressed by the authors in this unique study.

Liquid level measurement is another feasible technique for distributed sensors, as shown by Gerardi et al [75]. This study deployed bare optic fiber into liquid sodium, and successfully measured the liquid level. The liquid level measurement was indicated by a sharp gradient in temperature between the sodium and its cover gas, which is injected at a slightly different temperature. This

study highlights the usefulness of distributed sensors for other parameters than temperature or strain.

Ringel et al [76] investigated the effects of a high-voltage environment on FGB sensors. The authors also included Rayleigh scattering loss measurements. While the fiber survived these harsh conditions, the authors found the grating temperature measurements to be unreliable.

A study by Thomas and Hellevang [77] quantified the strain response of polyimide-coated DTS to humidity. The authors reported a sensitivity of 1.3$\mu\epsilon$ / %RH, which is a relatively small value but must still be accounted for when using polyimide-coated fibers. This strain sensitivity could be converted to a temperature sensitivity (°C / %RH).

Nixon et al [78] studied the effects of fluid-structure interaction in an wire-wrapped tube bundle with distributed strain measurements. The authors installed optic fiber on the walls of the tubes, and subjected the bundle to various flow conditions. These experiments were required to be isothermal, however, because the hardware involved (LUNA ODiSI-B) interrogates sensors via their Rayleigh backscatter.

4.2 Natural Convection and Circulation

The passive heat removal capabilities of natural convection and circulation are desirable in many applications, ranging from building design to electronics to renewable energy. A recent study by Liu et al [79] describes the characterization and optimization of a hybrid solar wall, which uses use the chimney effect to remove heat. Heat removal in walls via heat pipes has also been studied [80, 81, 82, 83]. These studies demonstrate the improvements that internally-piped walls can offer, which use natural convection to improve their heat transfer characteristics.

Natural convection in heated cavities is another widely studied topic, and has been reviewed extensively by Khalifa [84] and Bairi et al [85]. Both of these articles describe results and heat transfer correlations. The former is focused on building applications, and the latter is more fundamental and includes a few numerical investigations. Several authors have also conducted heated cavity experiments. Karatas and Derbentli [86, 87] have published two similar experimental studies on the heat transfer within adiabatic cavities. These two studies discuss different characteristics but both had Rayleigh number ranges between 1 x 10^5 and 5 x 10^7. Lewandowski et al [88] also investigated

a heated cavity, but with a high-resolution thermal camera. Another study by Lewandowski et al [89] involved similar methods, but included heat transfer coefficient calculations. These heated cavity studies all highlight the importance of cavity design in natural convection systems.

Natural circulation loop testing is especially important for applications that may require more careful loop design, and can be made to remove heat from a wide variety of systems. Yamaguchi et al [90] and Sadhu et al [91] performed studies on supercritical CO_2 in a passive loop to study coolant behavior. While the former study did not explicitly classify or promote their experiment as a natural circulation loop, their loop was still passively exchanging heat and can be considered a natural circulation loop. Supercritical CO_2 can be relatively complex to control, but its properties can improve heat cycles.

Power production is a particularly useful application of natural circulation loops. A numerical optimization study by Thalange et al [92] predicted the behavior of a natural circulation molten salt loop in solar power production. The authors showed that highly-concentrated solar radiation can be used to heat a natural circulation loop of molten salt, which would allow high-temperature co-generation processes to take place simultaneously.

Nuclear fusion systems can incorporate natural circulation systems for both heat removal and radiation shielding. An experimental study by Bao et al [93] investigated a square-channel natural circulation loop for nuclear fusion applications. This system represents a "blanket" of vertical square channels that contain water and manage the heat from a fusion reactor. The authors also note that this water system is important for shielding neutrons. Fusion reactions achieved with deuterium-tritium fuel produce streams of 14-MeV neutrons, which must be shielded. Any materials in the path of these neutrons are at risk of activation and structure defects.

Molten salts have shown great potential as coolants for several applications, including nuclear fission power. In particular, the natural convection & circulation characteristics are of interest but require a large amount of experimentation. Some of the earliest publications on molten salts by Briant and Weinberg [94] and Weinberg [95] provide details about this fluid. Continued work on the natural convection characteristics continues to be performed by Yoder et al [96] and Britsche et

al [97]. Both authors developed natural circulation molten salt loops for separate objectives, but nonetheless proved the feasibility of molten salt heat transfer. Other studies worth noting include those by Kudariyawar et al [98] and Srivastava et al [99], which both performed numerical and experimental analysis of natural circulation molten salt loops. Yang et al [100] investigated a thimble-type heat transfer element in a passive heat removal system, which was reported to be part of Molten Salt Reactor (MSR) system. The authors found an inverse relationship between the air gap inside this thimble and its maximum heat transfer capabilities. Chen et al [101] expanded on this idea into a full-scale passive heat removal system. This study combined a molten salt bath with water as a secondary coolant, which is representative of an actual reactor system.

Air has always been a coolant option for passive heat removal systems, and multiple studies have been published on this topic. Lisowski et al [102] published a full report of an air-cooled passive safety system, which included distributed temperature measurements of this system's plenum. Along with measurements, the authors also quantified the response of polyimide-coated fiber to relative humidity. A journal article covering similar information was also published [103].

Tompkins et al [104] also performed studies on an air cooled passive safety system, but with a specific focus on distributed fiber measurements. The authors only measured the air temperature inside the mixing plenum of their facility, but were generous in detail with their methods of filtering and uncertainty quantification.

Several studies on the air-cooled RCCS at the Texas A&M Thermal Hydraulic Laboratory have been performed. Alhashimi [105] and Sulaiman et al [106] made experimental observations and quantified temperature profiles, respectively. Frisani et al [107] performed an extensive numerical study on fluid and heat behavior in a smaller air-cooled facility.

The current study involves a water-based RCCS, on which multiple studies have already been published. Lisowski et al [108] and Vaghetto and Hassan [109] both performed studies on the single-phase behavior of separate RCCS facilities. A full report of these projects' activities was released by Corradini [110].

In addition to single-phase studies, Lisowski et al [111] published a study on the boil-off

characteristics of the facility at the University of Wisconsin-Madison. This study was unique because it included inventory (water level) measurements and structure health observations.

More recently at the Texas A&M University water RCCS facility, several studies have been published on high-resolution methods. Quintanar et al [112] and Holler et al [113] published short studies on coolant temperature profiles and plenum design, respectively. Holler et al [114] provided preliminary results of fiber DTS results of the cooling panel surface. Finally, a recent publication by Quintanar et al [115] reported PIV results of the lower manifold of this facility.

Lim et al [116] published a study on a water-cooled RCCS, but suggest a different facility configuration. Instead of one type of coolant in vertical pipes surrounding the reactor cavity, these authors suggest using a combination of these with a water jacket to increase heat transfer from the reactor cavity. The safety analysis code GAMMA+ was used to numerically study this concept, and vastly lower temperature were predicted.

4.3 Jet Impingement

Jet impingement measurements have many applications and have been published for some time. An early study by Wygnanski and Fiedler [117] used hot-wire anemometers to characterize a self-similar jet. This technique uses small probes (5μm diameter, 1-2 mm long) that return resistance measurements, which are then converted into fluid velocity measurements. This type of sensor is robust and reliable, but does not provide the dense data that advanced techniques do.

Another early study on jet measurements was conducted by Quinn and Militzer [118], where anemometer measurements were supplemented with pressure measurements from a pitot tube and transducer. The authors found good agreement with included numerical results, but could only quantitatively compare streamwise velocity and spread. At the time, those were the only fluid measurements available for comparison. Hussein et al [119] expanded on these measurements with flying hot-wire anemometry and laser-Doppler anemometry (LDA). Flying hot-wire anemometry measurements of turbulent jets continue to be prevalent, including a fairly recent study by Fellouah et al [120]. Shorty after, Ball et al [121] reviewed the experimental and numerical techniques applied to turbulent jet problems.

A similar combination of techniques was used by Welling et al [122], which also included temperature measurements due to the use of heated cylinder. This study reported measurements of a plume from a heated cylinder. The authors chose a high applied power (1,200 W) in order to produce fluid velocities that were withing the measurable range. However, such a strong heat source would have caused strong turbulence near the cylinder surface, as the authors noted. A similar study was recently conducted by Grafsronningen et al [123], where PIV was used to take measurements around a horizontal heated cylinder.

Webster et al [124] published an early study on turbulent jet measurements using the PIV and LIF techniques. Mi et al [125] continued this work with more details about the turbulent characteristics with additional PIV measurements. Other notable turbulent jet PIV studies include works by Milanovic and Hammad [126]

Horizontal impinging jets have also been studied with high-resolution techniques. Guo et al [127] performed stereoscopic PIV measurements on a horizontal jet with a specific focus on "the development of the triple-layered wall jet structure." [127]. Stereoscopic PIV has several advantages over PIV, most notably the capability to measure out-of-plane parameters. Perspective error is also minimized when two cameras are focused on the same area.

The High-Temperature Gas-cooled Reactor (HTGR) upper plenum facility at the Texas A&M University Thermal Hydraulic Research Laboratory is a 1:16 scale model of its namesake. Preliminary results of a different facility and scaling analysis were performed by McCreery and Condie [128]. The Texas A&M facility has the ability to study the behavior of up to 25 jets / plumes in its transparent plenum. McVay et al [129] performed preliminary PIV measurements in this facility with three active jets. A recent publication by Alwafi et al [130] describes a complete set of isothermal measurements made in the current jet impingement facility. The authors used time-resolved PIV to evaluate a single jet in the center of a hemispherical dome. A complete set of high-resolution results were presented along with uncertainty quantification. This type of data is extremely insightful and provided the level of detail necessary to validate high-resolution numerical techniques.

4.4 Two Phase Sensing and Measurement with Fiber Optics

Extrinsic optic fiber sensors have been used for many applications. Figure 4.1 shows two examples of extrinsic fiber sensors, where the fiber itself is merely a transmission medium. Among the first to develop this technology was Graindorge et al [131], who described the improved response of conical-end fiber sensors compared to cleaved fibers. Yan et al [132] and Berthold et al [133] published early studies on this topic. The former of these used a fluorescent dye in the test section to indicate void fraction, while the latter measured the void fraction of a small volume with un-altered fluid. Both of these studies note the importance of proper sensor calibration, which should take place in a similar geometry to the experiment.

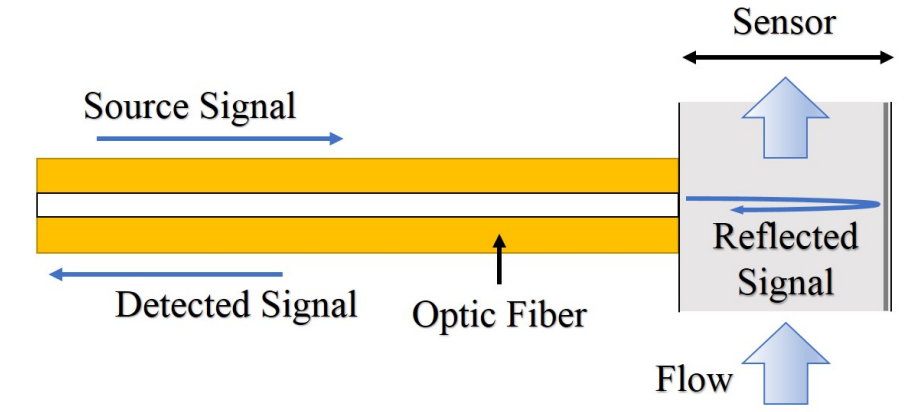

(a)

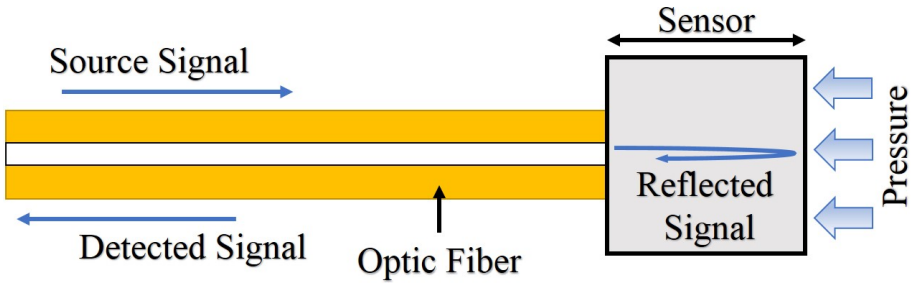

(b)

Figure 4.1: Extrinsic optic fiber sensors for two-phase (a) and pressure (b) measurements.

More recently, El-Kamash et al [134] and Rojas and Loewen [135] measured void fraction and bubble size distributions beneath breaking waves. The former study focused on stepped chutes, while the latter studied a more general breaking wave. These studies were performed in part to confirm the accuracy of previously-developed fiber probes. The authors addressed this uncertainty in accuracy by performing detailed calibrations and comparisons with previous calibration activities.

Yamada and Saito [136] developed a probe that could measure bubble characteristics and gas concentrations in the surrounding liquid. This combination of measurement abilities was achieved with a platinum-coated optical probe. The authors predicted its response and proved its feasibility, although it is not clear how reproducible this probe design is.

Delwiche et al [137] designed a rugged optic fiber probe sensor for long-term underwater use. This sensor design is unique because it can also capture gases for later analysis. The sensor was also designed to be placed in the field for long periods of time and was built from economical materials.

Microchannel two-phase flow has also been proven measureable with optical probes. Ide et al [138] developed a probe to measure two-phase characteristics in a 100μm channel, which is on the same order as optic fiber itself. Even though the experimental geometry was small, the authors were able to determine

Baroncini et al [139] performed mass flow and fluid velocity measurements by placing FBG sensors across a flow channel. The authors correlated strain measurements with standard flow measurements, and achieved reasonable comparisons between the two methods. However, the fluid velocity profile was not presented, so it is unclear whether this technology can provide this result.

A recent study by Aliyu et al [140] reported a new probe for two-phase measurement in a gas-liquid annular ejector system. The authors developed this sensor to take measurements in high bubble velocity flows, which were previously unavailable. Numerical studies were also performed on the experimental geometry, and agreed well with the optical probe results.

5. DISTRIBUTED SENSING THEORY

Optic fibers can become distributed sensors through various interrogation techniques, each having their own unique characteristics. Many hardware options are available to accomplish distributed measurements, but the specific combination of hardware and scattering mechanism used is determined by application.

5.1 Distributed Sensing with Optic Fibers

Distributed sensing interrogates the optic fiber itself as a sensor, resulting in an intrinsic sensor. The other type – extrinsic sensors – use the optic fiber for signal transmission purposes only. Figure 5.1 shows the signal path through an intrinsic optic fiber sensor. In this work, the sensor length is made from single-mode fiber (SMF). The termination is a short length (5 cm) of coreless silica fiber, which attenuates the signal due to the absence of a core. The coreless fiber has matching cladding and coating characteristics to that of the SMF. Additional information about both types of these fibers can be found in Appendix A.

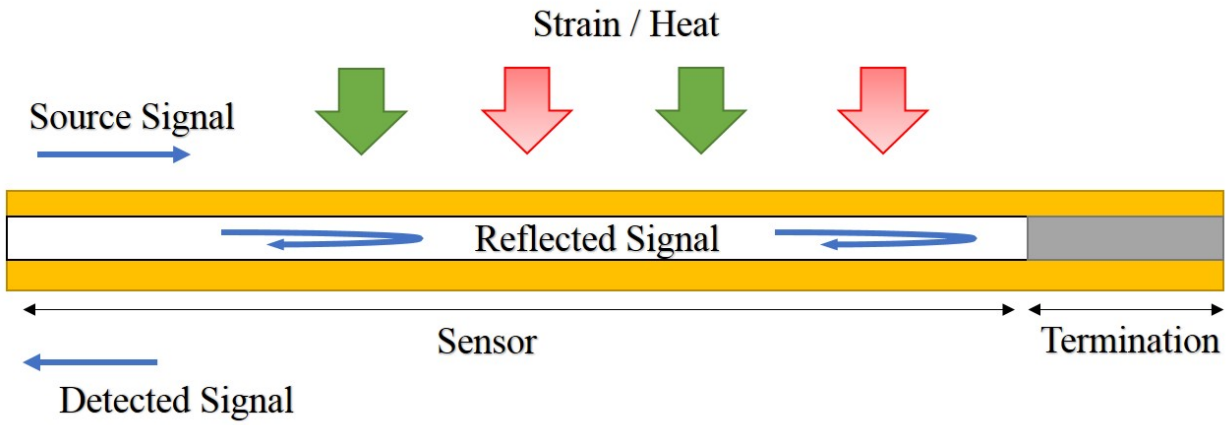

Figure 5.1: Intrinsic optic fiber sensor. Not to scale.

The source signal is scattered along the entire sensing length, producing distributed points of

measurement. External force elongates the fiber, causing the photons to scatter differently in the optic fiber. The detected signal can then be evaluated according to the distinct type of scattering the user wishes to investigate.

5.2 Scattering Mechanisms for Distributed Measurement

Intrinsic optic fiber sensing is dominated by three types of scattering: Raman, Brillouin, and Rayleigh. Each type of scattering has its own characteristics, which can vary greatly. Figure 5.2 is an example emission spectrum of light scattering in glass, and Figure 5.3 is the equivalent Jablonski diagram. According to Krohn et al [1], the Brillouin components are approximately tens of MHz wide, and are separated by 11 GHz. The Raman components are much broader, about 6 THz wide, and are separated from the input by 13 THz. The Rayleigh scattered intensity is an order of magnitude (OM) higher than the Brillouin intensity, and 3 to 5 OM higher than the Raman scattered intensity. Scattered wavelengths above and below the input are known as Stokes and anti-Stokes components, respectively.

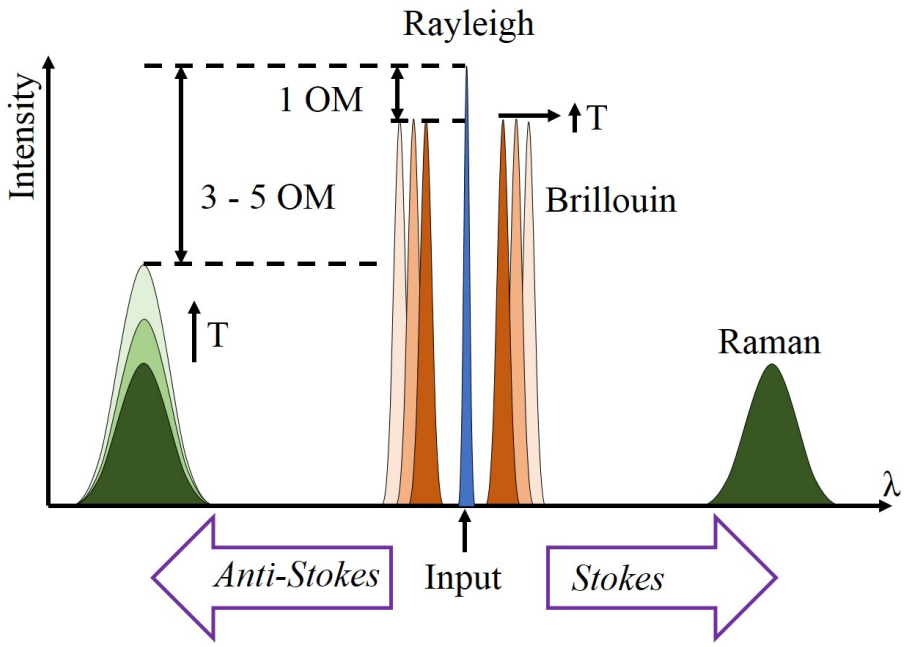

Figure 5.2: Scattered light emission spectrum of glass. Not to scale.

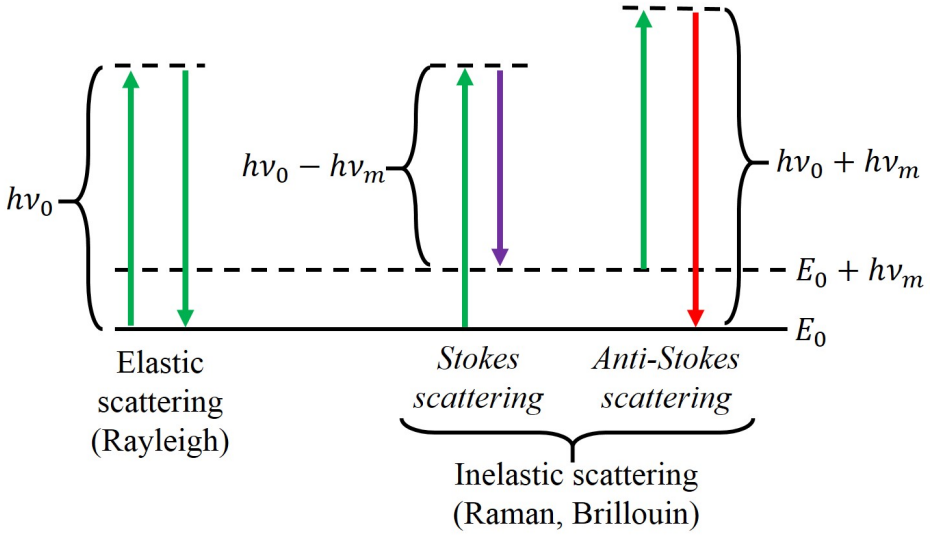

Figure 5.3: Jablonski diagram for photon scattering in glass, where the input energy is $E = h\nu_0$. Not to scale.

Raman scattering is a form of inelastic scattering and is the result of incident photons reacting with thermal vibrational modes of individual molecules. The scattered photons can experience a decrease or increase in energy, resulting in Stokes and anti-Stokes components, respectively. The anti-Stokes components are particularly sensitive to temperature only, so it is this portion of the spectrum that is investigated in Raman scattering-based DTS.

Brillouin scattering is another form of inelastic scattering, occurring between incident photons and refractive index variations. These variations are caused by acoustic waves formed by thermal vibrations in the molecular lattice. The acoustic waves occur at a specific wavelength along the optic fiber, and produce a backscattered signal at spatial intervals corresponding to this wavelength. These intervals restrict the points of measurement available through Brillouin scattering, but both Brillouin and Raman scattering-based sensors are well suited for long-distance use where sensors can be kilometers in length. Brillouin scattering is sensitive to both strain and temperature.

Fiber Bragg grating (FBG) sensors produce measurements at periodic refractive index variations along the sensor length. Bragg gratings are deliberately imposed onto the fiber before interrogation via intense ultraviolet (UV) light. The UV light changes the density of the silica, and therefore its

index of refraction. Fiber Bragg grating sensors are not scattering-based like Raman, Brillouin, or Rayleigh sensors, but they are pertinent to the current discussion of distributed optic fiber sensing. Bragg gratings act as individual sensors, since the reflected signal can be evaluated at each grating for strain, temperature, or both. Equation 5.1 shows the Bragg wavelength condition, where λ_B is the Bragg wavelength, n_{eff} is the grating refractive index, and Λ is the grating period. When a grating reaches the Bragg condition, this wavelength is reflected and detected.

$$\lambda_B = 2n_{eff}\Lambda \tag{5.1}$$

Many individual Bragg gratings can be imposed on one length of optic fiber, creating a quasi-distributed sensor. In addition to Raman and Brillouin scattering-based sensors, FBG distributed sensors are also well suited for long-distance applications.

The current work will utilize sensors that exploit Rayleigh scattering. The interrogation of Rayleigh backscatter can be compared to a hypothetical continuous FBG sensor, except no modifications to the inherent silica density are made. Instead, backscatter due to density variations at the atomic scale is collected and averaged, yielding dense distributed measurements.

The sharp peak in Fig. 5.2 highlights the lack of effects caused by this form of scattering, which is elastic. Unlike Raman and Brillouin, Rayleigh scattered photons are at the same energy (therefore wavelength and frequency) as the input signal. The scattered intensity I can be found using Rayleigh's equation (Eq. 5.2). Table 5.1 lists the parameters of this equation.

$$I = I_0 \frac{8\pi^4 N\alpha^2}{\lambda^4 R^2} \left(1 + cos^2\theta\right) \tag{5.2}$$

Table 5.1: Parameters of Rayleigh equation (Eq. 5.2).

Parameter	*Definition*
I	Scattered intensity
I_0	Incident intensity
N	Number of scatterers
α	Polarizability
λ	Incident wavelength
R	Distance from scatterer
θ	Scattering angle

Scattering particle size and incident wavelength can both affect the process of Rayleigh scattering. The former is a requirement; particles in the path of photons must be approximately 1/10 the size or smaller than the respective photons' wavelength. If the particle size is of a similar order as the wavelength, then a phenomenon known as Mie scattering occurs.

5.3 Interferometry and Signal Analysis

Several hardware configurations (interferometers) can be used to interrogate optic fibers. The sensor configuration choice depends on the nature of the signal that is to be evaluated and the measured quantity of interest.

Figure 5.4 shows the four basic interferometer configurations that are used for optic fiber interrogation. The interference produced by Mach-Zehnder (a) and Michelson (b) configurations can be evaluated in the same manner, with one arm serving as a sensor and the other arm as reference. Fabry-Pérot (c) and Sagnac (d) interferometers are also quite useful for fiber optic sensing, but are beyond the scope of this work. The sensor in the Fabry-Pérot design can be a mirror or a small cavity which reflects the signal. Sagnac interferometers evaluate the phase shift between two coiled fibers attached to a rotating assembly. The Mach-Zehnder design will be in use for the duration of the current study. The sources in Fig. 5.4 are sometimes designated as tunable laser sources (TLS).

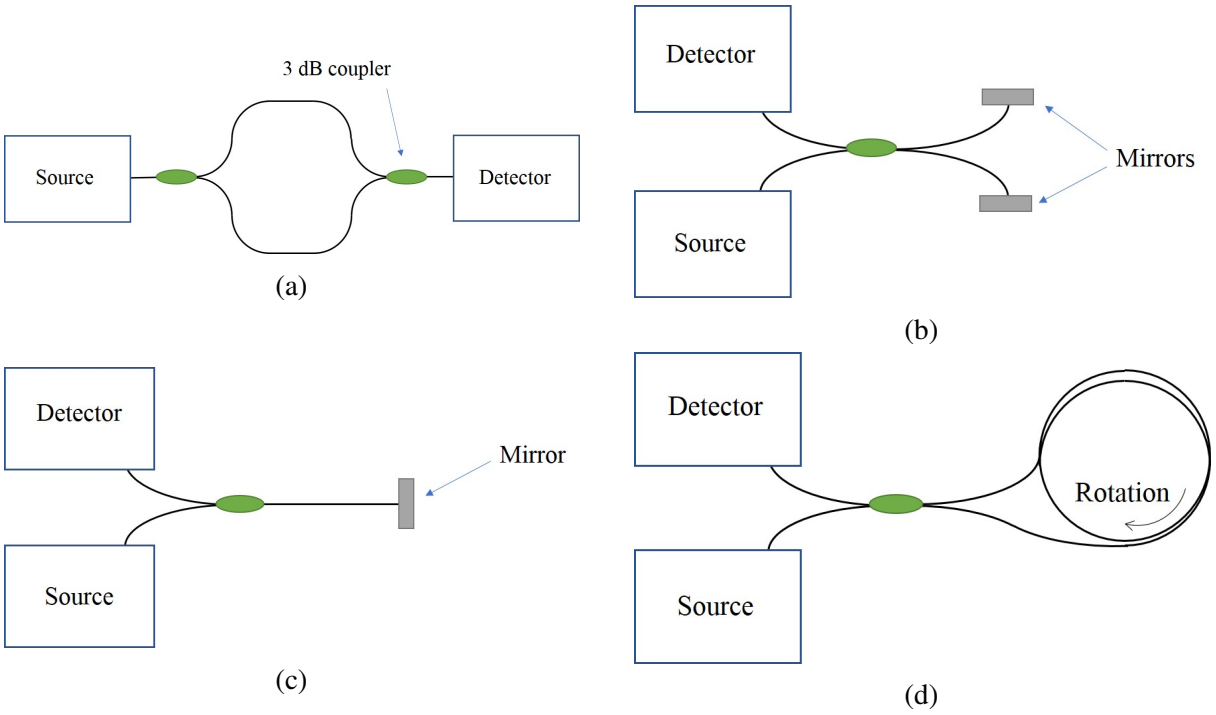

Figure 5.4: Four basic interferometer configurations: Mach-Zehnder (a), Michelson (b), Fabry-Pérot (c), and Sagnac (d).

This hardware employed in this study uses swept wavelength interferometry (SWI) to evaluate backscattered spectral shift in the Mach-Zehnder design. The TLS produces light within a small range of wavelengths (1540 $\pm$ 30 nm in this work), which are chosen so the Rayleigh backscatter will show a resonance in this range. The interference pattern between the source and detected signals can be represented as complex frequency functions, and the source can be characterized by Eq. 5.3. Both E_0 and the optical signal frequency ω are functions of time.

$$E_{source} = E_0 e^{-i\omega t} \tag{5.3}$$

The optical source signal is split into two separate signals in the Mach-Zehnder design (E_1 and E_2) and recombined as they move into the detector. The detected signal takes the form of Eq. 5.4. The separated signals have the form $E_n = E_0(t + \tau_n)$, where $n = 1, 2$ and τ is the time delay between the source and detector.

$$E_{out} = E_1 e^{-i\omega_1 t} + E_2 e^{-i\omega_2 t} \tag{5.4}$$

When the signal E_{out} is collected, it is automatically squared. This yields an expression for intensity, which is proportional to power. A Fourier transform of the detected power calculates the dominant interference fringes. The interference fringes reveal the spectral shift of the Rayleigh backscatter.

The detected temperature is calculated automatically from the spectral shift along the optic fiber. The total strain experienced by the optic fiber is proportional to this spectral shift. Equation 5.5 shows the standard linear relation between the spectral shift, mean optical wavelength, and the corresponding total strain. This relationship is analogous to FBG sensors, and is one of the most common (and simplest) ways to describe Rayleigh backscatter DTS measurements. Here, λ and $\Delta\lambda$ are the mean wavelength and spectral shift. The K-coefficients in Eq. 5.5 are constants based on the material properties of the fiber, i.e. germanium-doped silica. The default values of K_T and K_ϵ are -0.638 $^\circ$C^{-1} and -6.67999983, respectively. These values were generated for the fiber used in this study, which will be described in the next chapter. One coefficient can be assumed for temperature change (ΔT) and strain (ϵ), but the option of converting Eq. 5.5 to a higher order polynomial is available during the sensor configuration process. After temperature change is found, it is then added to a reference temperature (baseline), resulting in actual temperature.

$$\frac{\Delta\lambda}{\lambda} = K_T \Delta T + K_\epsilon \Delta\epsilon \tag{5.5}$$

If the fiber sensor is allowed to expand and contract freely, then only thermal strain persists in the fiber. The mechanical strain term in Eq. 5.5 ($K_\epsilon\epsilon$) becomes negligible, and only the temperature term ($K_T\Delta T$) remains. Temperature change is then added to a reference temperature, resulting in actual temperature. Distributed temperature measurements with Rayleigh backscatter can only be deemed valid if the mechanical strain is accounted for. Most of the difficulty of temperature measurements with Rayleigh backscatter DTS stems from this fact.

6. GENERAL RESEARCH METHODS

The concept and technology behind Rayleigh DTS is well understood, but applications are not quite as developed. This technology was originally developed for high-resolution strain measurements, but it has recently found more use in temperature sensing. Further studies in sensor design and installation technique will continue to advance distributed temperature measurement with Rayleigh backscatter-based measurement techniques.

6.1 Distributed Fiber Sensor Construction

Fiber sensor construction technique remained the same throughout this study. The sensor installation materials varied slightly between applications, but all methods drew materials from a common list. Several pieces of specialized hardware are necessary to splice optic fiber. Table 6.1 is a generic list of hardware needed to construct distributed optic fiber sensors.

Table 6.1: List of necessary equipment and materials to construct distributed optic fiber sensors.

Item	*Dimensions*	*Material*	*Purpose*
Splice-on connectors (SOC)	SMF, APC end	-	Head of sensor
Bulk single-mode optic fiber	155 μ m	Silica / Polyimide	Sensor body
Bulk coreless optic fiber	155 μ m	Silica / Polyimide	Sensor tail, attenuates signal
Core-alignment fusion splicer	-	-	Welds fibers
Cleaver	-	-	Prepares stripped fiber for fusing
Stripping Tool	-	-	Strips coating from fiber
Acetone	-	-	Cleans fiber for fusing

Several options are available for each piece of equipment, but they must all produce quality results. The method of DTS implementation requires a high level of detail and caution, especially when installing fiber into an experiment. More information about the types of optic fiber and fusion splicer used in this document can be found in Appendix A.

The optic fiber sensor has three main parts: head, body, and termination. The fiber head is a short bare-silica fiber splice that is protected by a sleeve and shipped in a Splice-On Connector (SOC). Various types of heads can be used, depending on extension cable and interrogation system. The body of a fiber sensor is a section bulk fiber, usually with unaltered polyimide coating. The termination is also a section of bulk fiber, but needs to be coreless to attenuate the signal. The termination coating does not need to match that of the body section.

The first step in sensor fabrication is to cut lengths of bulk sensor fiber and coreless fiber. The sensor fiber should have two feet of extra length. The coreless fiber should be cut to about one foot,

or it can be stripped on the spool and cut afterward. Generous lengths fiber will allow for user error and for easier insertion into the fusion splicer.

Before attaching the fiber head, consideration must be given to the method of securing the fiber head. Heat-shrink and PTFE tubing complement the head parts well, but all of these parts must be on the body end before one end is stripped for head attachment. The head splice protection sleeve and head-body adapter are the only essential parts, but the fiber after the head should be protected in some way. It is a good practice to perform a mock-up install of all heat-shrink and PTFE tubing with all head parts before splicing.

The head of the fiber is installed by removing one of the fiber clamps from the fusion splicer, and replacing it with a SOC directly from the package. A short section of pre-cleaned bare-silica fiber should protrude from the SOC and reach the arc tips. Then, about 2 cm of body fiber should be stripped, cleaved, cleaned with acetone, and placed into the remaining clamp. Stripping fiber can be difficult, but 2 cm is necessary for a good, 90 °cleave. No coating should be present on the cleaver's grips on either side of the blade. If stripping becomes too time consuming, applying acetone before stripping can sometimes help.

After the head is spliced on, the fiber can be removed from the SOC. The splice protection sleeve should be placed over the newly spliced section and shrunk onto the fiber. Some fusion splicers have a heating compartment that is designed specifically for this application. When the sleeve is cool, the head-to-body adapter can be placed over the sleeve and connected with the head adapter, which is included in the SOC kit.

Finally, the termination section can be spliced to the end opposite the head. Two centimeters should be stripped on both fibers, cleaved, cleaned, and fused in the splicer. If the head was attached just before this step, then the other fiber clamp will need to be re-installed onto the splicer. The one-foot length of termination fiber should be cut to 5 cm after splicing, and its end slightly crushed. An alternative is to use 25 cm of termination fiber without crushing, but this is more difficult to install and secure.

The user can determine whether to attach the head or the termination first, since the choice

does not affect the sensor or measurement quality. This is determined by the quality of cleaves and splices, not the order in which the fiber was put together. Figure 6.1 is an example of how PTFE tubing, heat shrink tubing, and a compression fitting can be combined with a fiber sensor.

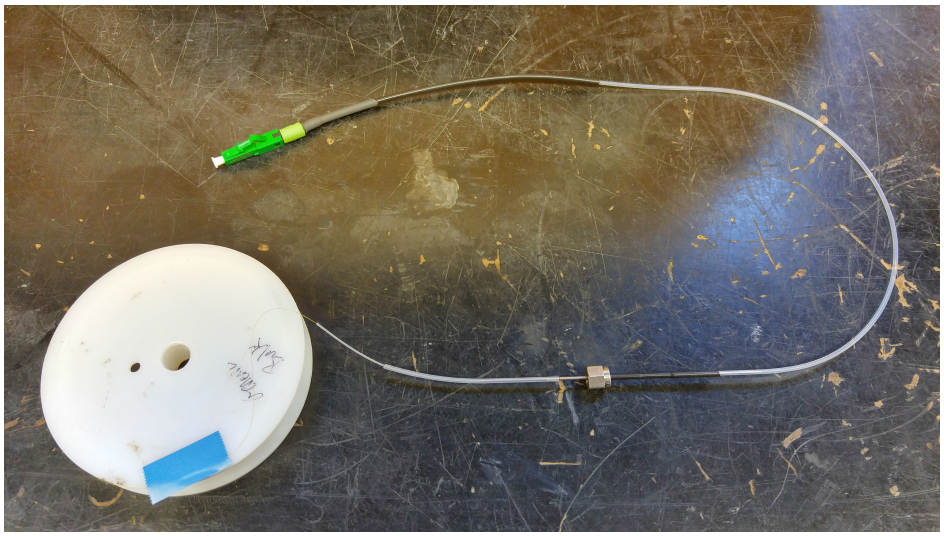

Figure 6.1: Optic fiber sensor constructed with PTFE and steel tubing.

Once the sensor has been constructed, its iso-train profile can be recorded by the Optical Distributed Sensor Interrogator (ODiSI) unit. This profile is a recording of the fiber sensor's Rayleigh backscatter that is stored on the ODiSI's computer. During use, this profile is compared to the profile obtained from the device under test (DUT) and a relative strain measurement is made. Detailed procedures can also be found in the LUNA Sensor Config User's Guide.

6.2 Fiber Installation Materials

Fiber construction and installation are two separate challenges in and of themselves, but users benefit from considering installation requirements when constructing fiber sensors.

The installation of DTS normally includes supplementary materials to protect the fiber and anchor it in place. Table 6.2 lists the materials used in this study. Most of these materials are widely available and no special equipment is required to handle or modify them.

Table 6.2: List of equipment and materials used to install distributed optic fiber sensors.

Item	*Dimensions*	*Material*	*Purpose*
Capillary tubing	21, 18 ga.	304 SS	Protect fiber, match steel surface
Plastic tubing	21, 30 ga.	PTFE	Protect fiber
Heat shrink tubing	0.25 in	Polyolefin	Connect PTFE tubing to sensor head
Heat transfer putty	-	-	Adhere and transfer heat to capillary tubing
Steel foil	-	316 SS	Anchor capillaries to metal surfaces
Springs	0.25 in. x 1.0 in.	302 SS	Apply tension to fiber or capillaries
Drill stop collar	1/16 in.	Steel	Apply tension to fiber or capillaries
Two-stage epoxy	-	-	Adhere fiber or capillary tubing to other tubing

6.3 Data Acquisition and Recording

The method of data recording in this study varied by application. All thermocouple and flow rate data were obtained with LabVIEW virtual instruments (VIs). The software included with ODiSI unit was used to record all DTS data. Table 6.3 lists the features of each data recording method. A complete description of the data acquisition hardware used can be found in Appendix B.

Table 6.3: Data recording hardware and parameters used in this study.

Hardware	*Experiment*	*Sensor Types(s)*	*Sampling Rate(s)*
LUNA ODiSI-A50	Two-phase heated vertical pipe	DTS	1.5 - 2.0 Hz
LUNA ODiSI-B	WRCCS, HTGR Upper Plenum	DTS	50, 100 Hz
NI cDAQ 9171 w/ 9214 module	Two-phase heated vertical pipe	Thermocouples	1 Hz
NI SCXI 1001 w/ various modules	WRCCS, HTGR Upper Plenum	Thermocouples, RTDs, Flowmeter	1 Hz

The data file sizes created by LabVIEW VIs are typically not large, but DTS files can be very large. A typical raw DTS file size is approximately 12-13 GB. Data file size can be controlled with data acquisition parameters in the ODiSI software. The sampling rate of the ODiSI A50 model cannot be precisely controlled (unlike the ODiSI-B), and depends heavily upon the data destination during recording. The best sampling rates with the ODiSI-A were achieved by writing the data to a solid state drive. All DTS files were written into their raw format, which is a proprietary binary format. Files written in LabVIEW VIs were either comma separated value (CSV) or text files.

6.4 Sensor Calibration

Several types of temperature sensors underwent calibration during this study in order to produce the most accurate results possible. The following subsections describe the calibration efforts for these sensors.

6.4.1 Thermocouple and RTD Calibration

The temperature sensors used in the WRCCS and HTGR upper plenum facilities were calibrated with a Fluke® 1524 reference thermometer and 5615 reference RTD probe. Two calibration points

were used for each thermocouple. One point was obtained by inserting sensors into a pouch of ceramic fiber insulation, and left to sit overnight (shown in Figure 6.2). The second point was obtained by bringing an electric kettle to boiling and inserting the sensors into the water. The same equipment was used to calibrate the thermocouples in the HTGR upper plenum facility. Calibration equipment was unavailable for the sensor in the heated pipe experiment.

Figure 6.2: Method for obtaining room temperature calibration point for WRCCS thermocouples.

In the WRCCS facility, the thermocouples were calibrated with two points, while the RTDs used four points. Both of these sensor types have linear responses in the expected operating ranges (20 - 100°C). Table 6.4 lists the averaged calibration points for non-panel thermocouples and RTDs. Thermocouple data were averaged over approximately 30 seconds, and RTD data were averaged over 5 minutes. The RTDs were calibrated alongside the DTS in a lab oven. Figure 6.3 is a photograph of the collocated RTDs and DTS. The RTDs were removed for temperatures over 100°C. Calibration data for the panel thermocouples can be found in Appendix C.

Table 6.4: Calibration points and averaging parameters for non-panel TCs and RTDs in the WRCCS.

Sensor	*Room Temp. Point (°C)*	*Int. Point (°C)*	*Int. Point (°C)*	*Sat. Point (°C)*
Ref.	21.391	-	-	99.759
Tank In	21.755	-	-	100.206
Tank Out	21.743	-	-	100.678
Top Chimney	21.696	-	-	100.500
Sec. Tank In	21.945	-	-	100.402
Sec. Tank Out	21.640	-	-	100.030
Ref.	20.425	39.097	50.687	99.602
Vessel In	22.525	41.461	53.051	103.981
Vessel Out	26.204	45.009	56.994	107.812

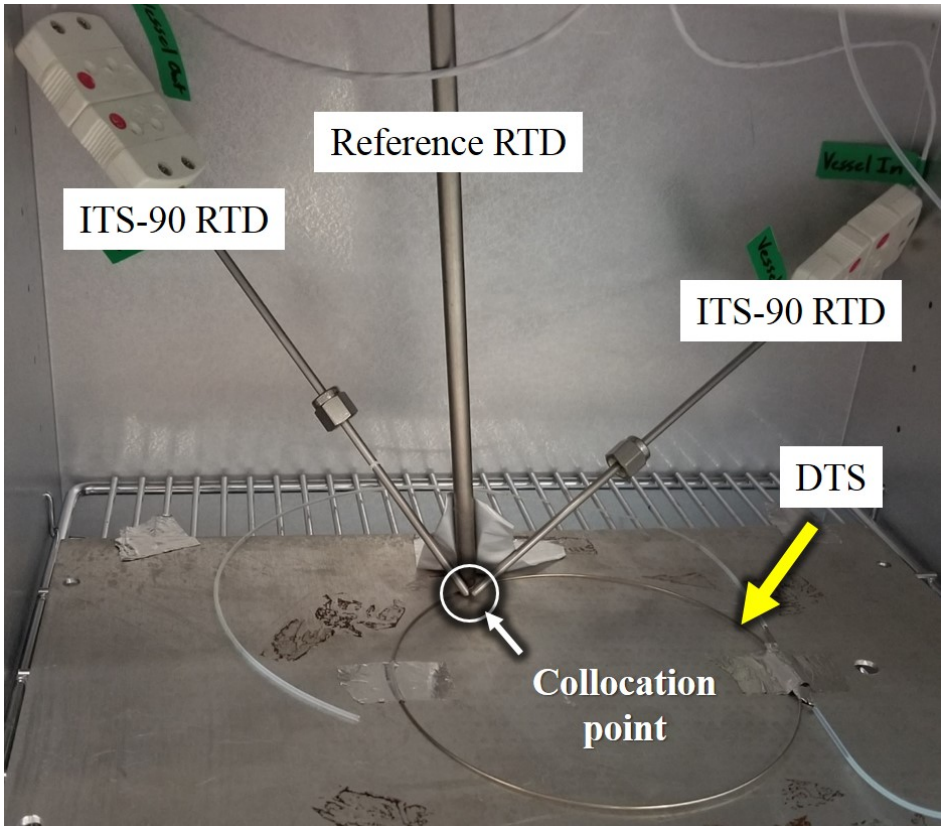

Figure 6.3: Collocation of reference RTD, OMEGA RTDs, and DTS in lab oven for calibration.

Figures 6.4 and 6.5 show the calibration curves for select non-panel thermocouples and RTDs in the WRCCS facility. The four-point calibration of the RTDs was performed to confirm their linear response in the applied temperature range.

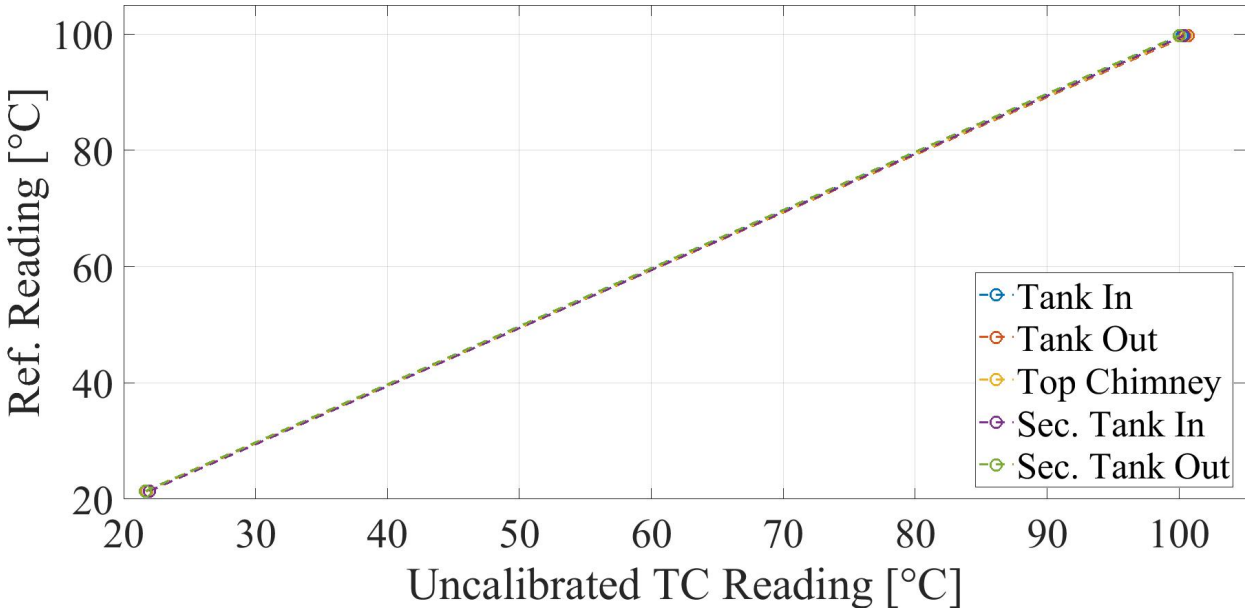

Figure 6.4: Calibration curve for select non-panel thermocouples in WRCCS facility.

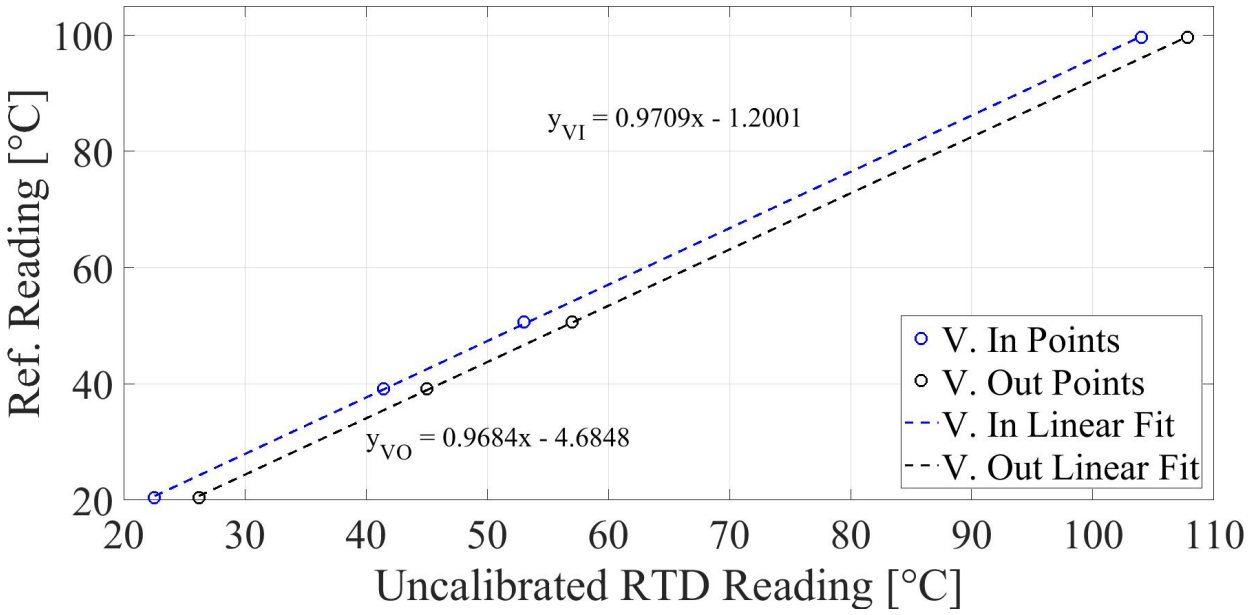

Figure 6.5: Calibration curve for RTDs in WRCCS facility.

Only the calibration curves for select thermocouples in the HTGR upper plenum facility are

available. Table 6.5 lists the relevant thermocouples and their parameters. The first two thermocouples, "c1b" and "c1t" are wall-mount thermocouples that are adhered in-place. They cannot be removed for calibration.

Table 6.5: Calibration curves for HTGR upper plenum thermocouples used in the current study.

Thermocouple	*Location*	*Type*	*Calibration Curve*
c1b	Bottom of center pipe	T	N/A
c1t	Top of center pipe	T	N/A
Inlet	Main coolant inlet	T	y = 1.2315x - 8.7587
Outlet	Main coolant outlet	K	y = 1.0197x - 3.0793
CJ Inlet	Inlet of cooling jacket	K	y = 1.0175x - 2.9205
CJ Outlet	Outlet of cooling jacket	K	y = 1.021x - 2.7584

6.4.2 Transient DTS Calibration

The DTS calibrations used a fiber inside a capillary tube in a temperature-regulated oven, simulating the expected experimental conditions. The first DTS calibration followed the procedure outlined by Tompkins et al [104]. Here, five Type-T thermocouple probes were used instead of one Type-K probe. The oven was turned to its highest setting ($\sim$250°C) while recording both thermocouple and DTS data. Figure 6.6 shows the configuration of sensors in the oven. Each Type-T thermocouple had been previously calibrated.

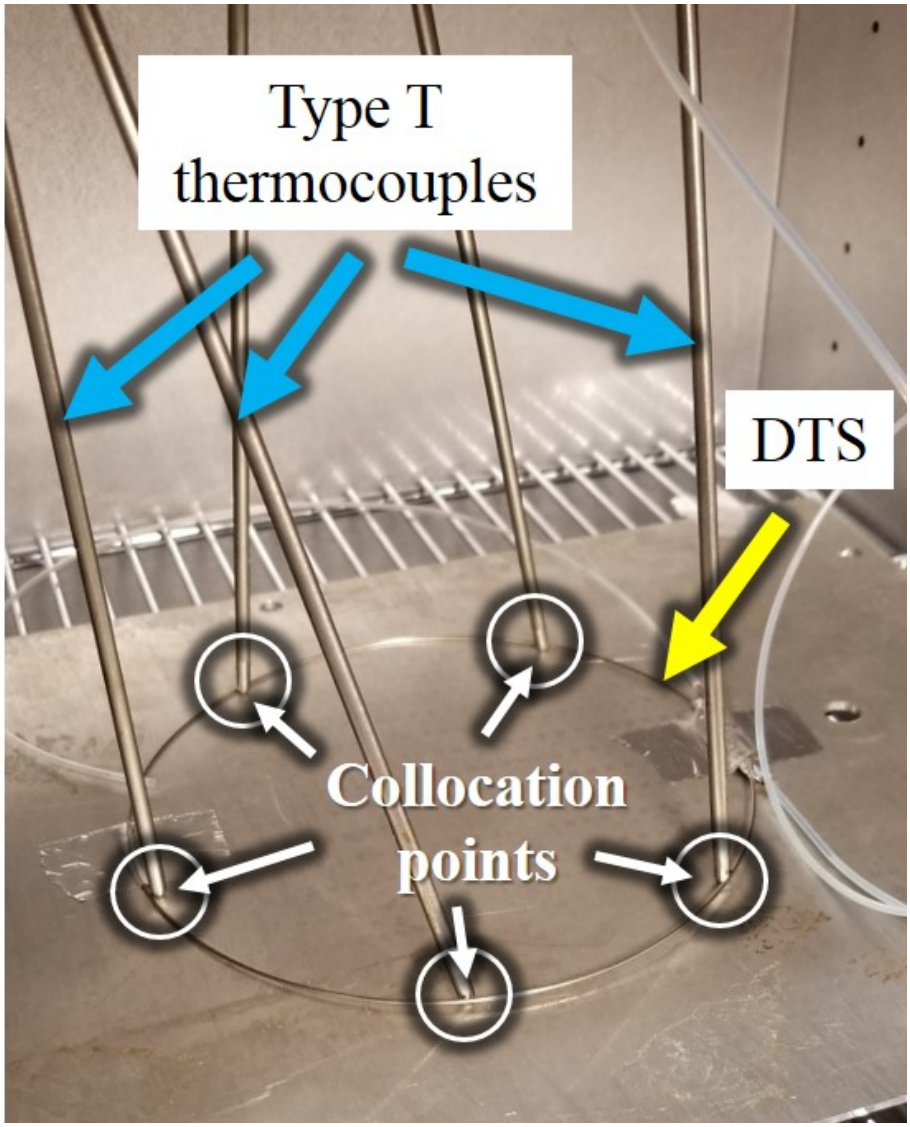

Figure 6.6: Collocation of RTDs and DTS in a lab oven for transient calibration.

Figure 6.7 shows the recorded thermocouple and DTS readings during the final transient calibration run. The DTS was heat-cycled to maximum temperature several times before these readings were recorded, alleviating the heat-cycle effects observed by Lisowski et al [70] and Tompkins et al [104].

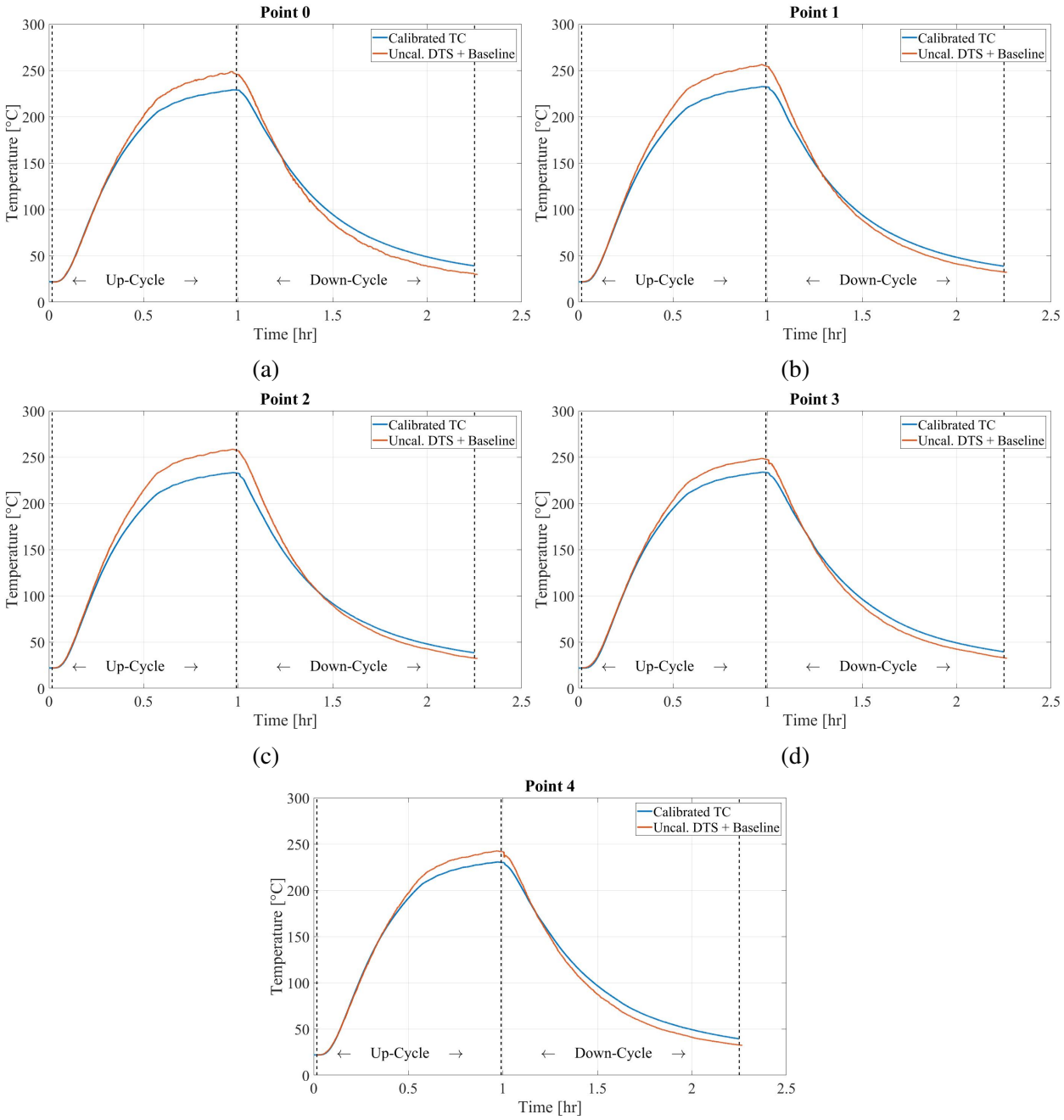

Figure 6.7: Transient thermocouple and uncalibrated DTS recordings in lab oven heat cycle.

This calibration yielded 10 calibration curves, two for each collocated thermocouple point and one for the up- and down-cycles. Figure 6.8 shows each calibration curve grouped by up- and down-cycle, along with the average calibration curves.

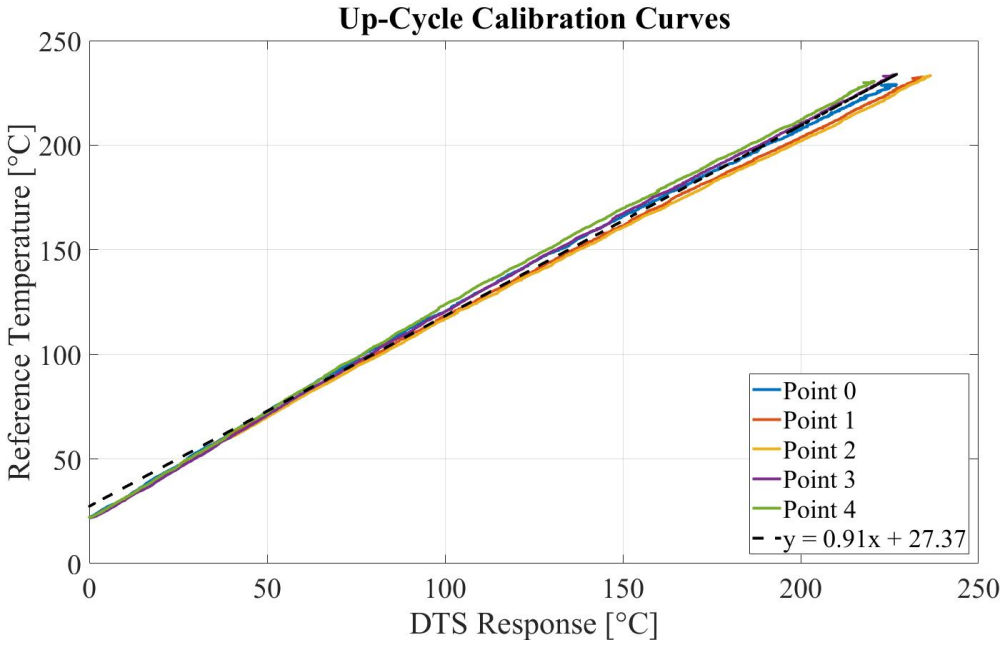

(a)

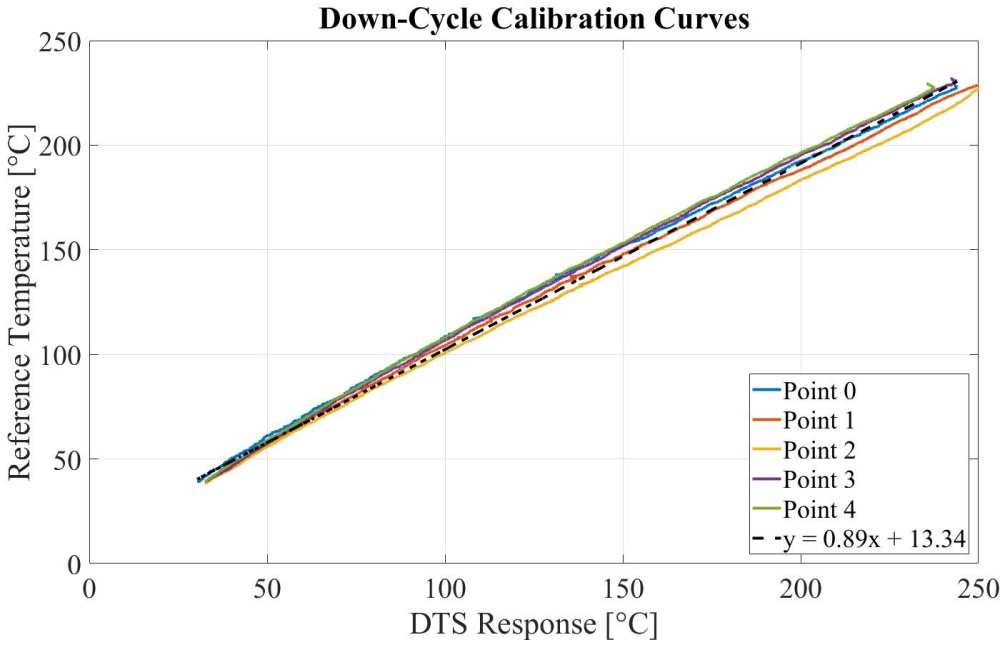

(b)

Figure 6.8: Transient DTS calibration curves for up-cycle (a) and down-cycle (b) heating.

This calibration exercise yielded very similar calibration slopes, but very different intercepts. A difference in curves was expected, but the steady-state calibration behavior still needed to be

investigated.

6.4.3 Steady-State DTS Calibration

The second DTS calibration took place in the same oven, but with one collocation point between a reference RTD and DTS. The oven was then brought to multiple steady temperatures in steps of $\sim$13°C. This configuration was shown in Fig. 6.3. Reference and DTS data were recorded at each steady temperature for approximately 30 minutes before moving to the next point. Table 6.6 shows statistics from the second DTS calibration. All values are in degrees Celsius.

Table 6.6: Statistics for second DTS calibration (steady-state).

Setpoint (°C)	*Ref. Mean (°C)*	*Ref. Std. Dev. (°C)*	*DTS Mean (°C)*	*DTS Std. Dev. (°C)*
40	38.8856	0.4139	37.5653	0.5572
50	50.4225	0.4436	47.8800	0.5682
60	62.6137	0.4797	59.9505	0.7071
75	76.6181	0.2303	73.3313	0.4872
88	83.8539	0.2006	80.7315	0.4167
100	101.4213	0.5210	99.1705	0.8898
113	114.4206	0.1818	116.5535	0.5431
125	124.2733	0.1599	128.0167	0.6221
138	138.4761	0.1566	145.8510	0.4661
150	150.7762	0.1327	157.5309	0.5930
160	160.3703	0.1367	169.5030	0.5546
175	173.7970	0.1316	189.7530	0.7531
188	186.9890	0.1565	206.4819	0.9566
200	197.6128	0.1422	219.6280	0.9012
210	210.5514	0.1209	235.9617	0.6445
220	221.0689	0.1129	249.8885	0.9431

Figure 6.9 shows the curve for the second full DTS calibration. A quadratic curve fit had a slightly better correlation coefficient (R^2 = 0.9995) than a linear fit (R^2 = 0.9972).

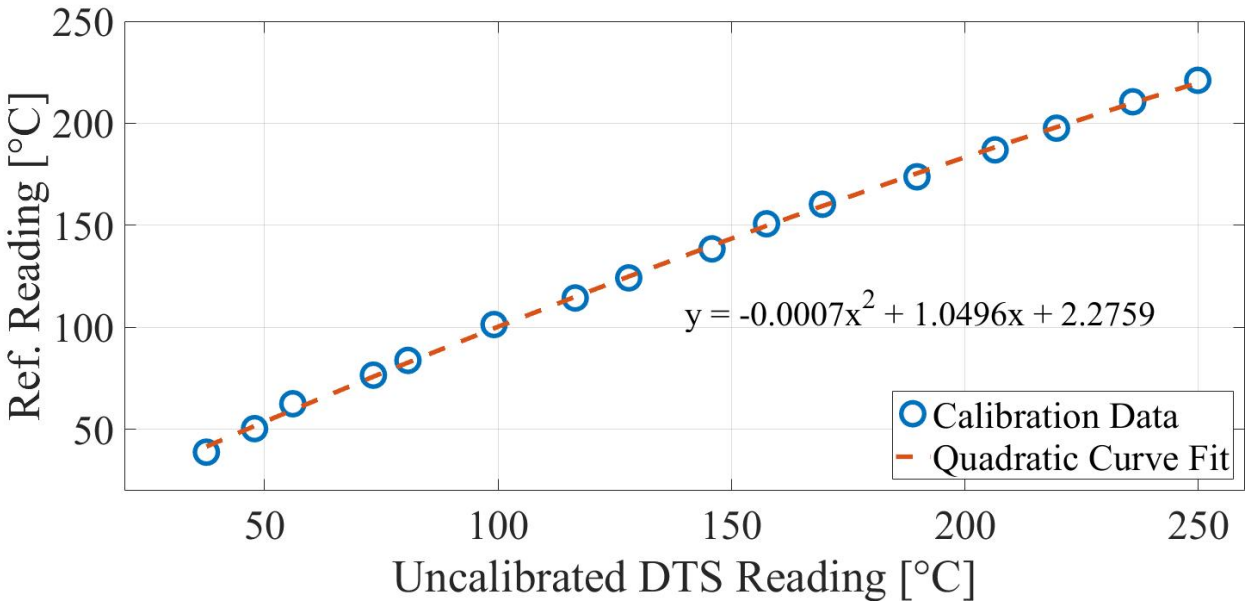

Figure 6.9: Calibration curve for second DTS calibration in air (steady-state).

Two more steady-state DTS calibrations were performed in the 25 - 100°C range to validate the data in Table 6.6 and Fig. 6.9. Table 6.7 lists the values of the final two DTS calibrations in air, and Figure 6.10 shows all three steady-state DTS calibration curves in one plot. The range of this plot has been limited to the range of the final two calibrations. All values are in degrees Celsius.

Table 6.7: Statistics for final two DTS steady-state calibrations (steady-state).

Setpoint (°C)	*Ref. Mean (°C)*	*Ref. Std. Dev. (°C)*	*DTS Mean (°C)*	*DTS Std. Dev. (°C)*
40	42.3720	0.7635	41.4038	1.2211
58	59.0098	0.5045	57.8385	1.4402
75	77.2905	0.2799	74.6831	1.7066
90	90.4262	0.5097	86.1185	1.4380
100	98.1403	0.2503	92.9630	1.2509
40	41.0235	0.3275	39.5561	0.4716
50	52.8902	0.3667	51.5131	0.5032
75	74.4147	0.3049	71.4558	0.4954
87	87.1003	0.2511	83.7620	0.6271
100	100.3984	0.3343	98.9812	1.1115

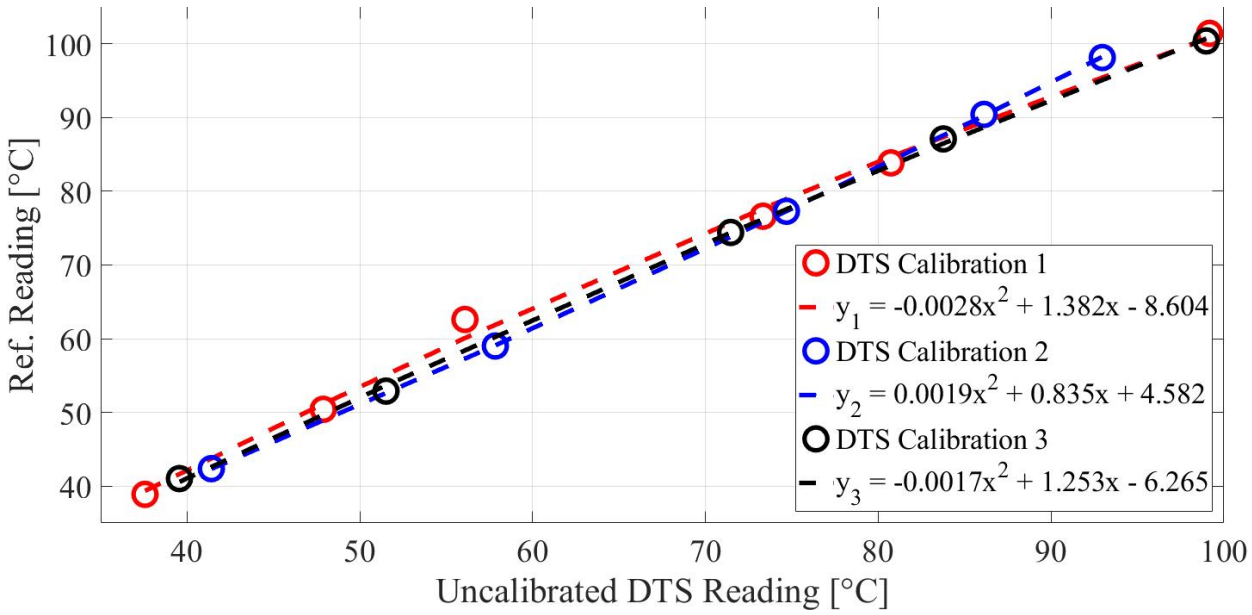

Figure 6.10: All steady-state DTS calibration curves. Maximum deviation between curves in this temperature range is 2.0 °C.

Table 6.8 quantitatively lists the linear calibration curves for the data presented in Fig. 6.10. This data is the most representative of common laboratory experiments and can be used to calibrate most DTS readings.

Table 6.8: Numerical calibration curves from Fig. 6.10.

Steady DTS Calibration	*Calibration Curve*
1	$y_1 = 1.0151x + 1.5285$
2	$y_2 = 1.0846x - 3.1287$
3	$y_3 = 1.0136x + 1.1737$

6.5 Uncertainty Estimation

Estimation of the measurement error was conducted following approaches developed and discussed by Lomperski et al [66]. This method considers the total uncertainty as sum of different contributors as shown in Equation 6.1. Each term of Eq. 6.1 is explained in the following paragraphs. This method is only applicable to sheathed DTS inside capillary tubing. Uncertainty estimation for exposed DTS was not performed.

$$\sigma^2_{total} = \sigma^2_{K_T} + \sigma^2_{\epsilon} + \sigma^2_{ref.} + \sigma^2_{rep.} + \sigma^2_{RH} \tag{6.1}$$

The uncertainty of the temperature coefficient σ_{K_T} is due to the material properties of the optic fiber, and was estimated to be 1.0°C. This value was adopted from a study by Lomperski et al [65], since the current study used the same sensing fiber brand and model.

The applied strain uncertainty σ_{ϵ} is negligible (set to zero) in this study, and only needs accounting for when the fiber itself is under tension. The fiber sensors in this study were allowed to expand freely within steel capillary tubing.

The reference temperature error $\sigma_{ref.}$ is the uncertainty of the ambient reference measurement,

which was 0.022°C. This is the combined uncertainty of the reference thermometer and RTD probe at room temperature, which varies slightly between 20 and 25°C.

The repeatability error $\sigma_{rep.}$ is the factory-given repeatability of the LUNA ODiSI-B in the mode (5.0 mm gage length) used for this work. This value was adopted from the manufacturer as 0.01°C.

The uncertainty due to relative humidity (RH) σ_{RH} stems from the use of polyimide-coated fiber sensors. Humidity sensitivity for polyimide coated fibers has been studied, but further investigation into these effects is beyond the scope of the current study. The polyimide coating is hygroscopic, and has been shown to cause shifts in detected values. Thomas and Hellevang [77] and Lomperski et al [66] quantified humidity-induced shifts in detected strain and temperature, respectively. However, the latter study explicitly stated that these shifts would not be applicable to all fiber measurements or installations. The calibration curves in Fig. 6.10 show a maximum variation of approximately 2.0°C. The ambient relative humidity varied by approximately 20% between calibrations, which is representative of the lab space where the current study was performed.

Table 6.9 summarizes each of the described sources of error and their estimated values. The total uncertainty has been rounded to one decimal place.

Table 6.9: Contributors to uncertainty and their values.

Term	*Source*	*Value (°C)*
σ_{total}	-	2.2
σ_{K_T}	Conversion from spectral shift	1.0
σ_{ϵ}	Residual fiber strain	$\sim$0
$\sigma_{ref.}$	Reference (baseline) temperature	0.019
$\sigma_{rep.}$	Hardware repeatability	0.01
σ_{RH}	Relative humidity	2.0

7. SURFACE TEMPERATURE MEASUREMENTS

To the best of the author's knowledge, distributed surface temperature measurements had not been published before this study. Surface temperature profiles of this particular facility had also not been evaluated. These two facts, along with the goals of the supporting project, led to the application of DTS described in this section. Portions of this chapter have been published in the Transactions of the American Nuclear Society and are under review for publication in the International Journal of Thermal Sciences.

7.1 Experimental Facility Description

A 1:23 axial scale model of a WRCCS was instrumented with surface DTS, and is shown in Fig. 7.1. The WRCCS is a passive safety system that will be incorporated in the HTGR nuclear power plant system. A panel of heaters simulates the heat leaking from the reactor vessel. The heat generated is transferred by radiation and convection (80/20 approximate ratio) into an insulated cavity. The heat is then transferred to a cooling panel of nine vertical pipes welded together with interstitial fins. This system was designed to passively transfer heat from the cavity to the cooling panel, and inwards to the water coolant. The heated water rises through the channels, and natural circulation develops in the primary loop. The experimental facility uses an active secondary coolant loop connected to the water tank with a heat exchanger and chiller to achieve steady conditions. A butterfly valve located under the water tank can be adjusted to change the pressure drop in the loop, and in turn changing the system flow rate and overall temperature distribution.

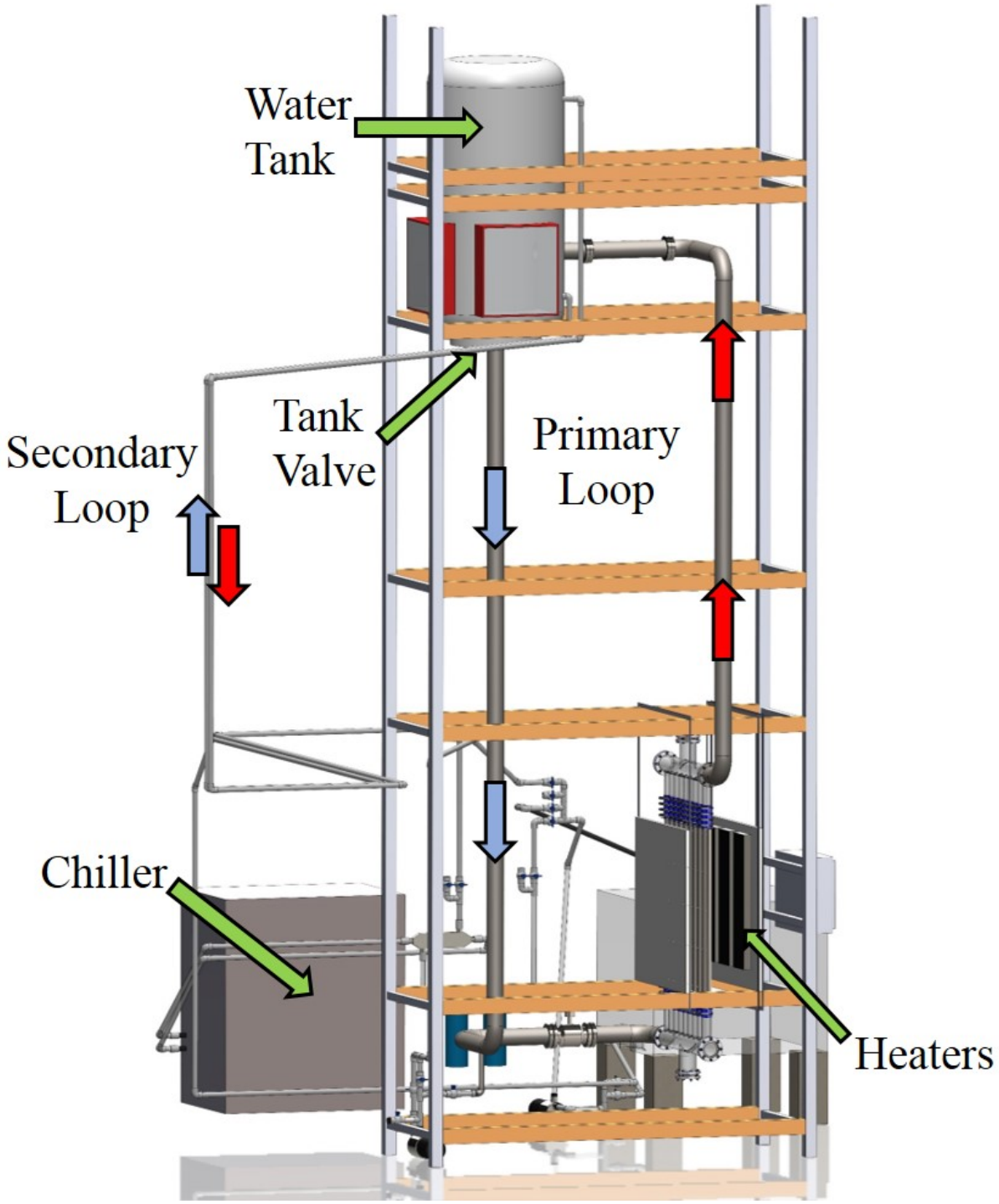

Figure 7.1: Full view of TAMU WRCCS facility. Major components and flow paths are labeled.

Figure 7.2 is a labeled diagram of the cooling panel and the surrounding structures. Flow rate,

inlet and outlet temperatures are the main parameters monitored during experimentation, especially during steady-state testing. Table 7.1 lists the characteristics of the basic instrumentation in the WRCCS facility. Inlet and outlet temperatures are measured with platinum resistance temperature detectors. This facility also has wall thermocouples on the heated side of the cooling panel and thermocouple probes in the riser water columns. In all, 137 Type-K thermocouples are installed throughout this facility.

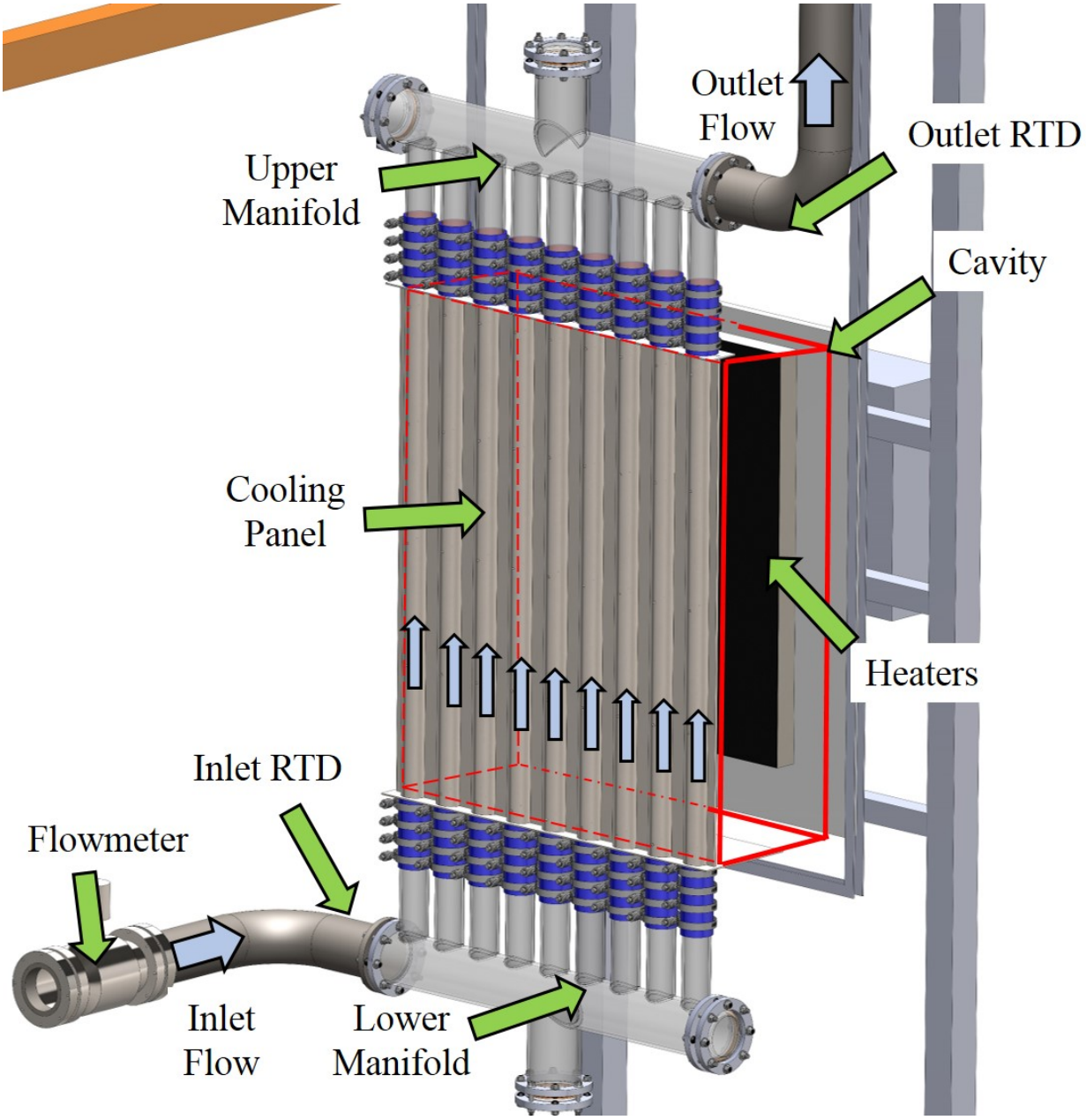

Figure 7.2: Labeled computer drawing of the WRCCS cooling panel and surrounding structures.

Table 7.1: Basic information about the conventional sensors in the Texas A&M WRCCS facility.

Sensor	*Make & Model*	*Uncertainty*
Thermocouples	OMEGA Type-K SLE	1.1°C
RTDs	OMEGA ITS-90, 100Ω	0.2°C
Flow meter	Krohne Optiflux 4100 w/ IFC 300 SC	0.2%

Passive operation is one of the key features of the WRCCS. No forced flow is necessary to establish circulation in the primary loop. Another advantage of the WRCCS is its location outside the reactor cavity. Unless the reactor vessel and cavity are breached, the WRCCS does not have contact with anything from inside the reactor vessel. The simultaneous action of containment and cooling are paramount during an accident scenario.

7.2 Facility Operation

The WRCCS facility is normally operated in one of four steady conditions. The bulk flow rate of the primary loop is controlled by the tank valve setting, which can be 25%, 50%, 75%, or 100% open. Previous tests performed with this facility have shown the largest difference in flow behavior in the cooling panel occurs between the tank valve settings of 25% and 100%, particularly in flow distribution [115]. Steady conditions are achieved by initializing a secondary loop when the lower manifold inlet temperature reaches ∼30°C. The secondary loop is actively cooled by a chiller. Steady conditions are verified with minimal variations (±0.1°C) in the primary loop water temperatures. The total power applied to the heaters was 6 kW. For the majority of steady-state testing, the target water temperature at the cooling panel inlet was 30°C. Extensive internal documentation of these procedures has been developed.

When steady conditions were achieved, 1000 acquisitions of each fiber sensor at a sampling rate of 5 Hz (down-sampled from the default 50 Hz rate) were recorded separately for each fiber. Due to the length of the fiber sensors, gage length was left at the default setting of 5 mm. This is the only mode available for fibers of this length, and yields measurements every 2.6 mm along the fiber

sensor. Facility data (thermocouples, RTDs, flow rate) were recorded at a rate of 1 Hz during the entire test.

7.3 Preliminary Fiber DTS Installation

Two installations of surface DTS were achieved on the heated side of the cooling panel wall in the TAMU WRCCS facility. The attachment of fiber DTS to solid surfaces requires all of the materials in Table 6.2. Gas environments require the same materials, excluding heat transfer putty and steel foil. When used properly, these materials isolate the DTS from mechanical strain. The DTS is allowed to expand and contract freely within the steel capillary tubing, which is adhered to a surface with heat transfer putty and foil tape.

Figures 7.3 and 7.4 are photographs of the first surface DTS installations, which did not include capillary tension. Each fiber was completely enclosed within the cavity. Fiber sensors were installed on the riser pipe walls only for this round of testing. Three fibers covering three riser pipe walls each (two passes per riser pipe) provided 18 total fiber segments available for temperature measurement. The fibers' total lengths were 12.32361, 10.53345, and 10.81851 meters. The wall thermocouples were left in place, which led to slight discrepancies in capillary spacing, which was approximately 1 inch.

Figure 7.3: Full view of installed DTS on WRCCS cooling panel wall, first round of testing.

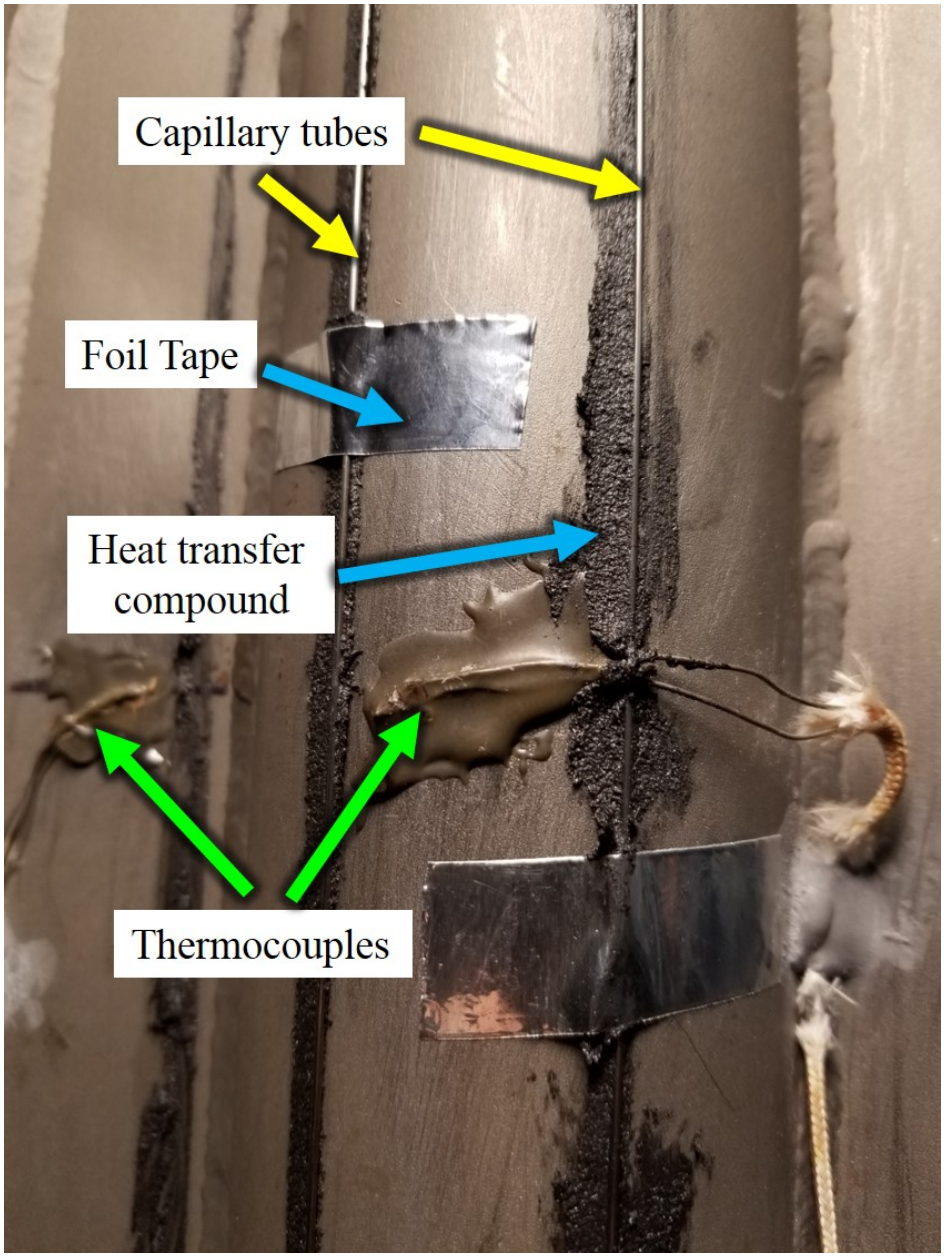

Figure 7.4: Close-up view of installed DTS on WRCCS cooling panel wall, first round of testing.

7.4 Preliminary Results

The steady-state behavior of the main facility parameters (flow rate, inlet and outlet temperatures) for all four flow conditions are presented in Figure 7.5. These data represent the facility conditions that the first DTS installation was tested in. They also depict all four possible experimental facility

flow conditions available. The flow rate data and temperature dat have been down-sampled by factors of 20 and 300, respectively, to provide a better visual representation. This data reduction does not remove any trends. The inlet and outlet temperatures in these plots were obtained with Type-K SLE thermocouple probes, which were later upgraded to RTDs.

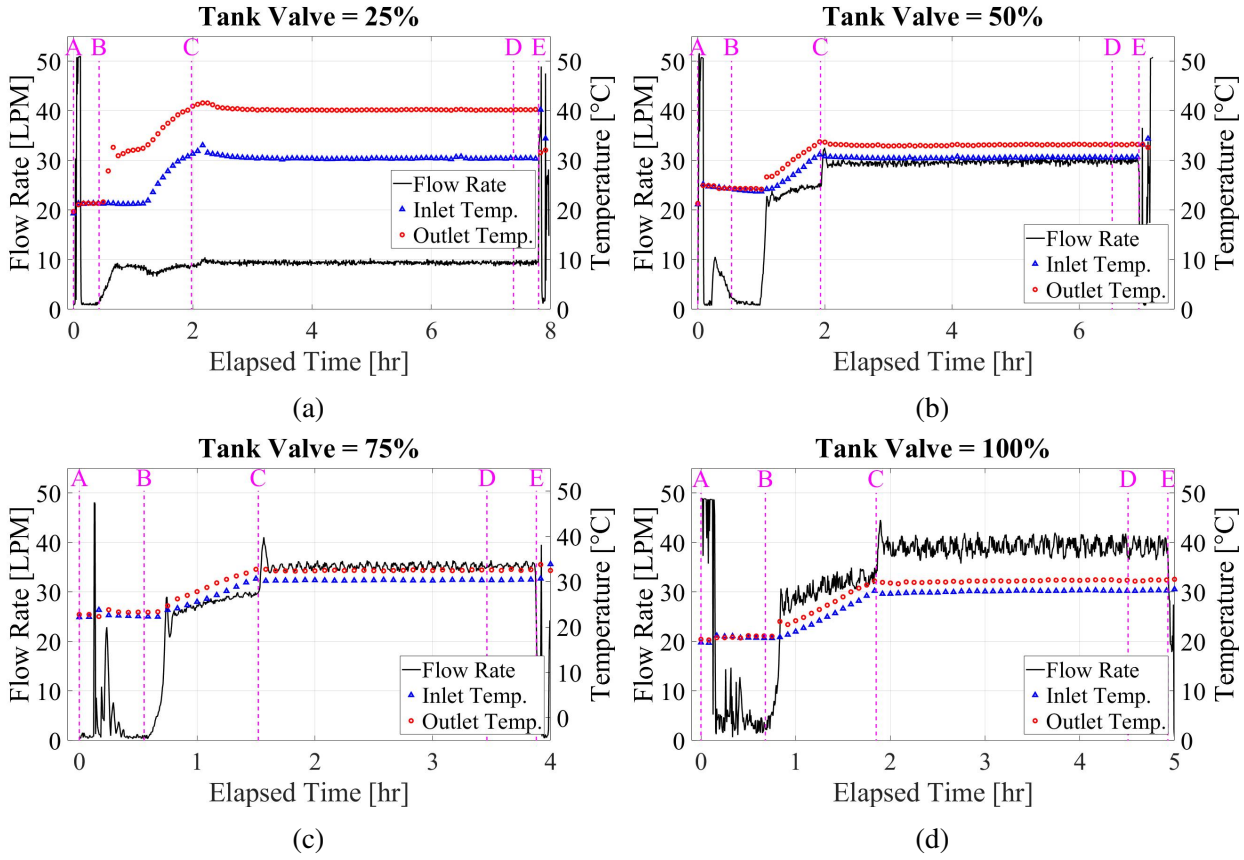

Figure 7.5: Main facility parameters recorded during steady-state testing of WRCCS.

Table 7.2 lists the labeled events shown in each plot in Fig. 7.5. The specific times of each event varied between tests, but their descriptions and order remained the same.

Table 7.2: List of events in each plot in Fig. 7.5.

Event	*Description*
A	Data recording start
B	Heaters to 6 kW
C	Secondary loop on, chiller on
D	Steady conditions reached, DTS recording start
E	DTS recording end, heaters off

The time-averaged values of these facility parameters during steady conditions are listed in Table 7.3. This data is in good agreement with previous results of the same facility, and confirms the facility was operated in the same manner. The tank valve position is an independent value of this facility. Each tank valve setting induces a specific bulk flow rate and Reynolds number.

Table 7.3: Time-averaged main facility parameters during steady conditions in Fig. 7.5.

Figure	*Tank Valve Position*	$\overline{\dot{V}}$ (LPM)	*Re*	$\overline{T_{In}}$ (°C)	$\overline{T_{Out}}$ (°C)
4.1(a)	25%	9.40	2,352	30.4	40.2
4.1(b)	50%	29.8	7,753	30.6	33.2
4.1(c)	75%	35.2	9,158	30.3	32.5
4.1(d)	100%	39.3	10,224	30.3	32.4

Figure 7.6 shows the time-averaged temperature recorded by the DTS on the wall of the cooling panel during each steady condition. Since three fiber sensors had to be interrogated and the LUNA ODiSI-B can only interrogate one fiber at a time, the data in Fig. 7.6 had to be gathered separately. However, the entire WRCCS facility has shown to be capable of reliably reaching steady conditions across many tests. This justifies plotting the data as it appears in Fig. 7.6.

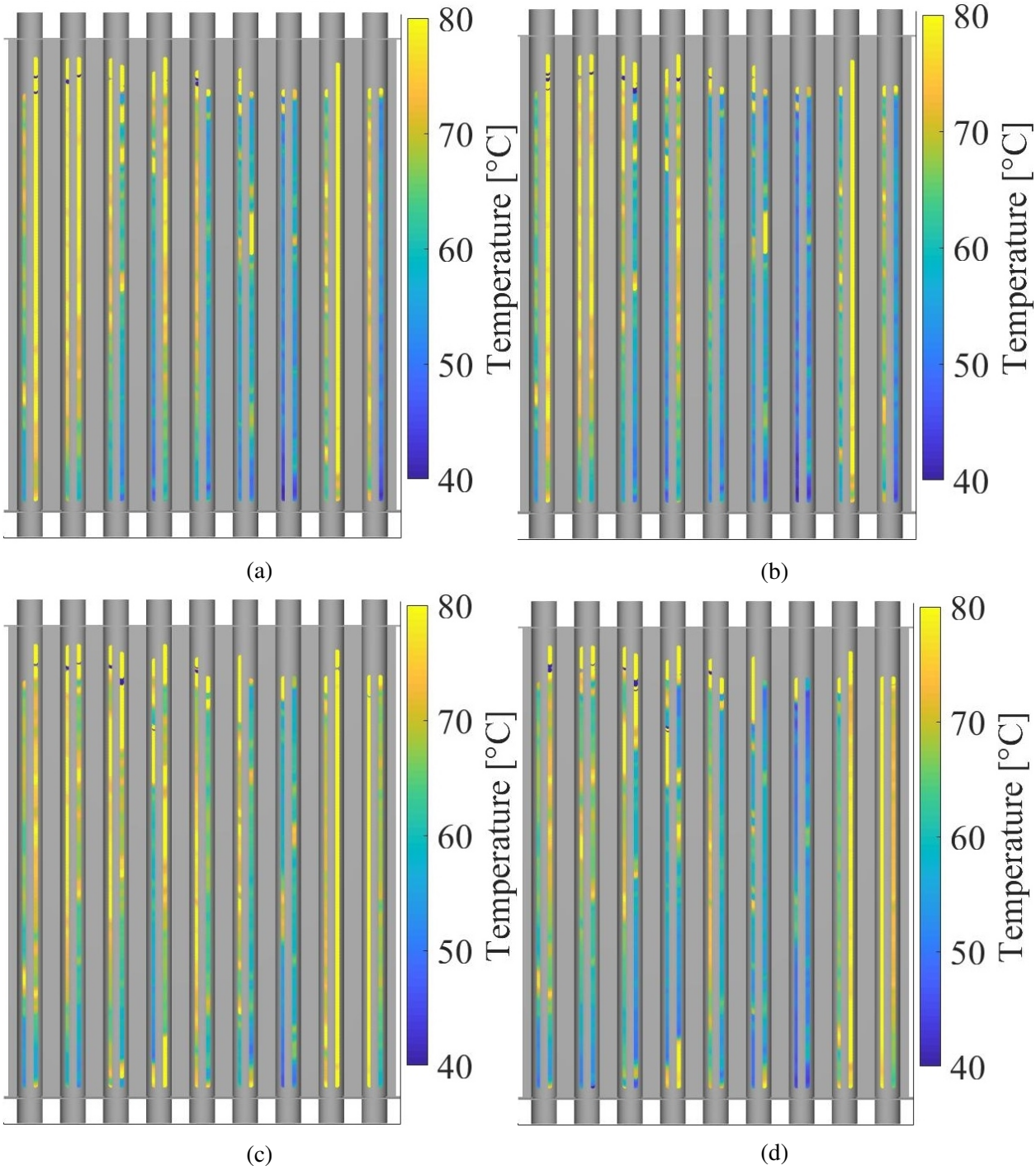

Figure 7.6: Time-averaged DTS measurements recorded during steady-state testing of WRCCS.

These results were less than adequate and needed improvement. No discernible differences are seen between flow conditions, although at the time it was not clear what differences would be

observed. Significant bowing of the capillaries is indicated by high-temperature recordings in short segments, and is present in each plot in Fig. 7.6. In some areas of the plotted data, the gradients adjacent to bowed sections of capillary are so steep that they caused the ODiSI-B to return a false reading. These false readings are indicated by large negative values, typically -1500°C. These obviously false readings can easily be filtered, but the data shown in Fig. 7.6 would need much more filtering than a simple cutoff. Instead of analyzing the data further, a consensus was reached to modify the steel riser panel for a more robust DTS installation.

The installation method used to obtain the data in Fig. 7.6 was also not as precise as it should have been due to the presence of wall-mount thermocouples on the riser pipe walls. Many of these thermocouples were installed with epoxy or cement adhesives, which tend to spread during curing. This spreading of adhesive affects a much larger area around the installed thermocouple sensor, which for wall-mount applications is essentially a wire junction. The spreading of adhesive prevented the DTS from being installed in precise, consistent locations.

Uncertainty in the DTS measurements was also higher for the data in Fig. 7.6, due to the method of reference temperature recording. The Fluke® 1524 and 5615 reference thermometer and probe were not available until after these measurements took place. The reference measurement for the data in Fig. 7.6 was obtained by averaging the first readings of the thermocouple probes in the riser columns, which have an uncertainty of 1.1°C. Following Eq. 6.1, the uncertainty for the data in Fig. 7.6 becomes 2.5°C.

7.5 Method Refinements

It became clear that capillary tension would be necessary to obtain acceptable surface temperature measurements in this facility. Capillary tension was achieved with small springs, stop collars, and ferrules. The cooling panel was removed from the facility in order to install the capillaries close to the cooling panel wall and hold them under tension. Figure 7.7 shows the removal of the cooling panel from its normal position. A small winch was attached to structural framing above the panel and connected to the panel with tow straps. The panel was then let down slowly until it rested horizontally on supports.

Figure 7.7: Removed cooling panel from WRCCS facility.

After two fiber segments were installed on one fin and one riser wall each, the cooling panel was lifted back into place and the insulated cavity was put together. The glass manifolds were out for repair and modification, so the heaters were set to a low power ($\sim$10%) and the system was allowed to reach steady conditions. Figure 7.8 shows the results of this simple test. The smooth temperature profile indicates a successful DTS installation, although the absolute values cannot be confirmed with thermocouples recordings.

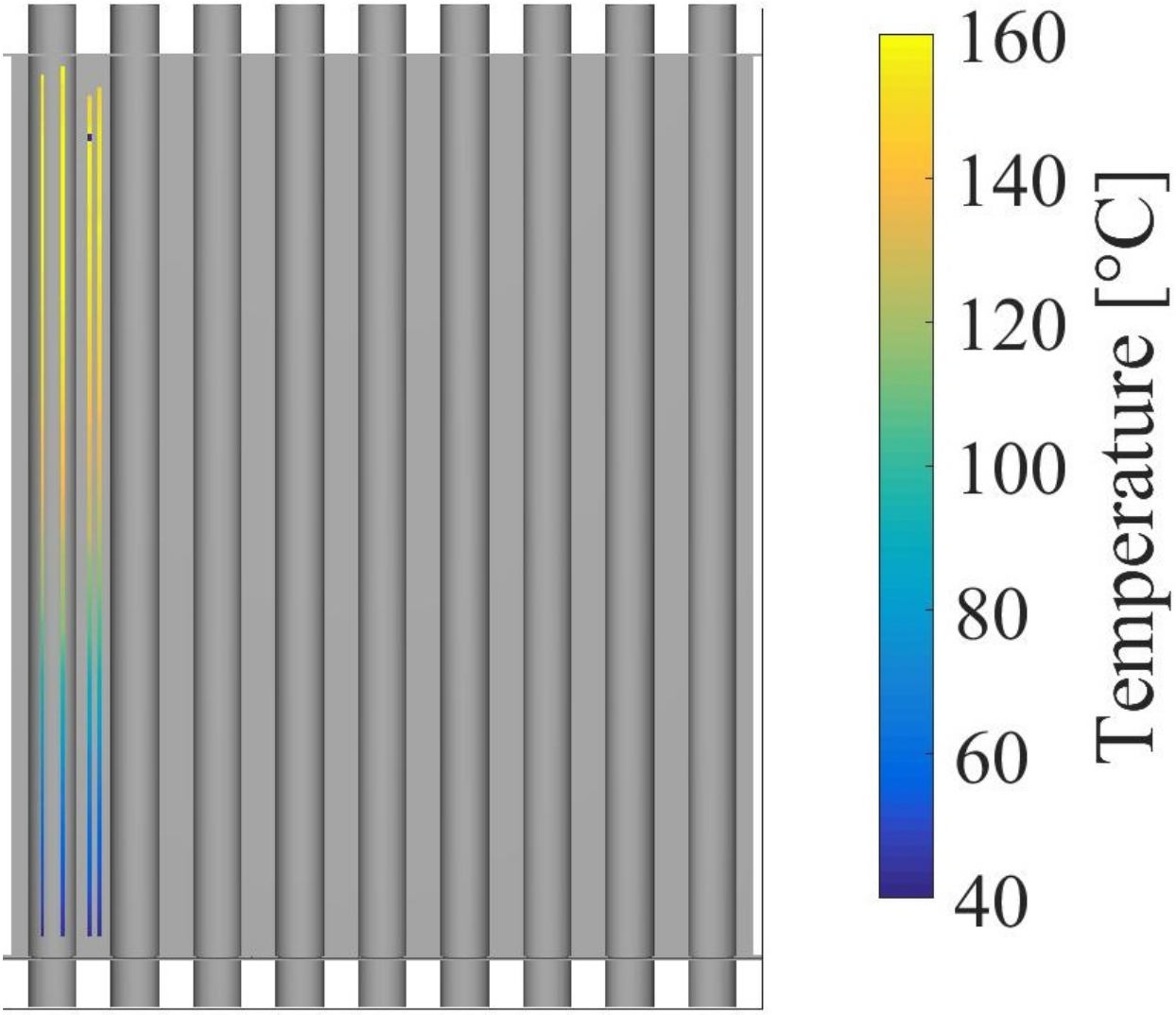

Figure 7.8: Temperature measurement on WRCCS cooling panel wall during test with no manifolds attached.

Re-installation of thermocouple probes in the water columns was also done at this time. The previous thermocouple probes had been secured with 1/16 inch tube fittings, using stainless steel ferrules. These metal ferrules create a permanent bond. Several of the previous probes were unresponsive, and many were not located near the center of the riser pipes. New probes of the same characteristics (1/16 inch dia., Type-K SLE) were secured in the riser pipe centers with the same fittings, except different ferrules were used (see Figure 7.9). The new ferrules were made of

PTFE, and when used properly, allow the user to adjust probe depth between experiments. These PTFE ferrules are rated for 200 psi, which is far above the hydrostatic pressure head in the WRCCS facility (22 psia).

Figure 7.9: Thermocouple placement in riser column of WRCCS facility.

The final installation of surface DTS on the WRCCS cooling panel wall included tension on the capillaries. Fibers were also installed on the riser fins. Figures 7.10 and 7.11 are close-up views of the final surface DTS installation. Four fibers covered each riser pipe and fin twice, yielding 34 total fiber segments available. The fibers' total length ranged from 13.2596 to 15.8535 m. All wall thermocouples (Type-K SLE) were replaced to allow the precise installation of DTS.

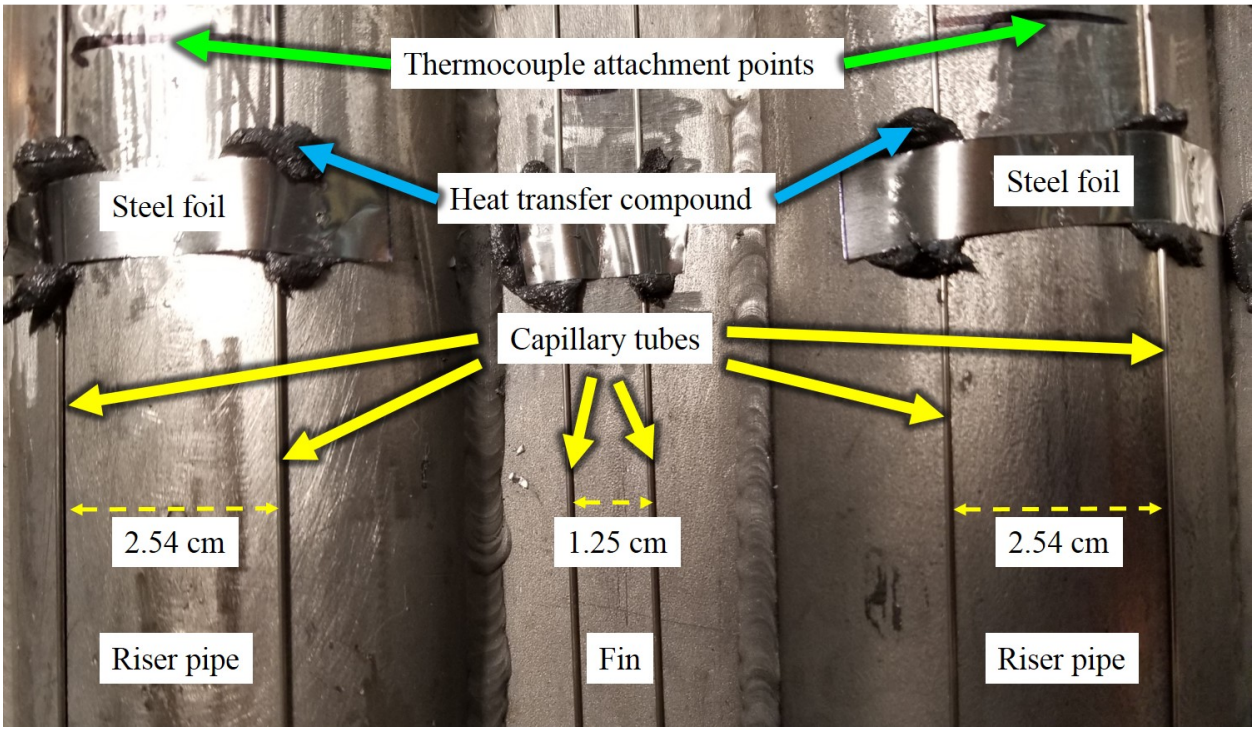

Figure 7.10: Close-up view of installed DTS on WRCCS cooling panel wall, second round of testing.

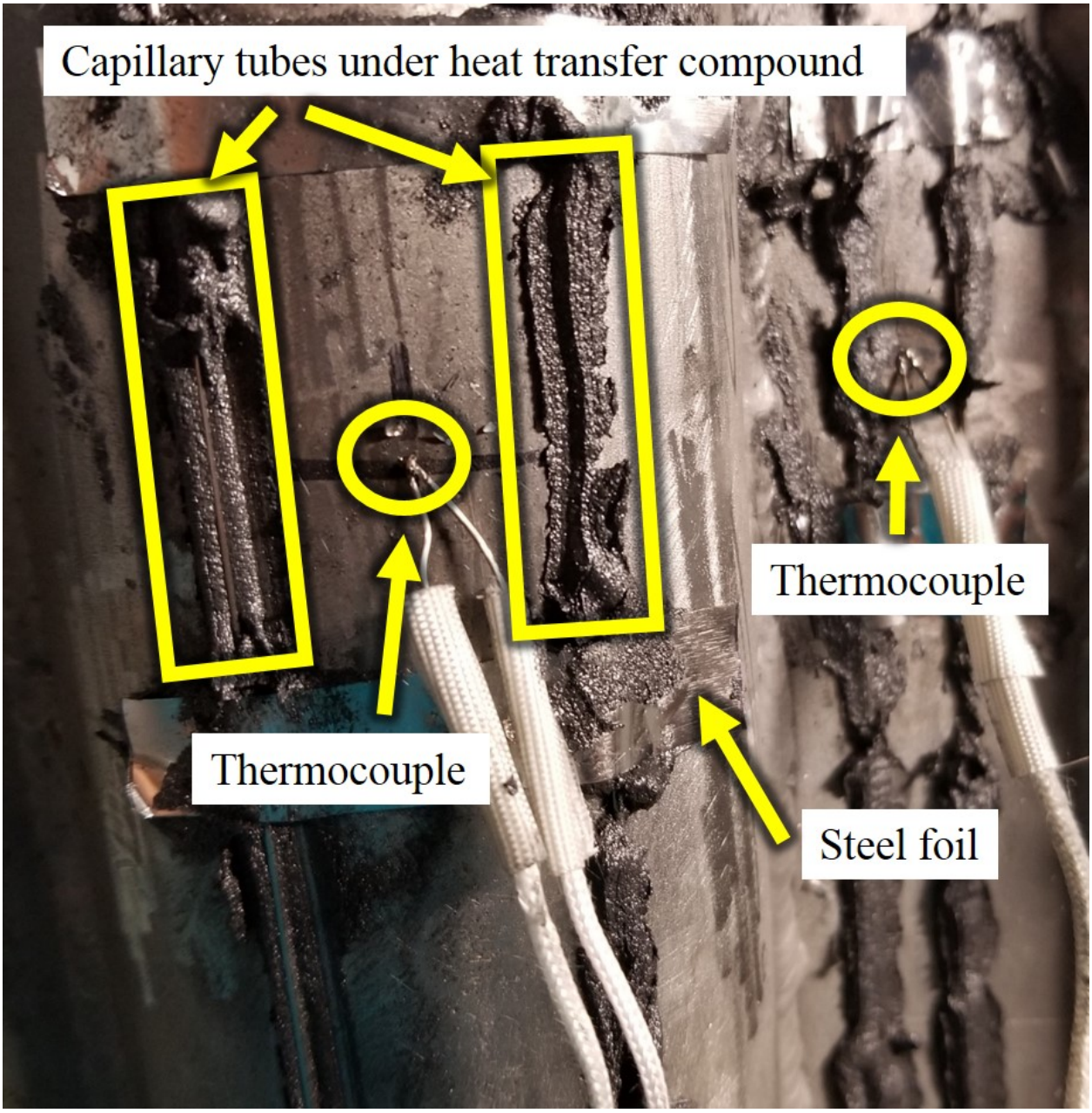

Figure 7.11: Close-up view of installed DTS on WRCCS cooling panel wall, second round of testing.

The capillaries were put under tension via springs and stop collars above a support plate on the cooling panel, as shown in Figure 7.12. These springs can be adjusted between tests.

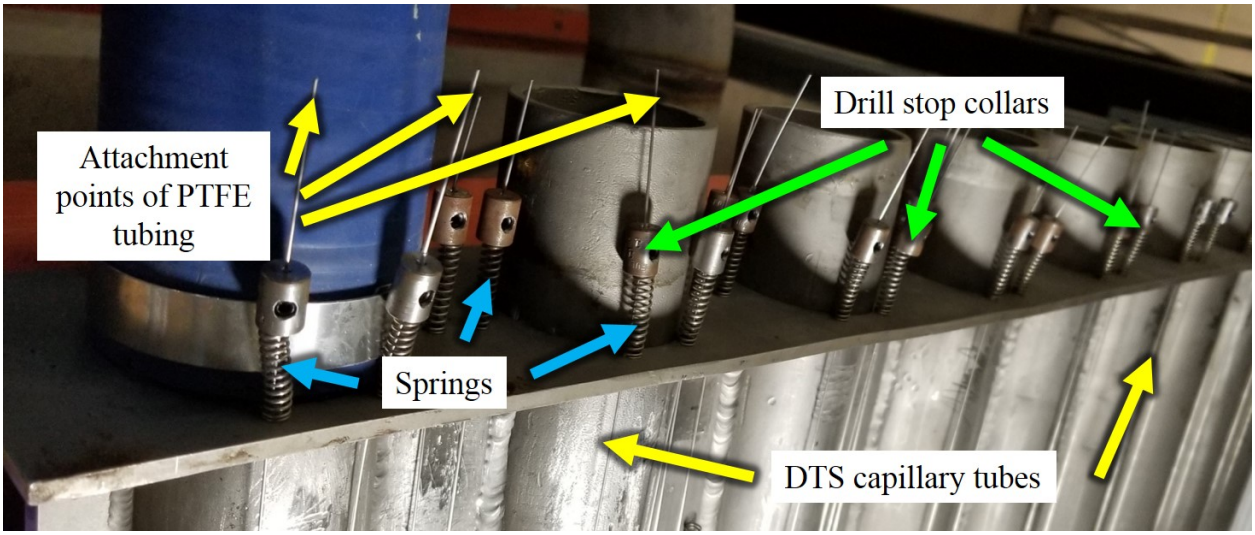

Figure 7.12: Springs and stop collars for applying tension to DTS on WRCCS cooling panel wall.

The capillaries were held in place through the support plate at the bottom of the cooling panel. As the 21 ga. capillaries pass through this plate, they were sleeved with short sections of 18 ga. tubing. The annular gap between these tubes was filled with epoxy. Stainless steel ferrules were then tightened onto the outer sleeves, creating a simple stopping mechanism. The capillaries were then threaded through drilled holes in both support plates and put under tension. Tension was left on the capillaries for several days before heat transfer putty and steel foil were applied.

7.6 Final Results

The final surface DTS installation was evaluated with one test encompassing two steady conditions, which were set with the tank valve positions of 25% and 100% open. Figure 7.13 shows a time history of the flow rate and the inlet and outlet temperatures during this test, and Table 7.4 lists the main events of this test. These conditions provide the most contrast in system behavior, and are useful for evaluating any modifications to the WRCCS facility.

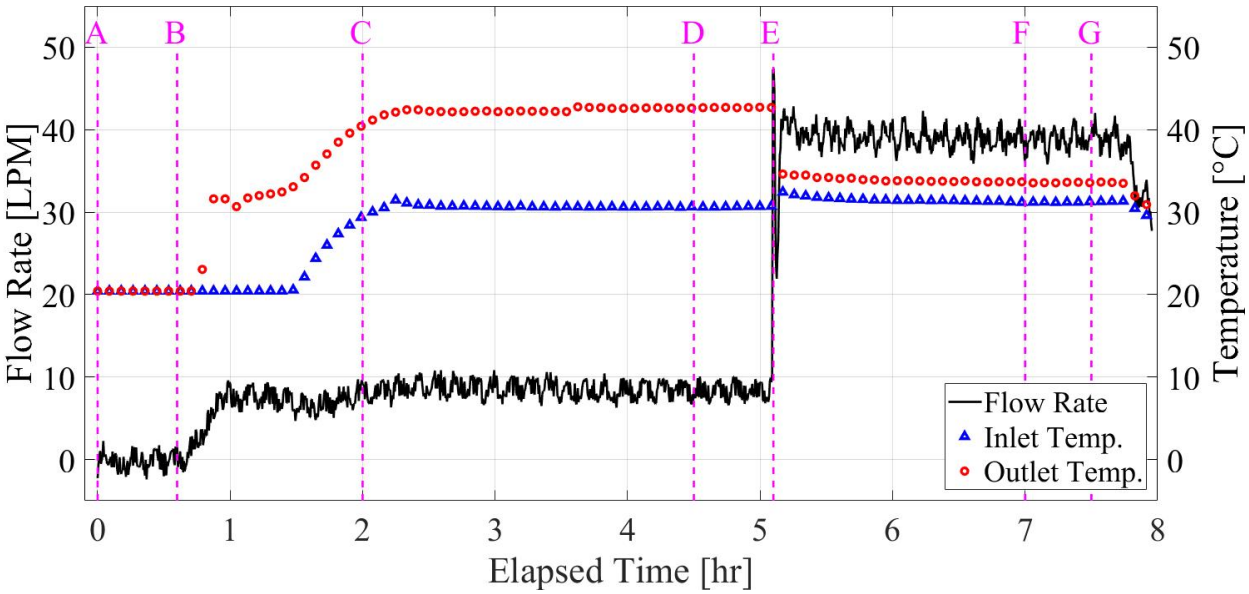

Figure 7.13: Main facility parameters recorded during steady-state testing of WRCCS with second installation of DTS on panel walls.

Table 7.4: Descriptions of events in Fig. 7.13.

Event	*Time* (hours)	*Description*
A	0	Data recording start; Tank valve opening = 25%
B	0.6	Heaters on (6 kW)
C	2.0	Secondary loop chiller on
D	4.5	Steady conditions reached; DTS data recording start
E	5.1	DTS data recording end; Tank valve opening = 100%
F	7.0	Steady conditions reached; DTS data recording start
G	7.5	DTS data recording end; Heaters off (end of test)

This data is very similar to the data presented in Fig. 7.5(a,d) and confirms that the facility has been operated in a similar manner. The repeated acquisition of similar data proves the reliability and reproducibility of the WRCCS facility.

The slightly larger than usual difference between outlet and inlet temperature seen in Fig. 7.13 is likely due to a slightly smaller tank valve opening, which is only coarsely controlled. The tank valve position of 25% can be difficult to set, due to its proximity to the valve's 0% (closed) position. The valve adjustment mechanism tends to become unreliable when adjusted to 25%, and can sometimes become closed. This exact situation occurred during a shakedown test early on, where the outlet temperature reached approximately 60°C before the valve was adjusted.

Figure 7.14 shows the time-averaged temperature recorded by the second installation of DTS on the wall of the cooling panel during two steady conditions.

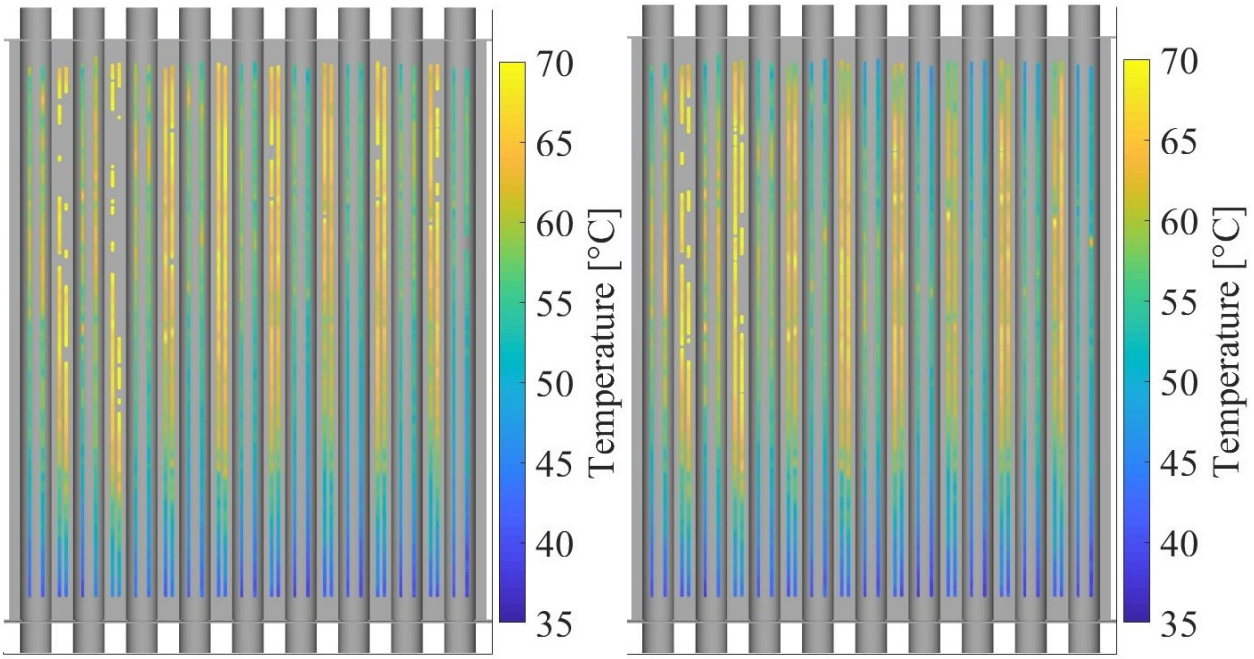

(a) (b)

Figure 7.14: Time-averaged DTS measurements (second installation) recorded on the WRCCS cooling panel wall during two steady conditions.

Semi-collocated Type-K thermocouples were available for comparison along the bottom of the DTS segments shown in Fig. 7.14. Figure 7.15 illustrates the labeling of the collocation points on each riser pipe and fin wall. Table 7.5 lists the thermocouple recordings available for comparison,

along with a brief statistical analysis of the data. All values are in degrees Celsius and have been time-averaged. Seventeen thermocouples were initially installed, but four became detached during testing. The subscript "SD" denotes the standard deviation of the data set.

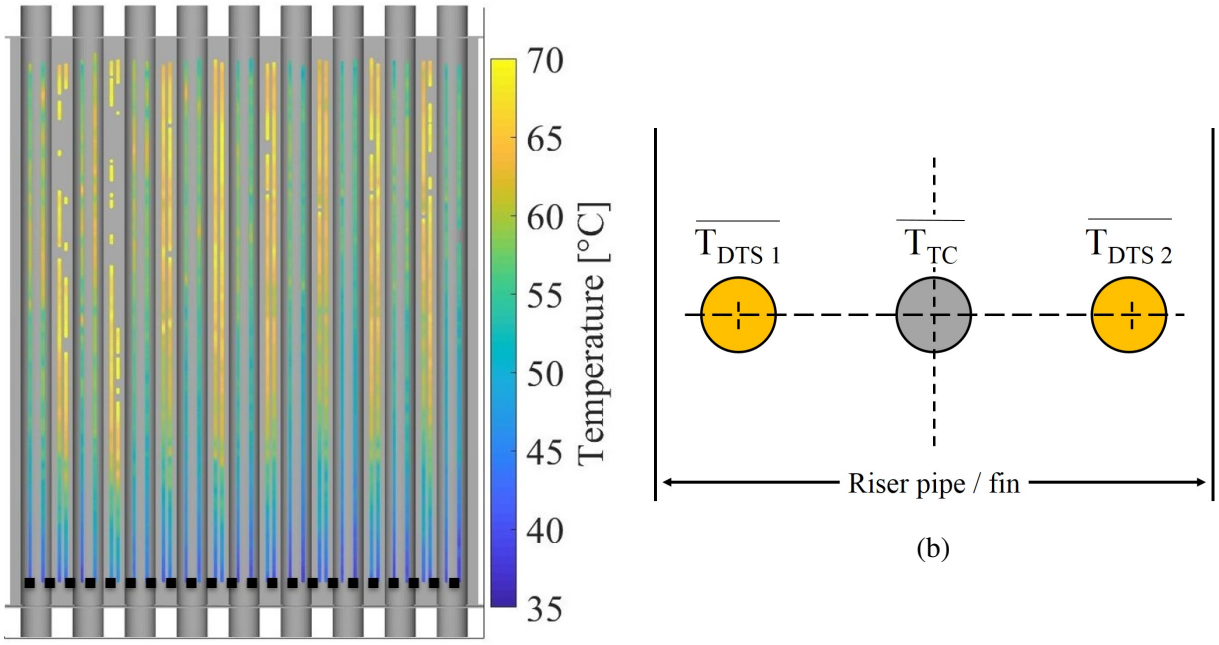

Figure 7.15: Collocation arrangement of thermocouples and DTS on each riser and fin near the bottom of the cooling panel.

Table 7.5: Comparison of recorded temperatures between thermocouples (TC) and DTS along the bottom of the WRCCS cooling panel.

Location	$\overline{T_{TC}}$	$\overline{T_{DTS1}}$	$\overline{T_{DTS2}}$	$\lvert\overline{T_{TC}} - \overline{T_{DTS1}}\rvert$	$\lvert\overline{T_{TC}} - \overline{T_{DTS2}}\rvert$
Riser 1	37.8	37.9	40.6	0.1	2.8
Fin 1	42.1	39.9	42.0	2.2	0.1
Riser 2	40.4	39.7	38.5	0.7	1.2
Fin 2	40.2	42.3	42.0	2.1	0.3
Riser 3	39.1	39.9	41.6	0.8	0.7
Fin 3	40.9	43.5	43.2	2.6	0.3
Fin 4	41.5	39.8	42.0	0.7	0.2
Riser 5	37.3	41.8	39.1	4.5	2.7
Fin 5	43.6	43.5	42.6	0.1	0.9
Riser 6	43.8	43.0	40.9	0.8	2.1
Fin 6	40.4	44.5	41.9	4.1	1.5
Fin 8	42.4	43.1	40.5	0.7	2.6
Riser 9	41.1	41.1	41.3	0.0	0.2
		$\lvert\overline{T_{TC}} - \overline{T_{DTS}}\rvert_{avg}$	$\lvert\overline{T_{TC}} - \overline{T_{DTS}}\rvert_{min}$	$\lvert\overline{T_{TC}} - \overline{T_{DTS}}\rvert_{max}$	$\lvert\overline{T_{TC}} - \overline{T_{DTS}}\rvert_{SD}$
		1.3	0.0	4.5	1.2

The fact that each DTS detected similar temperatures to those by the reference thermocouples each time it passed by the reference locations further confirms sensor integrity and correct overall functionality. The largest difference between thermocouples and DTS of 4.5°C is within the combined error bands of the DTS (±4.4°C) and TCs (±1.1°C). It must also be noted that the reference thermocouples are not exactly collocated with DTS, so slight temperature differences should be expected between sensors and may have contributed to the differences found.

It is possible that some unintentional mechanical strain was introduced to the encapsulated fibers. When analyzing the experimental data, the outlier DTS data was confirmed to have resulted from the capillary tubing separating from the cooling panel wall. As the capillary tubes bend outward,

they add mechanical strain to the fiber and move the fiber away from the surface into the cavity. Temperatures rise immediately from the cooling panel surface to the cavity air due to thermal resistance at their boundary. Therefore, an outward bowed section of capillary tubing can cause the fiber inside to experience both additional mechanical strain and higher temperatures. This reflects back to the fundamental issue of separating mechanical and thermal strain, but the combination of these effects makes outlier data easier to detect. The number of data points that we identified to be outliers as described above is less than 10% of the total data acquired during the test. The overall results obtained were determine to be very satisfactory with the current setup, proving the high spatial resolution that we wanted to achieve. Future refinements of the DTS installation technique presented may further reduce the number of outlier points.

8. WATER TEMPERATURE MEASUREMENTS

Several DTS were installed in liquid environments for this study. The liquid happened to be water in each case, but these installation techniques would not change for other liquids provided that the temperatures did not exceed 200°C.

8.1 The Water-Cooled Reactor Cavity Cooling System

The same WRCCS facility used for surface DTS measurements was used to implement liquid water DTS measurements. A full facility description can be found in Chapter 7.

8.1.1 Fiber DTS Installation

One optic fiber DTS was installed in a water column of the WRCCS facility. The complete installation is depicted in Figures 8.1 and 8.2. The fiber passes through the cooling panel and both manifolds, and is anchored with PTFE plugs and tube-to-pipe fittings.

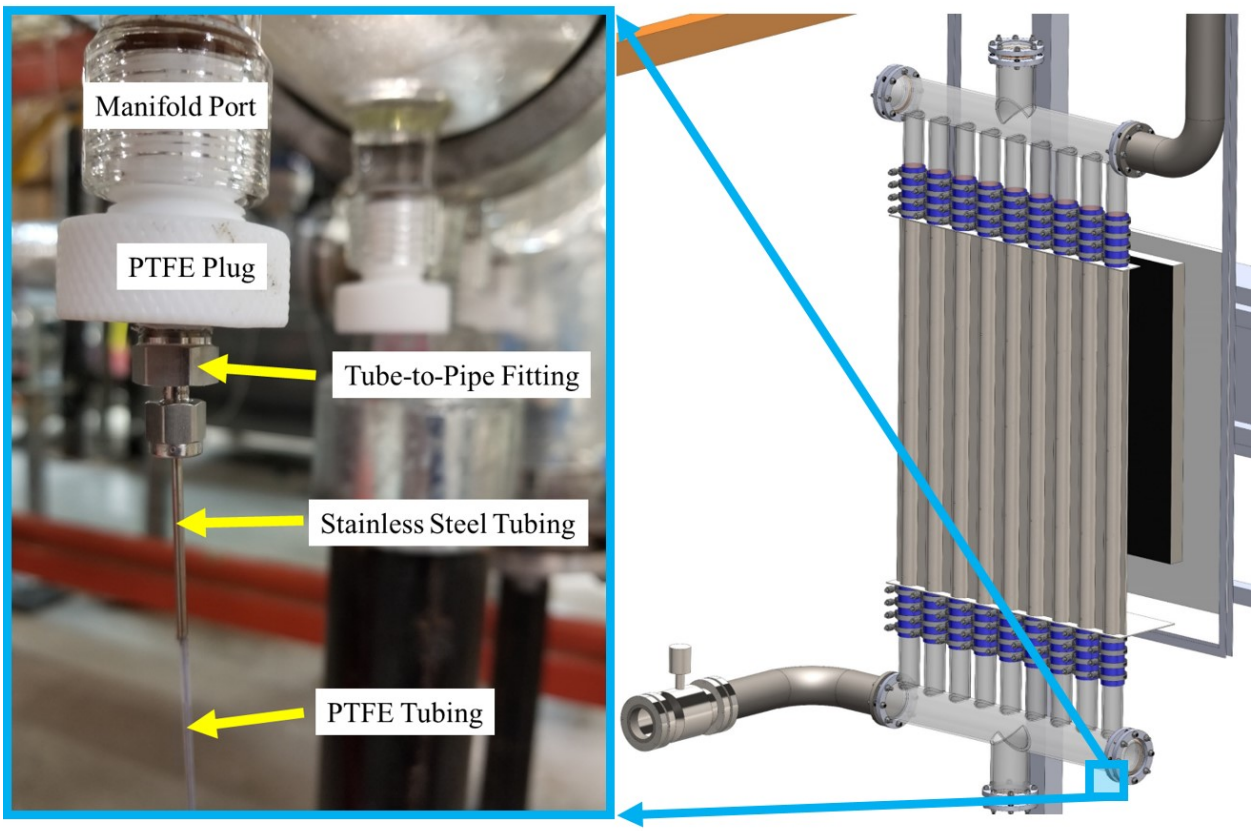

Figure 8.1: Installation of DTS at bottom of water column of Texas A&M WRCCS facility.

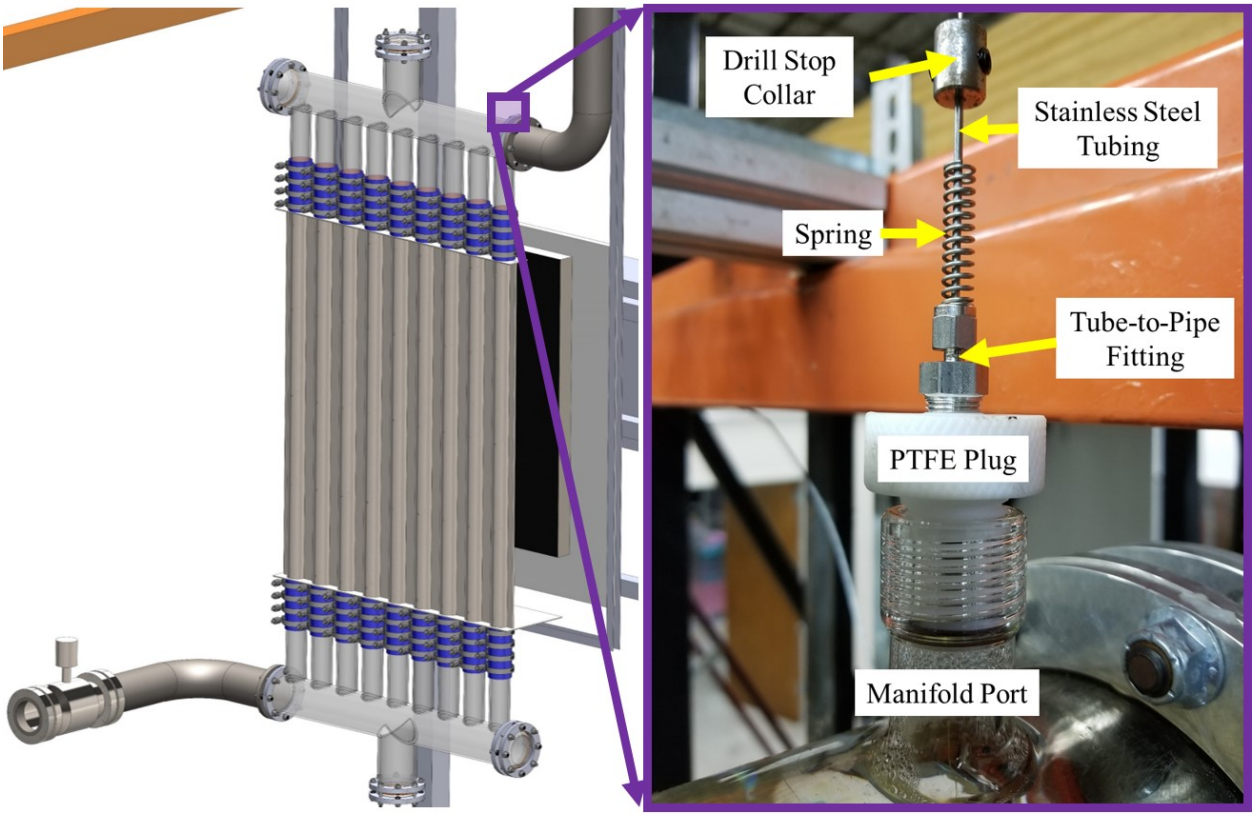

Figure 8.2: Installation of DTS at top of water column of Texas A&M WRCCS facility.

Epoxy was used to anchor the fiber concentrically inside sleeves of 21 and 18 gauge 304 SS tubing. At the bottom attachment point, stainless steel ferrules were used inside the tube fitting to create a permanent seal. In the top anchor point, removable PTFE ferrules were used inside the tube fitting. These PTFE ferrules have the same purpose as steel ferrules, except the PTFE ferrules do not tighten permanently onto tubing. If not over-tightened, they can be reused almost indefinitely. These ferrules can provide a seal at pressures up to 200 pounds per square inch.

The installation of DTS into this water column was made possible with modifications to the borosilicate glass manifolds. Figure 8.3 shows two photographs of the glass ports (Chemglass #15 Internal Thread, Part# CG-360-03) and PTFE bushings (Chemglass #15 Bushing, Part# CG-366-12) added to one of the WRCCS manifolds. These modifications were performed by Specialty Glass, Inc. and allow instrumentation (probes, DTS) to be inserted into the WRCCS water columns. The

PTFE bushings feature a front o-ring seal, which does not allow liquid into the bushing threads and provides a better seal.

(a) (b)

Figure 8.3: Addition of ports to WRCCS manifolds. The same modifications were performed on each manifold.

8.1.2 Facility Operation

Steady conditions were achieved with the same procedures described in Chapter 7. The transient operation of this facility involved the same startup procedures as steady-state testing, but the chiller and secondary loop are not activated until after all two-phase measurements and observations have been taken. This results in the water reaching $\sim$75°C at the lower manifold inlet. The primary loop was actively cooled after high-temperature tests were completed.

8.1.3 Steady-State Results

Figure 8.4 is a graph of the un-calibrated reponse of the water DTS in the WRCCS, recorded at the same steady conditions illustrated by Fig. 7.13. The only modification made to the DTS data was the addition of the reference (baseline) temperature. This DTS is located in the center of the leftmost riser shown in the surface measurements in the previous chapter. Throughout experimentation, this riser was referred to as "Riser 9". Each riser pipe has five thermocouple probes installed at different vertical locations. The five thermocouples in Riser 9 have been numbered 1 through 5 for the remainder of this study. The numbering scheme of the riser pipes and fins follows the general coolant flow direction, which is from right to left in the three-dimensional measurement plots of the previous chapter (i.e., Fig. 7.14).

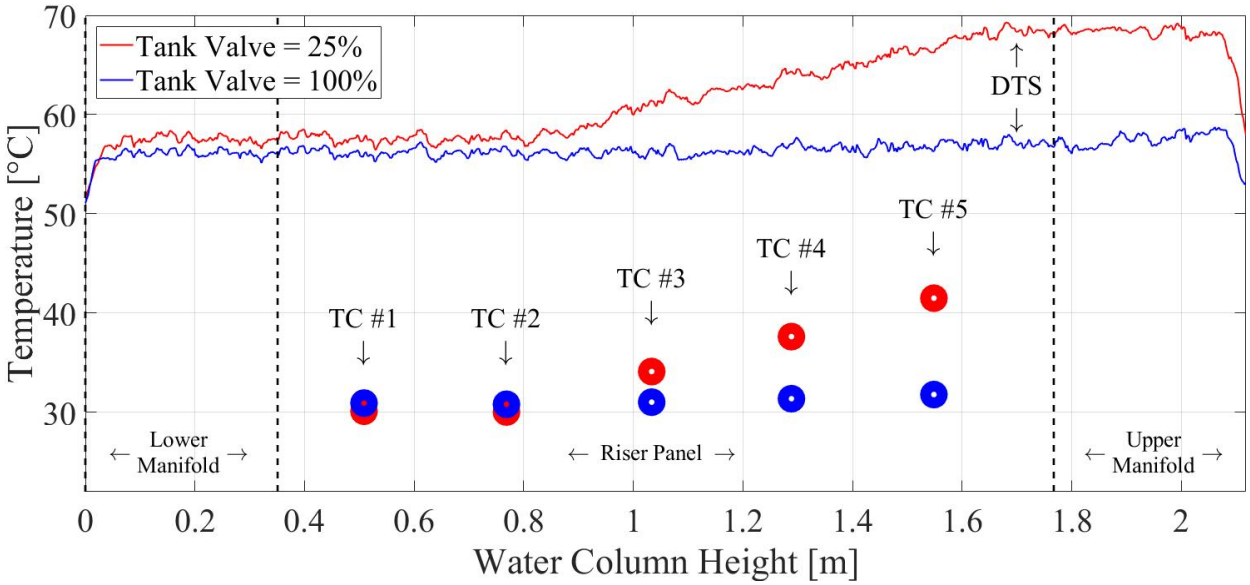

Figure 8.4: Un-calibrated water DTS response during steady conditions in WRCCS test.

These responses are obviously not indicative of the actual water temperature. The thermocouple recordings indicate much lower actual temperatures. Since the thermocouple probes are not sensitive to water or humidity and were calibrated with an accurate reference thermometer, their recordings can be considered to be close to the real temperature.

The larger values of temperatures recorded by the DTS are partly due to the hygroscopic fiber coating. This coating swells as it absorbs moisture, applying additional strain to the fiber. A few DTS application studies - including the current study - have estimated the error due to relative humidity, but this error is limited to DTS in air environments. Immersion in water is the equivalent of 100% absolute humidity. Absolute humidity is not normally used to describe environments because it requires knowledge of the total masses of air and water in a volume. These masses are virtually impossible to measure for large scale systems, such as the Earth's atmosphere. The mass of water in the WRCCS can be estimated, but this may not be practical if the DTS is only affected by the water immediately surrounding it. This further highlights the impractical nature of absolute humidity, and suggests that another parameter should be used to quantify the response of polyimide-coated DTS in liquid water.

The thermal expansion by the WRCCS facility components is another possible source of additional strain applied to the water DTS. The riser water columns in the WRCCS facility include sections of both borosilicate glass manifolds and the 304 SS cooling panel. These materials have different coefficients of thermal expansion, but would together impose a positive strain on the DTS. The linear coefficients of thermal expansion for 304 SS and borosilicate glass are 18 μ/m-K and 3 μ/m-K, respectively. Since the fundamental measurement mechanism of this DTS is based on Rayleigh scattering, it is impossible to directly separate these effects without further experimentation.

The response of the DTS is in conspicuous need of correction, which was accomplished with linear correction curves. Figure 8.5 contains plots of the DTS correction curves for this data.

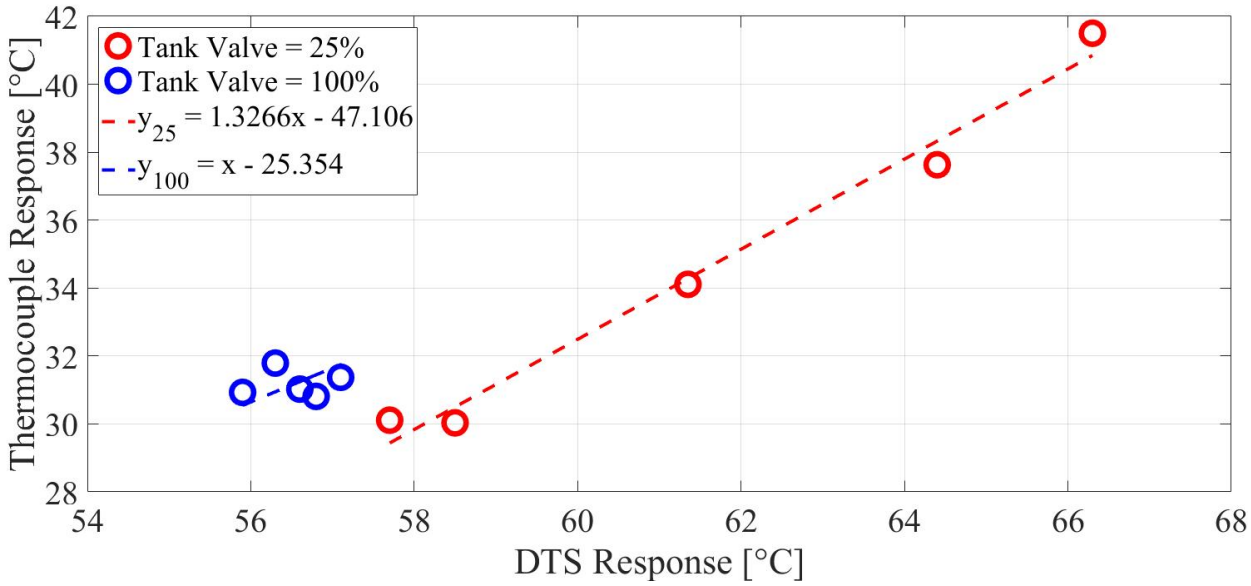

Figure 8.5: Correction (calibration) curve of DTS for steady conditions in a WRCCS riser column.

The good fit of a linear correction curve to this data suggests that both the overall thermal expansion and the water absorption rate of the polyimide fiber coating is linear and well-accounted for in this temperature range.

The presence of two different linear corrections suggests that the effects of water immersion

on polyimide-coated DTS are more dependent on temperature than time. Water vapor absorption characteristics of polyimide are normally measured over days, as reported in an application note from ARLON Electronic Materials [141]. However, studies conducted over the length of days may not appropriately capture effects that are accounted for during tests completed in a few hours. Hu and Chen [142], Chen et al [143], and Akram et al [144] all studied the effects of water vapor absorption in polyimide, but did not study liquid water effects.

The correction curve shown in Fig. 8.5 was then applied to the water DTS data collected during steady conditions and is presented in Figure 8.6. The correction curve seems to reliably correct the data, and in doing so, provides a new temperature measurement of the water in the manifolds.

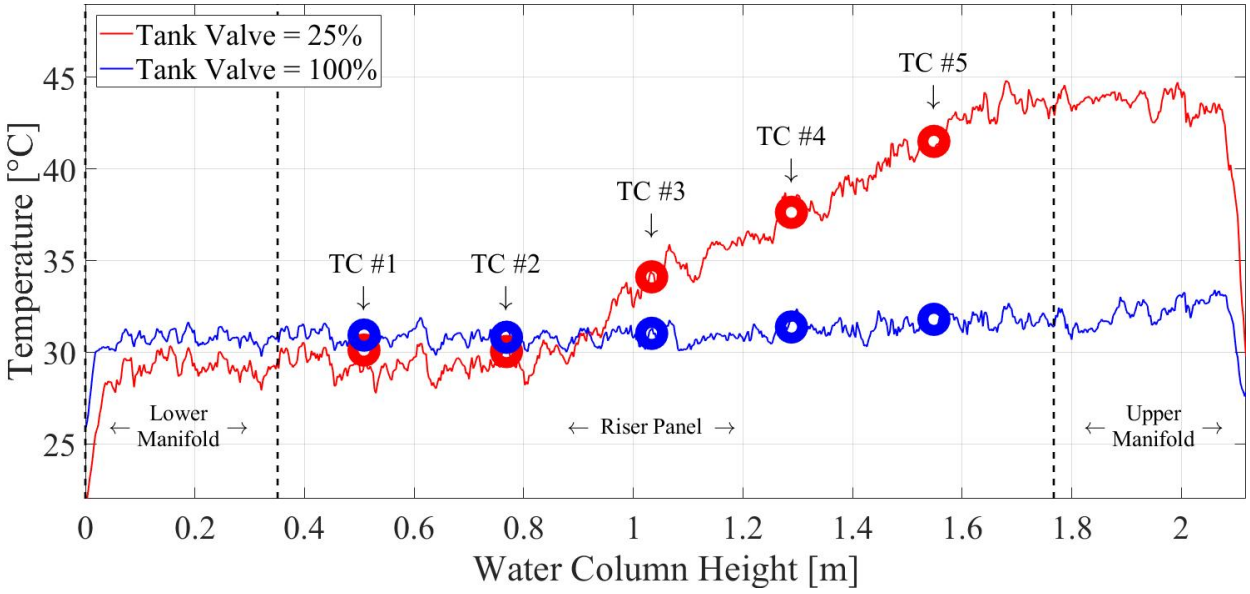

Figure 8.6: Water DTS data with correction curves applied.

Since the DTS extends through both manifolds, it can provide more insight into the temperature profile than thermocouples can. Both manifolds appear to be mostly isothermal, and the DTS has confirmed that the water temperature continues to increase after it passes the highest thermocouple, denoted in Fig. 8.6 as "TC $5". This thermocouple is located in the riser column but below the top of the cooling panel. This means it will not record the maximum water temperature of the water

column.

A second steady-state test of the WRCCS facility was performed at higher temperatures to verify the data shown in Figs. 8.4 - 8.6. Figure 8.7 shows the time history of the main facility parameters during this test, and Table 8.1 lists the major events.

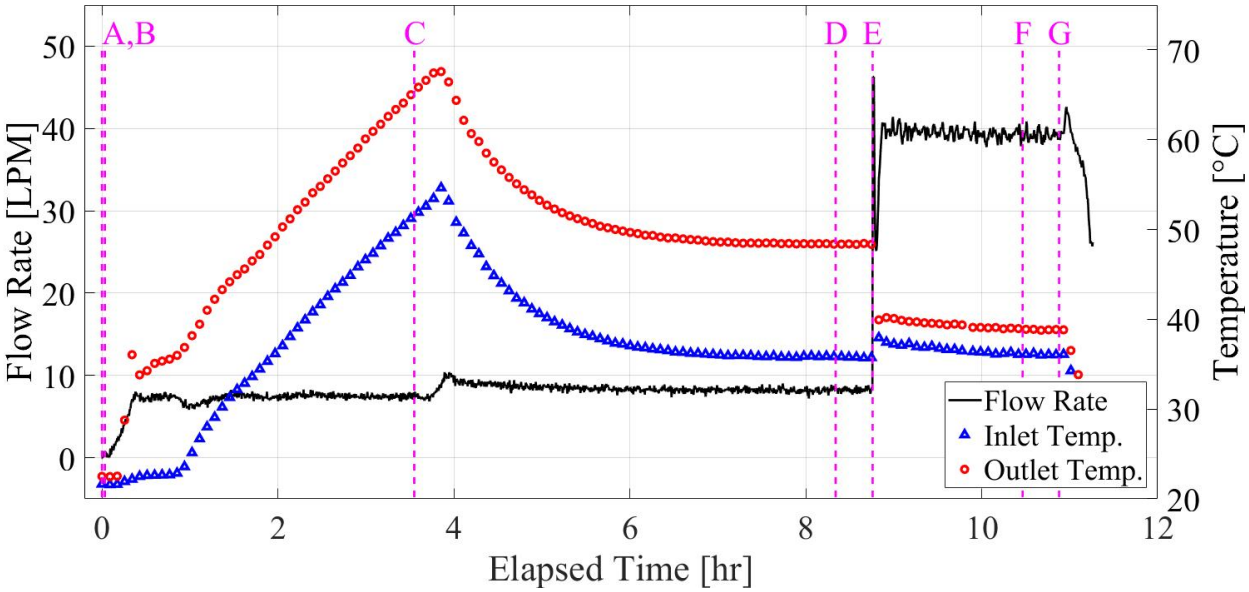

Figure 8.7: Main facility parameters recorded during second steady-state test of WRCCS.

Table 8.1: Descriptions of events in Fig. 8.7.

Event	*Time* (hours)	*Description*
A	0.00	Data recording start; Tank valve opening = 25%
B	0.05	Heaters on (6 kW)
C	3.55	Secondary loop chiller on
D	8.34	Steady conditions reached; DTS data recording start
E	8.76	DTS data recording end; Tank valve opening = 100%
F	10.5	Steady conditions reached; DTS data recording start
G	10.9	DTS data recording end; Heaters off (end of test)

Chiller activation was delayed for this test in order to reach steady conditions at a higher inlet temperature. The system has a slow response time, and this is the reason for the short continuation of temperature rise after chiller activation. At this higher-temperature steady condition, a larger difference between outlet and inlet temperatures formed. Table 8.2 lists the main facility parameters for the final two steady-state test performed. Both tests involved the same steady conditions (25% and 100% flow) and achieved them in the same order.

Table 8.2: Time-averaged main facility parameters during steady conditions in Figs. 7.13 and 8.7.

Figure	*Tank Valve Position*	$\overline{\dot{V}}$ (LPM)	*Re* (-)	$\overline{T_{In}}$ (°C)	$\overline{T_{Out}}$ (°C)
7.13	25%	11.6	3,063	30.6	42.7
	100%	42.2	11,283	31.2	33.6
8.7	25%	8.22	2,409	35.8	48.4
	100%	39.1	11,524	36.1	38.9

Figures 8.8 - 8.10 show the un-calibrated DTS response, the correction curve and the corrected response, respectively.

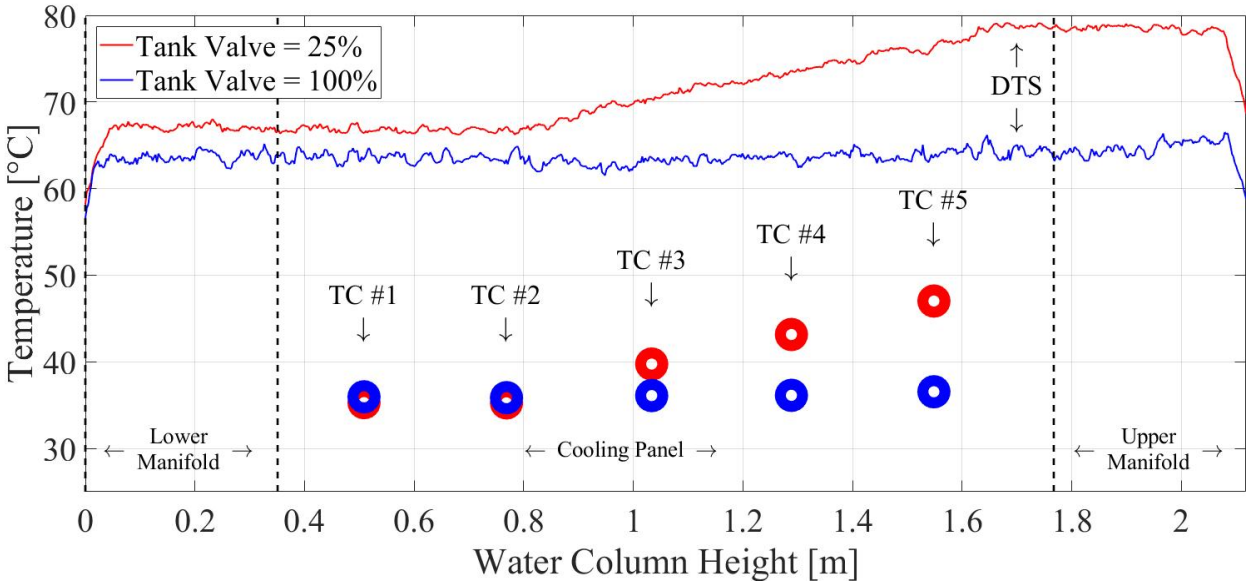

Figure 8.8: Un-calibrated water DTS response during steady conditions in second WRCCS test.

A consistent offset in DTS response between steady conditions in the lower manifold suggests that its cause is independent of DTS operation. The difference in DTS responses is likely due to the difference in overall temperatures between the steady conditions. At the low flow condition, the higher temperatures present cause more thermal expansion, and therefore a higher reading from the DTS. As the facility is allowed to become steady in the high flow condition, the facility cools slightly and imposes less strain on the DTS. Any additional strain imposed on Rayleigh backscatter DTS will add to the total response, which cannot be automatically separated into strain and temperature.

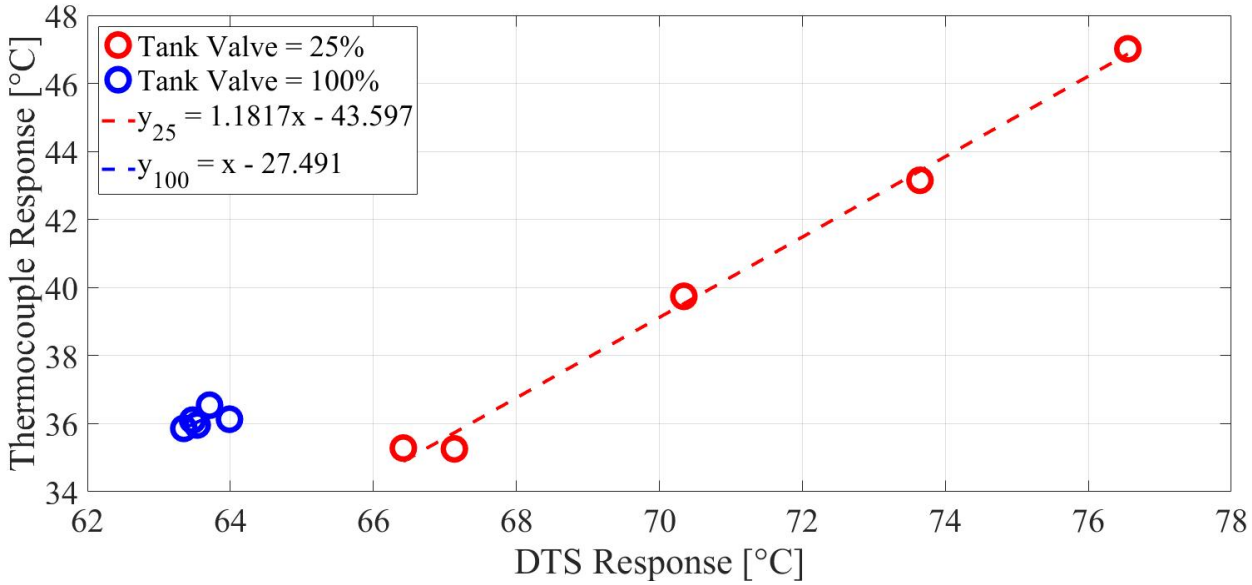

Figure 8.9: Correction (calibration) curve of DTS for steady conditions in a WRCCS riser column. Second test.

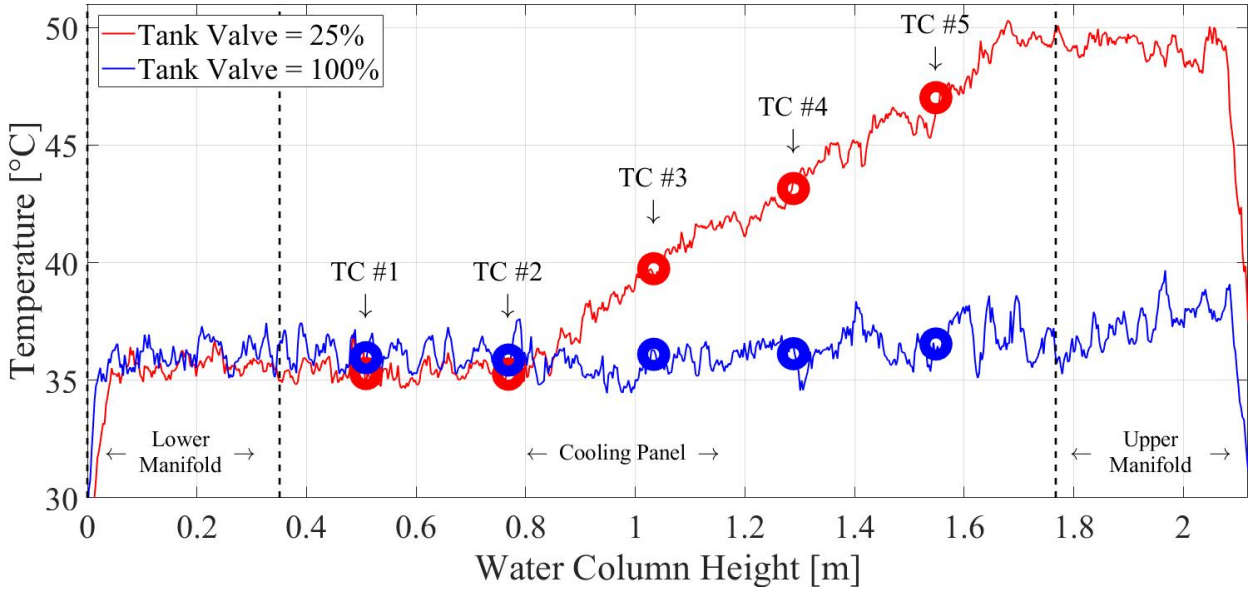

Figure 8.10: Corrected water DTS response during steady conditions in second WRCCS test.

These DTS correction curves are of the same form as before, suggesting that the formation of

a linear correction curve is appropriate. The DTS recording points located between and outside of thermocouple collocations also appear to have reasonable trends, suggesting that the correction methods would be valid for other experiments involving exposed DTS in water.

The DTS in small thermal gradients seem to only display an offset from the actual temperature, whereas the DTS in larger gradients seem to require a 1st-order correction. Table 8.3 compares both sets of correction curves found from both steady-state tests.

Table 8.3: Correction curves for WRCCS DTS in both steady state tests.

Test	*Tank Valve Position*	*Correction Curve*	*Correlation Coefficient*
1	25%	y = 1.3266x - 47.106	0.9835
1	100%	y = x - 25.354	-
2	25%	y = 1.1817x - 43.597	0.9949
2	100%	y = x - 27.491	-

The major limitation for completing this second test was the highest temperature allowed by the chiller, which is 80°F (26.7°C). This was not a limitation during previous testing, where the PVC secondary loop contained enough pressure losses to provide the correct amount of heat removal. After the high-temperature upgrades were completed (described in the next section), however, the flow path of the secondary loop became simplified and had fewer places where pressure losses could occur. This made the secondary loop a much more effective heat removal system, and the valve immediately downstream of the pump had to be throttled to stay within the limits of the chiller.

8.1.4 Transient Studies

Transient studies of the DTS response in the WRCCS facility were also performed. Figure 8.11 shows the recordings of the lowermost thermocouple in the riser column and the DTS at that point. Portions of the data that were extracted for use in correction curve efforts are labeled. The procedure for these tests followed those described in a previous subsection.

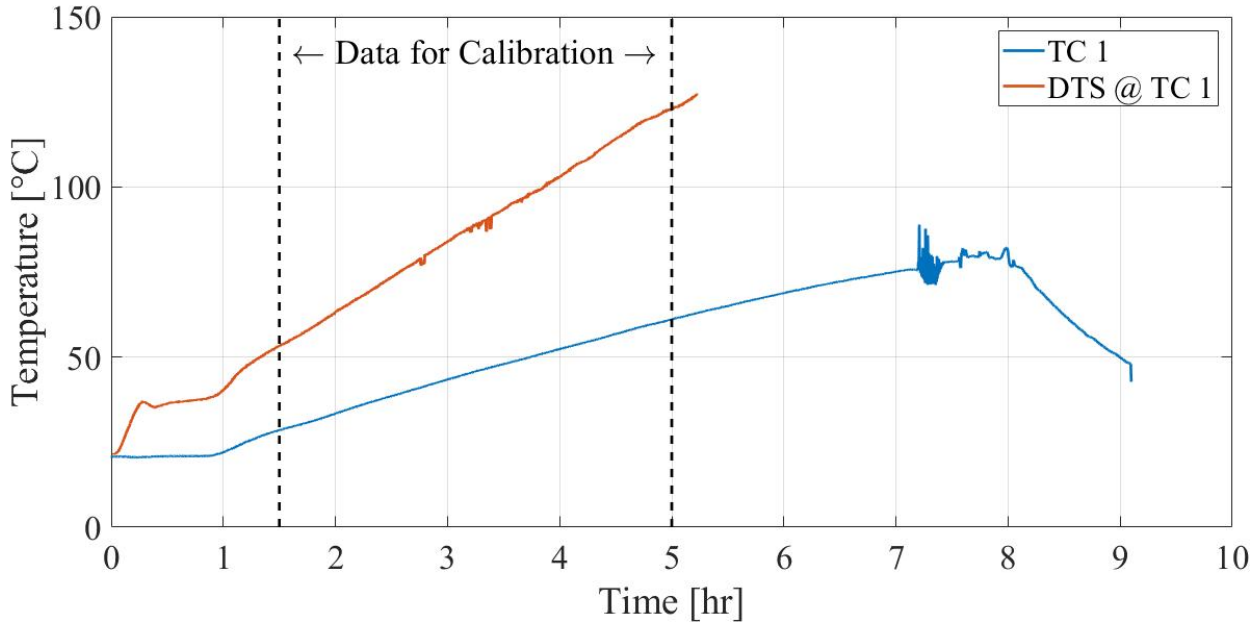

Figure 8.11: Comparison between thermocouple and DTS during transient in WRCCS riser column during a transient test.

The behavior of the DTS at the beginning of the test suggests that it is responding to the flow rate and possible thermal expansion of the facility, but this would be difficult to quantify. The DTS is inherently more sensitive than a thermocouple, but the DTS recordings at the beginning of the test (up to ∼45 min) seem to be related to the system flow rate. In the TAMU WRCCS facility, natural circulation in the primary loop is established relatively quickly, long before the system becomes steady. The fluid momentum convects through the system many times before the fluid's thermal energy starts to circulate. This phenomena is caused by the heat lost to facility piping and the atmosphere. The linear response of both DTS and thermocouples between 1.5 and 5 hours appears to be more correlated, so it will be compared for calibration.

Figure 8.12 shows comparisons at the other four thermocouples in this riser column. These five points in space were the only available points for comparison. All five of these thermocouple probes are located near the center of the riser column, where the DTS was installed.

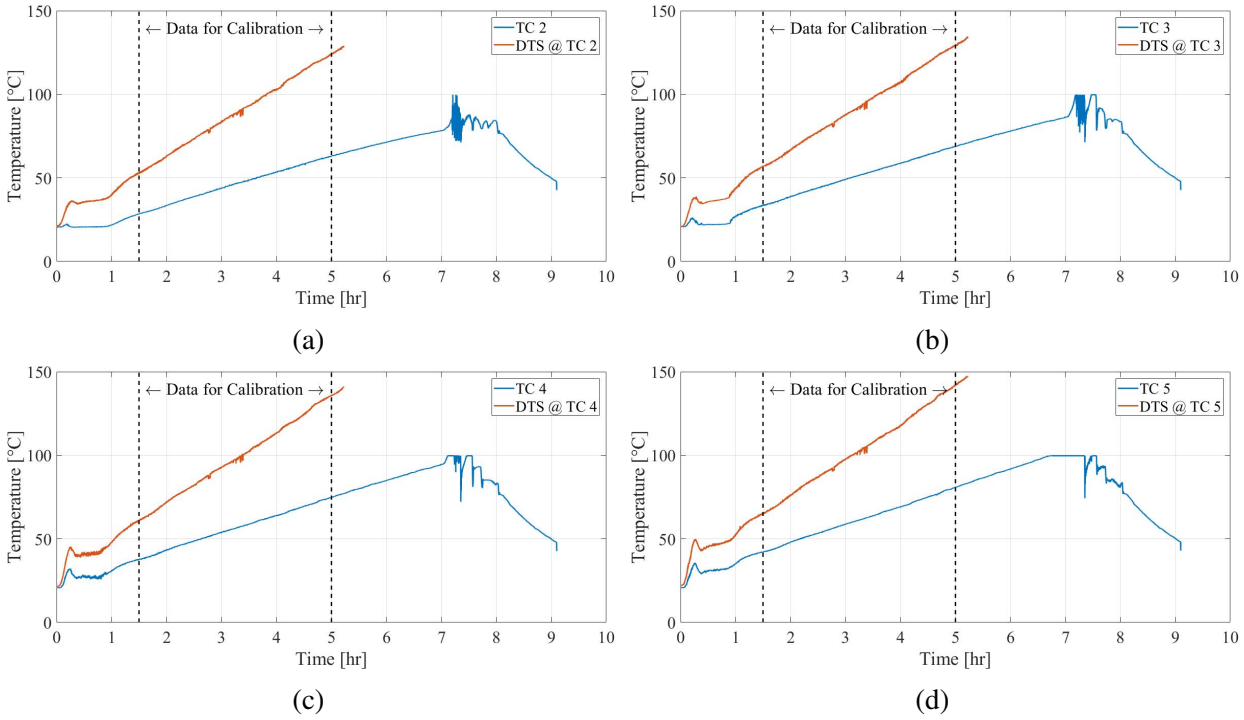

Figure 8.12: Comparisons between four thermocouples and collocated DTS in WRCCS riser column during a transient test.

High-temperature (>40°C) operation of this facility required the secondary loop piping to be replaced with 304 stainless steel pipe and vacuum-rated heater hose. Figure 8.13 shows labeled photographs of the upgrades to the secondary loop, which was previously made of only polyvinyl chloride (PVC) piping. All piping is 1 inch Schedule 40 304 SS, and all valves are full-port valves with PTFE seals.

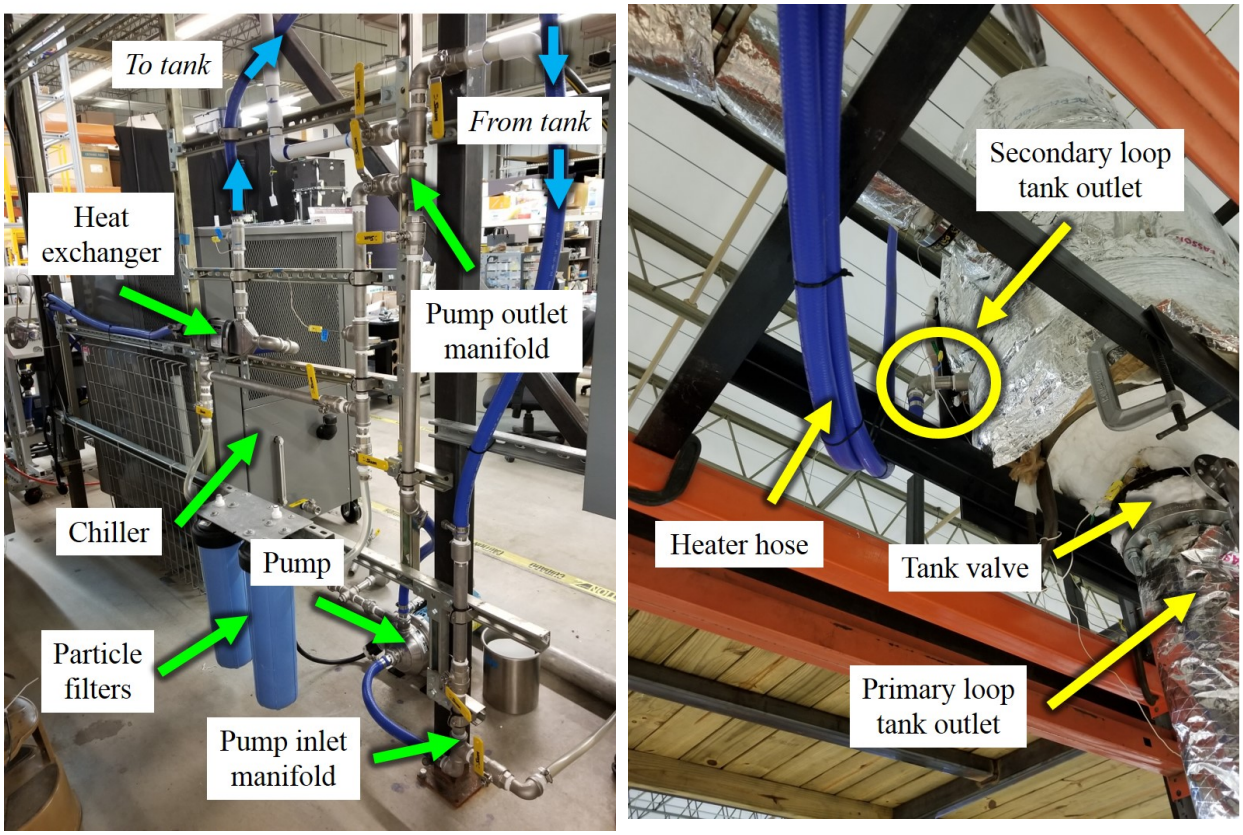

(a) (b)

Figure 8.13: Upgraded secondary loop piping in WRCCS facility for high-temperature testing. High-temperature materials replaced PVC throughout the ground floor (a) and second floor (b).

The data extracted from Figs. 8.11 and 8.12 was used to make correction curves, seen in Figures 8.14 and 8.15. These plot contains correction curves for each collocated thermocouple / DTS point (five total). The curves obtained with Figs. 8.14 and 8.15 are listed in Table 8.4.

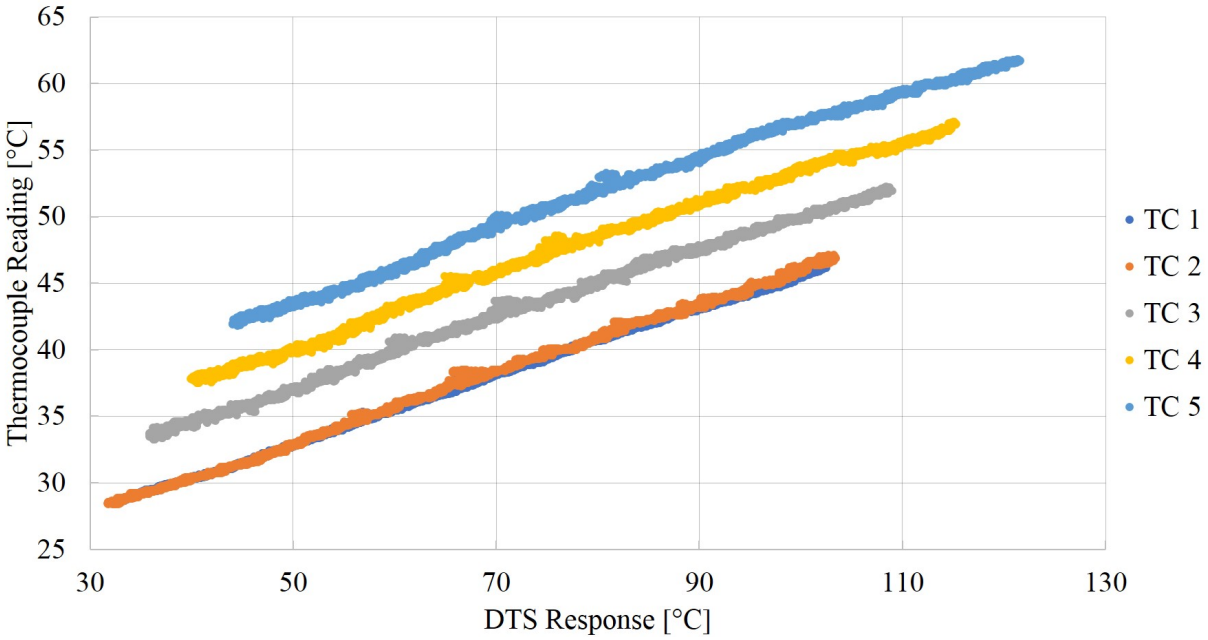

Figure 8.14: Correction curves for DTS response in WRCCS riser column during transient test.

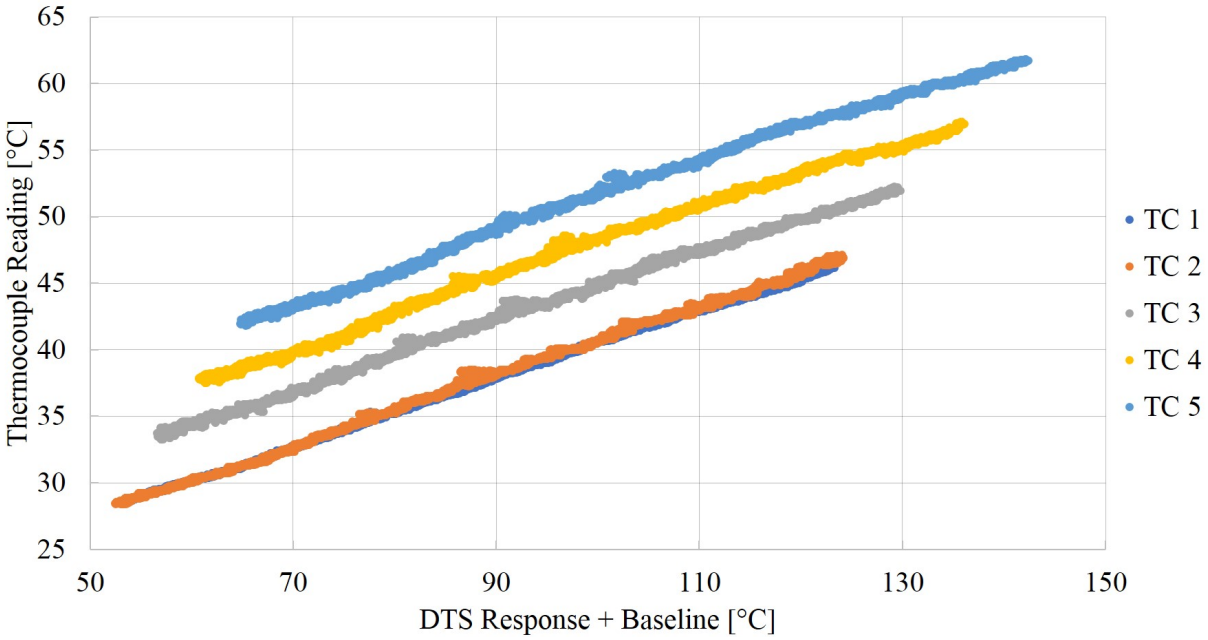

Figure 8.15: Correction curves for DTS response with added baseline in WRCCS riser column during transient test.

Table 8.4: Quantitative correction curves for DTS in WRCCS riser column during transient test.

Figure	*Collocation Point*	*Correction Curve*	*Correlation Coefficient (R^2)*
8.14	TC 1	y = 0.2544x + 20.224	0.9989
	TC 2	y = 0.2617x + 19.941	0.9984
	TC 3	y = 0.2571x + 24.398	0.9977
	TC 4	y = 0.2608x + 27.347	0.9957
	TC 5	y = 0.2620x + 30.671	0.9957
8.15	TC 1	y = 0.2544x + 14.937	0.9989
	TC 2	y = 0.2617x + 14.504	0.9984
	TC 3	y = 0.2571x + 19.057	0.9977
	TC 4	y = 0.2608x + 21.929	0.9957
	TC 5	y = 0.2620x + 25.227	0.9957

The linear character of the correction curves in Figs. 8.14 and 8.15 again suggests that both temperature and time have effects on polyimide-coated DTS response in liquid water. The slopes of the correction curves in Table 8.4 do not seem to be sensitive to temperature, but the intercepts certainly are.

Another comparison between thermocouples and DTS is illustrated in Figure 8.16. These comparisons are made with all five collocation points at select times throughout the data selected for correction.

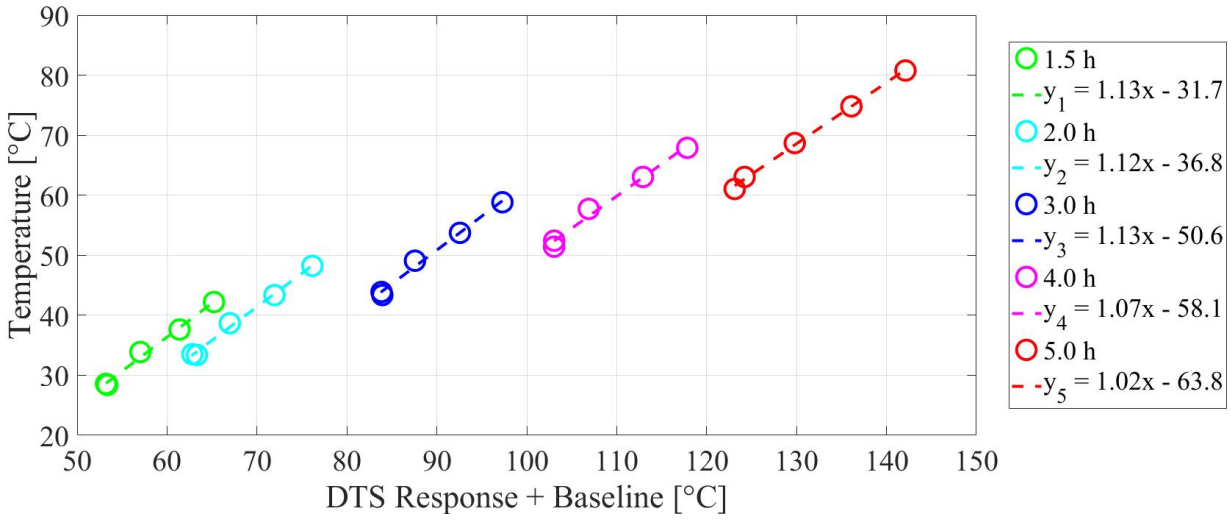

Figure 8.16: Correction curves for collocated DTS points (with added baseline) in WRCCS riser column at select times during transient test.

These curves suggest that the calibration slope becomes close to unity after a certain temperature has been reached. This is contrary to the results of the steady-state testing in the previous section, where the lower temperature conditions yielded a calibration curve with a slope of 1. These effects are likely caused by the combination of strain and temperature in the Rayleigh backscatter signal that cannot be separated with one fiber sensor. Due to the inconsistencies between calibrations, in-situ calibrations seem to be necessary for exposed polyimide-coated DTS in liquid water.

8.2 The HTGR Upper Plenum Facility

The scaled High-Temperature Gas-Cooled Reactor (HTGR) is another application of DTS, and is depicted in Fig. 8.17. This facility is a 1:16 scale model of an HTGR, but includes a transparent upper plenum to allow optical measurements to take place. The apparatus has two separate coolant loops, both of which use water. Isothermal and non-isothermal tests can be performed in this facility. The former use a pump in the primary loop, while the latter use natural circulation. Natural circulation in this facility is achieved by heating one or more of the 25 channels.

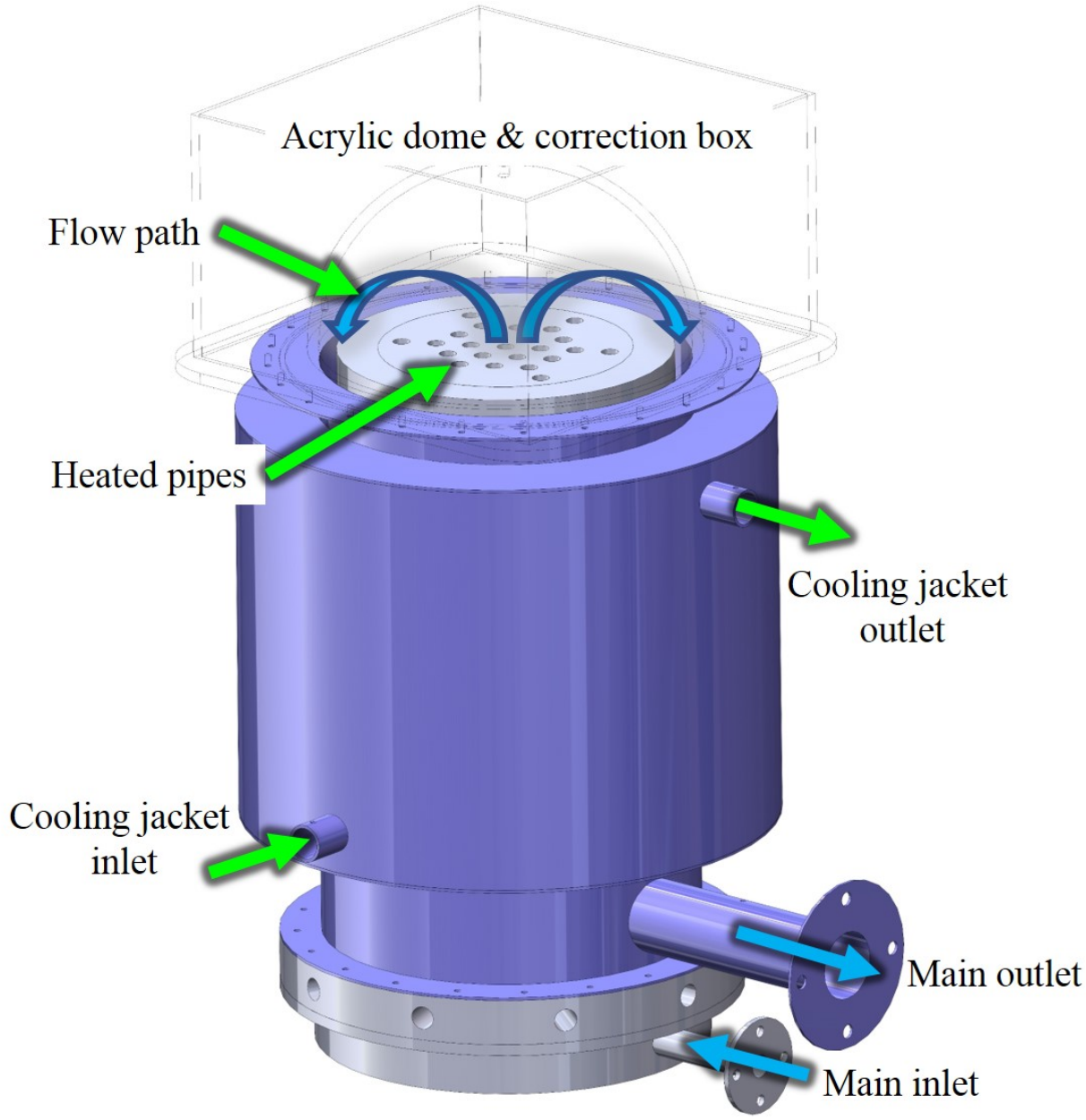

Figure 8.17: Scaled HTGR test section with labeled flow paths. Each loop has a dedicated stagnation tank.

The HTGR facility was designed to perform high-resolution velocity and temperature measurements of the water inside the acrylic dome. Particle image velocimetry (PIV) measurements have been performed, and laser-induced fluorescence (LIF) measurements are under way. However, one of the main drawbacks of LIF measurements is the inaccuracy of temperature measurements near

walls. Surfaces reflect the laser sheet back into the fluid, causing a non-physical measurement. Fiber DTS can serve to complement LIF and provide accurate temperature measurements on and near surfaces.

8.2.1 Fiber DTS Installation

Fiber DTS were installed inside the dome of the HTGR upper plenum facility. Figure 8.18 shows before (a) and after (b) photos of one DTS installed around the dome's inside peak (sheathed in 21 RW capillary tubing). The capillary tubing has been wound into approximately 6 concentric circles onto the wall, all with a 1 cm pitch.

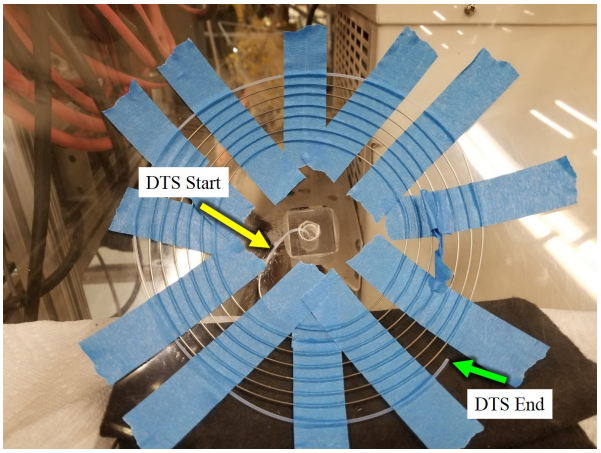

(a)

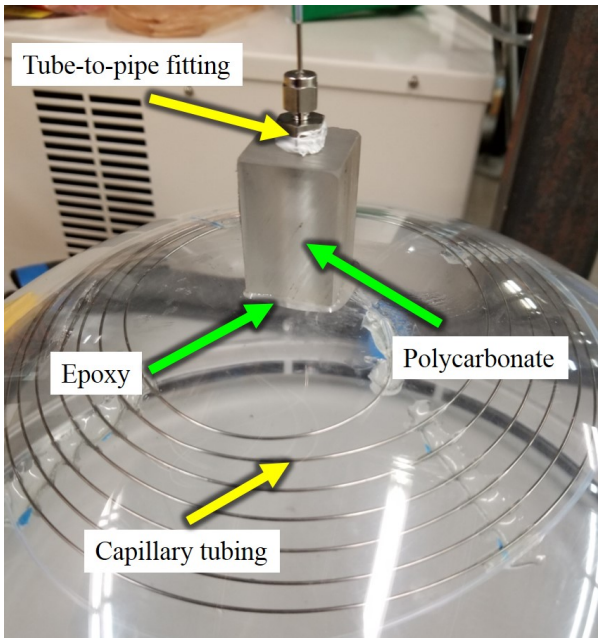

(b)

Figure 8.18: Installation of DTS around inner ceiling vertex of the HTGR upper plenum facility.

The second DTS installed in the HTGR upper plenum facility was in one plane crossing the center, inside the fluid. Figure 8.19 includes photographs of the installation of capillary tubing and fiber in this dome. The cloudy dome in Fig. 8.19(b) is from condensation on the inner surface after testing. The fluid DTS was also sheathed in 21 RW 304 SS capillary tubing, and strung across the

center of the dome. Springs and stop collars hold tension on the capillaries, which are sealed inside side supports with silicone. The side supports were necessary to provide a flat surface to ensure the springs stayed in place.

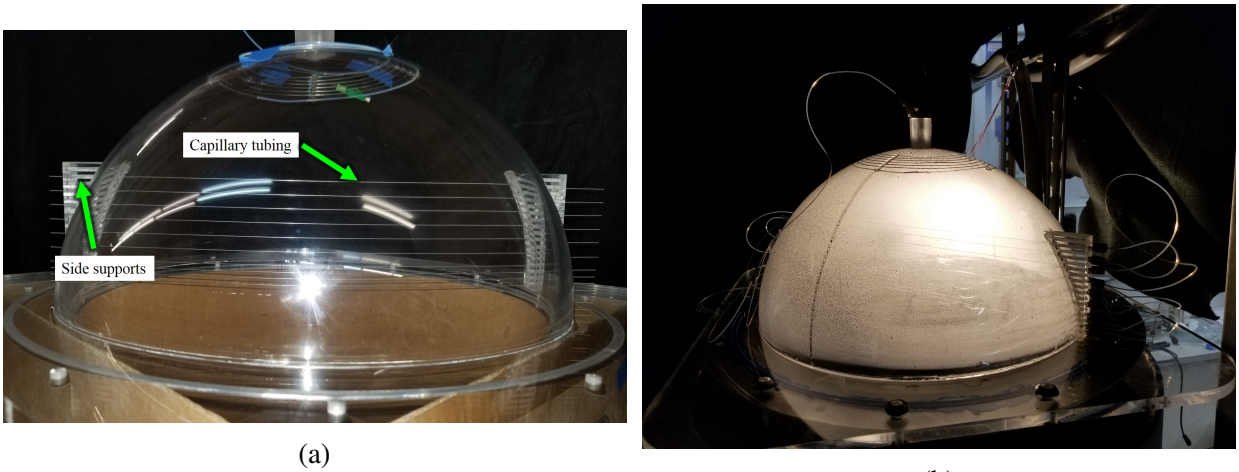

(a) (b)

Figure 8.19: Installation of DTS in fluid of the HTGR upper plenum facility.

The orientation of the DTS plane installed in the dome was determined by considering the dome's future use for PIV and LIF measurements. These laser-camera techniques require both an unobstructed laser path and camera view. On this dome, the DTS are at a 45°angle to either the laser or the camera. This orientation was also the best choice for installing the capillary side supports.

8.2.2 Facility Operation

The upper plenum facility was brought to steady conditions by pumping water through the cooling jacket after the main coolant had convected heat through the main vessel. Steady conditions are defined in this facility as close readings between main inlet and cooling jacket outlet temperatures. The plane-DTS was recorded during the entire startup process and during steady conditions, and the wall DTS was only recorded during steady conditions. Hardware limitations of the ODiSI-B required this procedure to take place. Fiber data was acquired at 100 Hz during steady conditions.

8.2.3 Results and Discussion

The vertical locations of the DTS in the HTGR upper plenum facility were measured after installation, and have been recreated in a computer drawing. Figure 8.20 shows the vertical layout of the fiber DTS segments, while Table 8.5 lists the vertical coordinates of each segment (numbered from highest z-location to lowest). Fiber segments were placed closer together near the floor of the dome in an effort to provide more resolution of the single plume that forms above the center heated pipe.

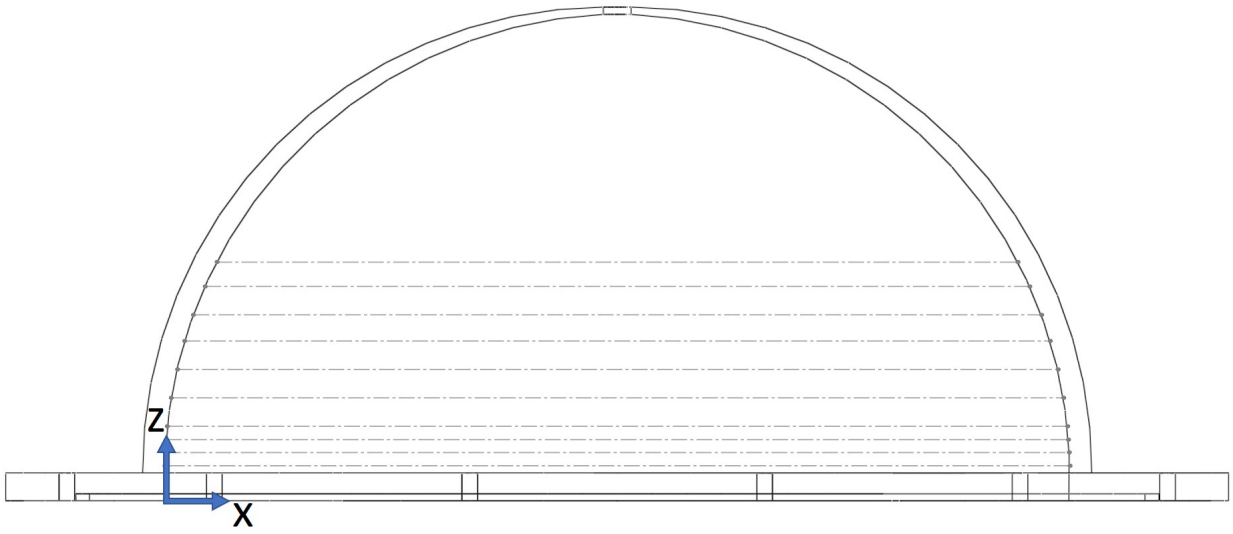

Figure 8.20: Location of DTS segments inside dome of HTGR upper plenum facility.

Table 8.5: Vertical coordinates of each fluid DTS segment in the z-direction.

DTS Segment	*Z-Location* (mm)
1	109
2	98.0
3	85.0
4	73.0
5	60.0
6	47.0
7	34.0
8	28.0
9	22.0
10	16.0

Time-averaged temperature during steady conditions fo the water DTS are shown next in Figure 8.21. Each fiber segment has been plotted as a function of distance across the dome. Since the reference temperature of the water was taken with the Fluke® reference thermometer and probe, the uncertainty of this data is 2.2°C.

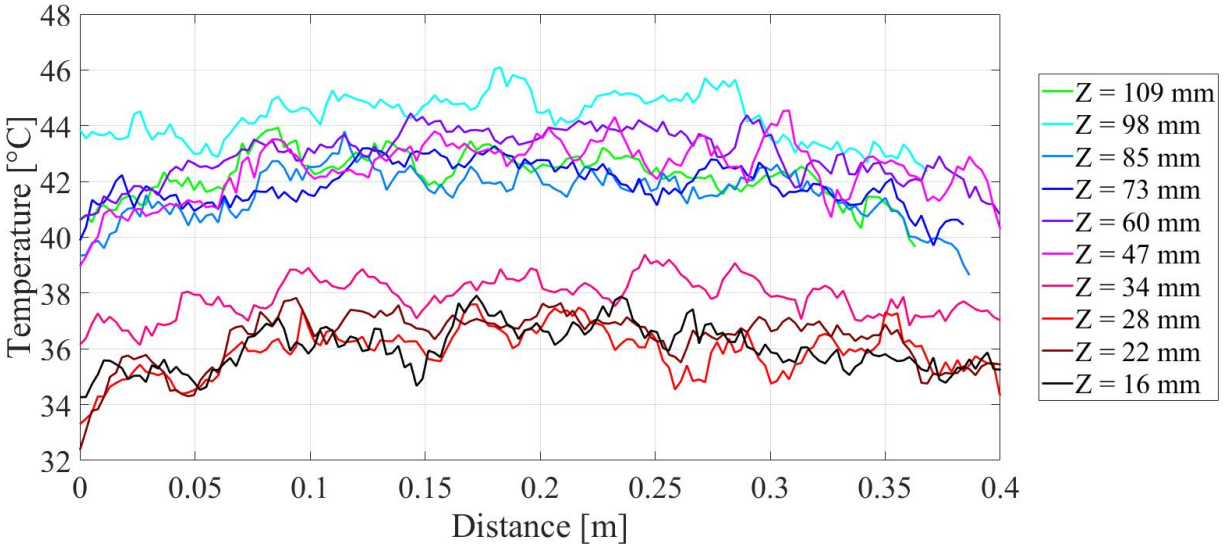

Figure 8.21: Time-averaged temperature recorded by DTS sensor in water.

The goal of these measurements was to resolve the temperature profile of the plume, but this does not seem to be feasible with sheathed DTS. The 304 SS capillaries seem to have spread out the heat evenly and created the mostly flat temperature profiles seen in Fig. 8.21. It is possible that the actual temperature of the water in the dome is uniform in the transverse direction far above the plume, but more variation should be seen in the lower fibers.

Another possible reason for this unexpected uniform temperature profile may be due to the intrusiveness of stringing capillary tubing across the plume. During testing, the plume was visible when viewed from the correct angle, and seemed to be at least partially obstructed by the capillaries. Air bubbles also tended to cling to the capillaries. A photo of air bubbles on the capillaries is shown in Figure. 8.22. Bubbles this small may not obstruct the flow that much, but it is an unintended consequence of installing capillaries above a heat source in water. Although these results do not provide any direct conclusions about system behavior, they do prove that DTS can be installed in a dome geometry in a practical way.

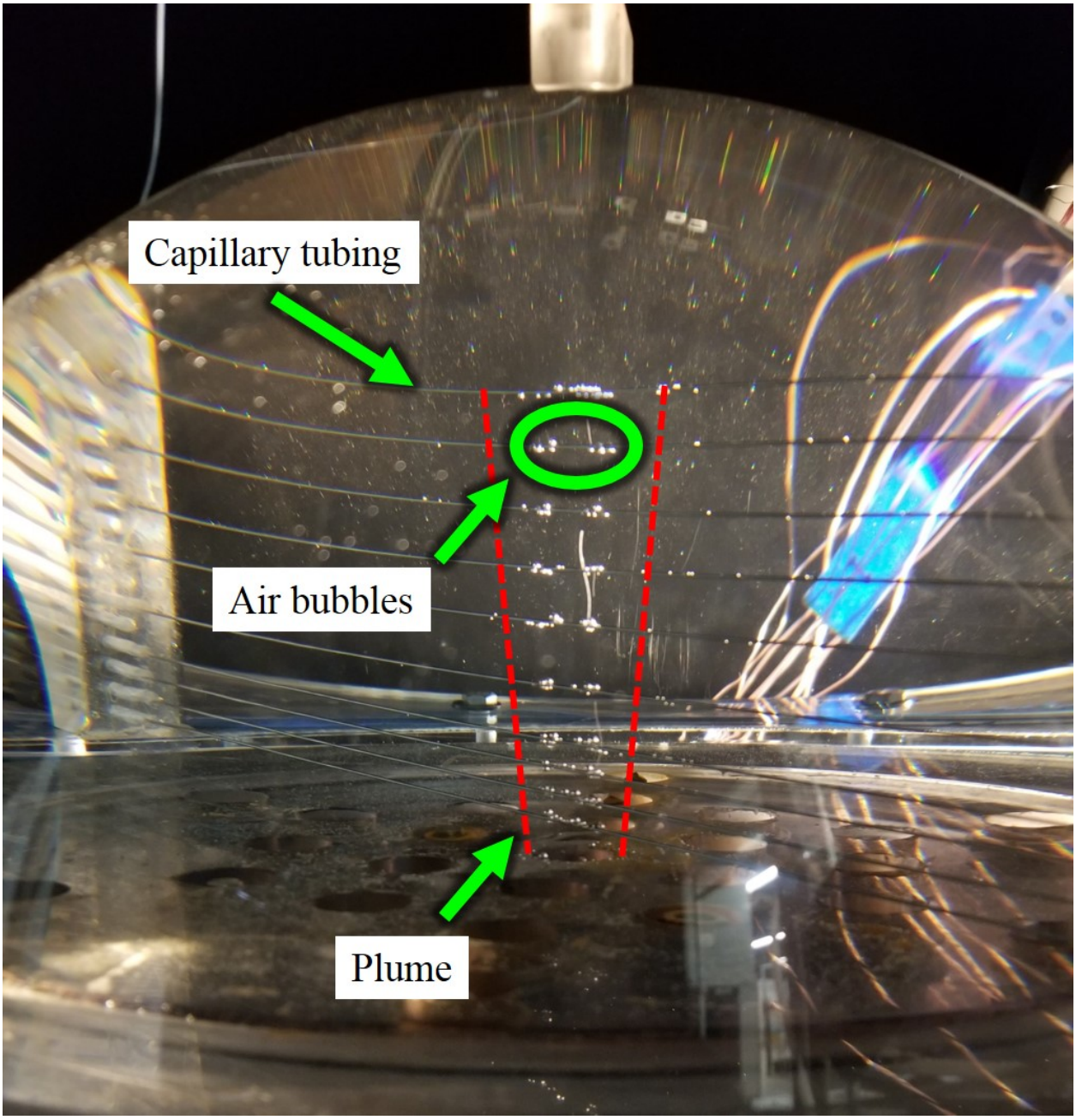

Figure 8.22: Bubbles attached to DTS in water of upper plenum facility.

Time-averaged temperature during steady conditions for the wall DTS in the upper plenum facility are presented in Figure 8.23. The time-average of the entire data set is also shown in the graph (33.3°C). Error bands of one times the uncertainty are also included.

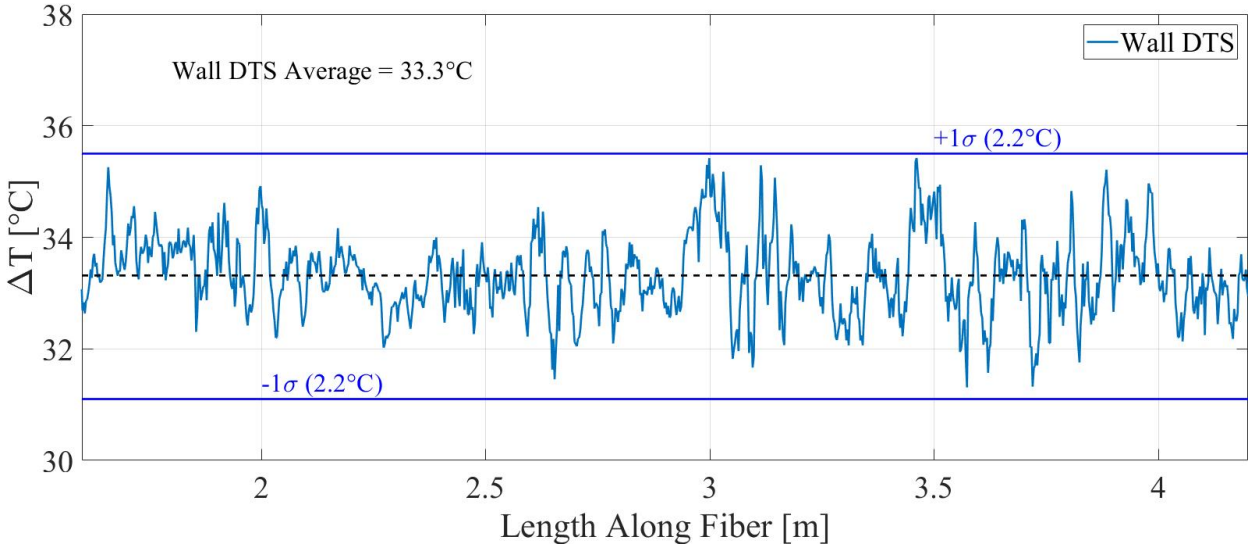

Figure 8.23: Time-averaged temperature recorded by DTS sensor around inner dome vertex.

The wall DTS performed quite well, and the span of 2.2°C in each direction from the time average indicates the steady behavior of this system. The standard deviation of the data shown in Fig. 8.23 is 0.72°C.

The temperatures recorded by DTS in this facility indicate that a warmer layer of water is present near the vertical middle of the dome. This warm middle layer may have formed from a combination of heat loss and stratification, due to no insulation being present on the dome. However, the data is not convincing enough to form a strong conclusion about the behavior of the system while using these measurement methods. Spatial averaging may improve the appearance of these results, but their overall trend will likely stay the same.

9. TWO-PHASE BOILING INVESTIGATIONS

Difficulties in prediction and measurement of two-phase conditions continue to persist in many applications. Conventional wire-based and probe methods and high-resolution camera techniques can both provide the desired measurements, but both have tradeoffs. The former methods tend to be low-resolution, and the latter typically require transparent containment walls. As depicted in Fig. 9.1, boiling two-phase flow can include several flow regimes and each regime change is accompanied by a change in heat transfer. Accurately predicting and measuring the heat transfer capabilities of a system is paramount for any system type. Extrinsic two-phase optic fiber sensors are already commercially available, but none use distributed techniques.

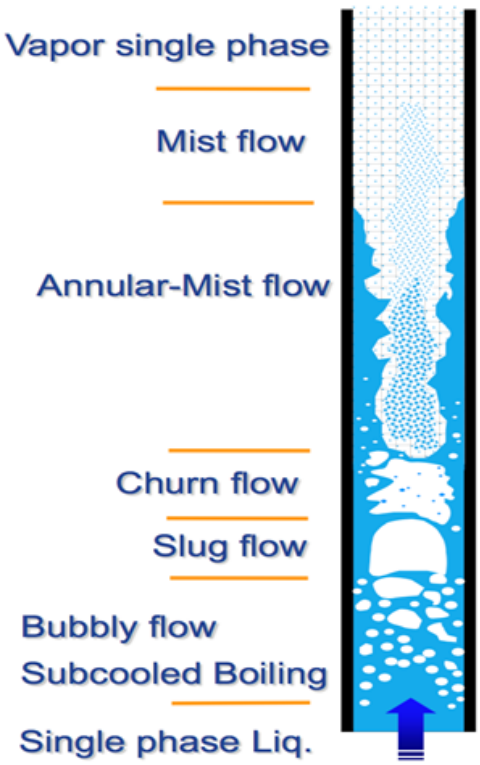

Figure 9.1: Diagram of boiling flow development in vertical channel.[145]

The final objective of this study was to explore the possibility of detecting and possibly measuring other parameters besides temperature and strain. Fourteen steady-state tests were performed with fiber DTS installed in a vertical heated pipe of water. Temperature gradients were detected below the boiling region, especially around the heaters and at the bottom of the intersection between metal and plastic pipes.

9.1 Experimental Facility Description

The final DTS implementation was in the centerline of a vertical heated pipe. Figures 9.2 and 9.3 are a computer drawing and the instrumentation diagram of this apparatus. Table 9.1 lists the characteristics of each thermocouple installed in this experiment. Multiple thermocouples were used alongside the fiber DTS to allow baseline and reference temperature measurement. The spatial variable z represents each thermocouple's distance to the aforementioned surface.

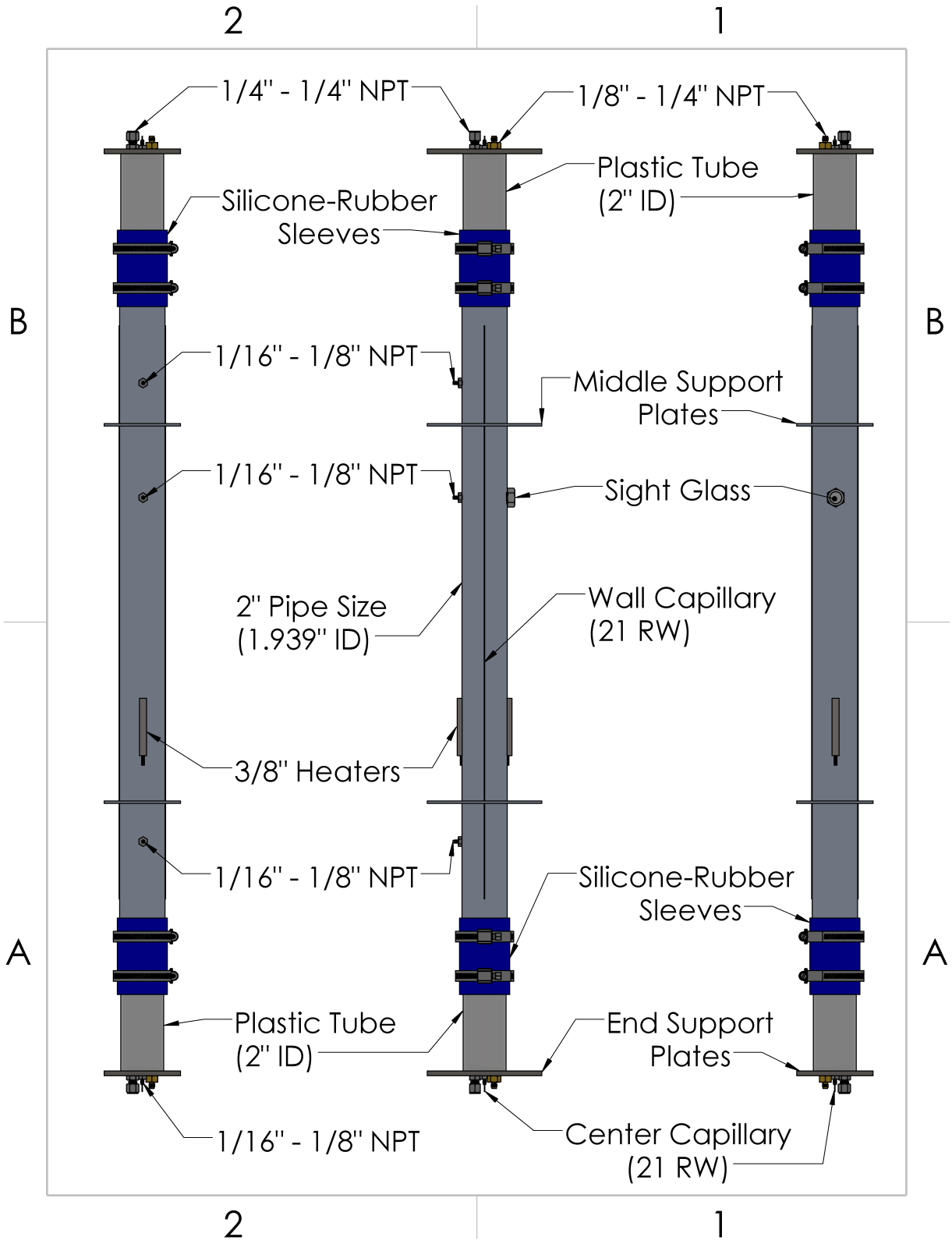

Figure 9.2: Computer drawing of apparatus for the study of DTS response in a heated vertical pipe.

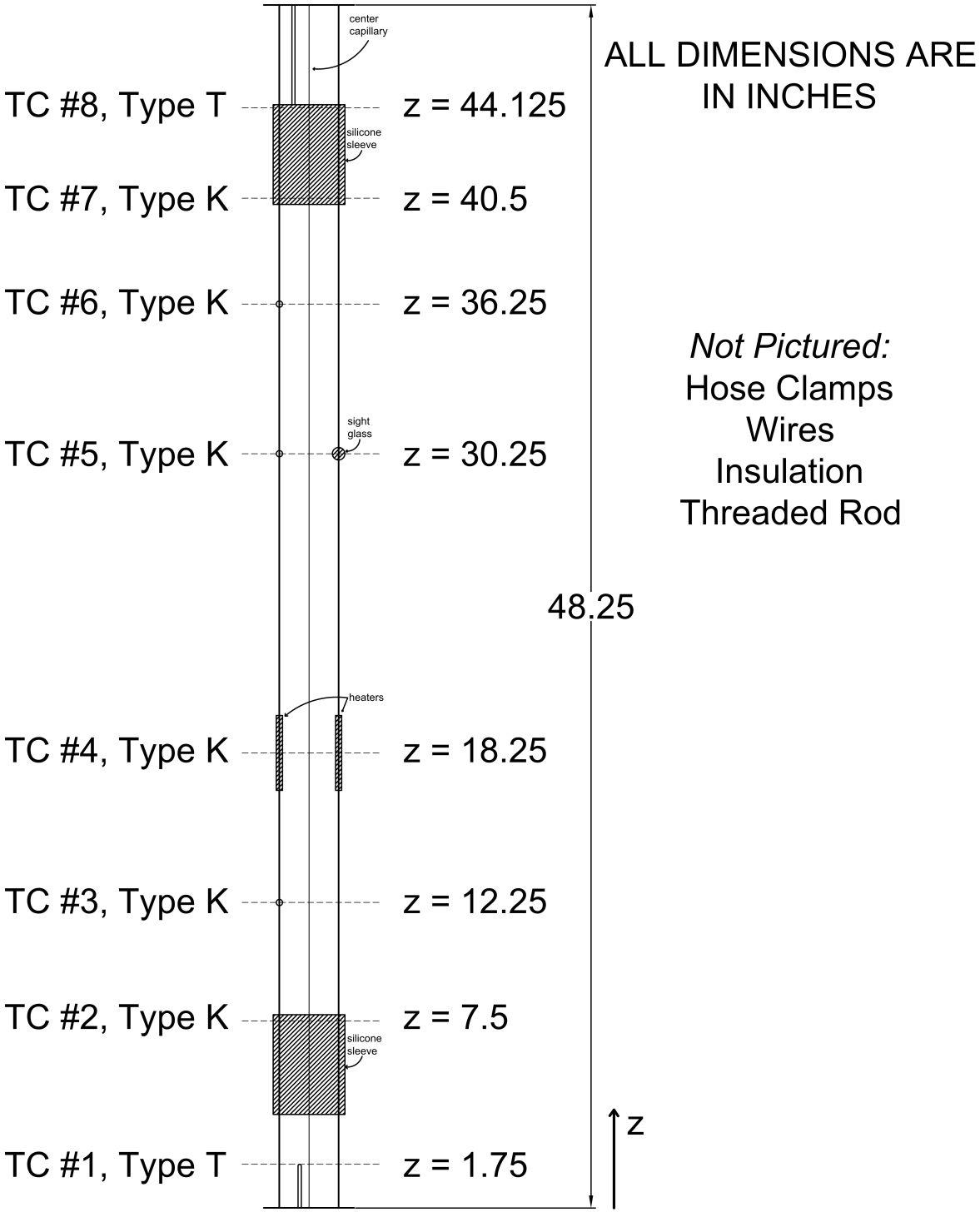

Figure 9.3: Instrumentation diagram of apparatus for the study of DTS response in a heated vertical pipe.

Table 9.1: Characteristics of thermocouples used in heated vertical pipe experiment.

Thermocouple	*Z-Location* [in (cm)]	*Type*	*Probe Dia.* [in (cm)]	*Uncertainty*
TC #1	1.75 (4.45)	T	1/8 (0.32)	$\pm$0.5°C or 0.4%
TC #2	7.5 (19.1)	K	wall mount	$\pm$1.1°C or 0.4%
TC #3	12.25 (31.1)	K	1/16 (0.16)	$\pm$1.1°C or 0.4%
TC #4	18.25 (46.3)	K	1/8 (0.32)	$\pm$1.1°C or 0.4%
TC #5	30.25 (76.8)	K	1/16 (0.16)	$\pm$1.1°C or 0.4%
TC #6	36.25 (92.1)	K	1/16 (0.16)	$\pm$1.1°C or 0.4%
TC #7	40.5 (103)	K	wall mount	$\pm$1.1°C or 0.4%
TC #8	44.125 (112)	T	1/8 (0.32)	$\pm$0.5°C or 0.4%

The experiment apparatus was designed around a 48 inch tall vertical cylindrical column of water, shown during (a) and after (b) assembly in Figure 9.4. Six inch sections of clear polycarbonate plastic allowed visual inspection of the apparatus interior at the top and bottom of the water column. The clear sections were secured on each end of the 2 inch diameter, 36 inch long Sch. 80 aluminum pipe by 4 inch sections of high-temperature coolant hose and secured with hose clamps. Two 400W cartridge heaters (800W total power) were placed in machined grooves and attached by hose clamps to the sides of the aluminum pipe. Three holes for instrumentation ports were drilled and tapped along the aluminum pipe, along with a hole for the sight glass. Space ($\sim$1/8 inch) was allowed between the polycarbonate tube sections and the aluminum pipe to reduce heat conduction between the two materials. Alumina silica wool insulation surrounded the length of aluminum pipe to reduce heat loss.

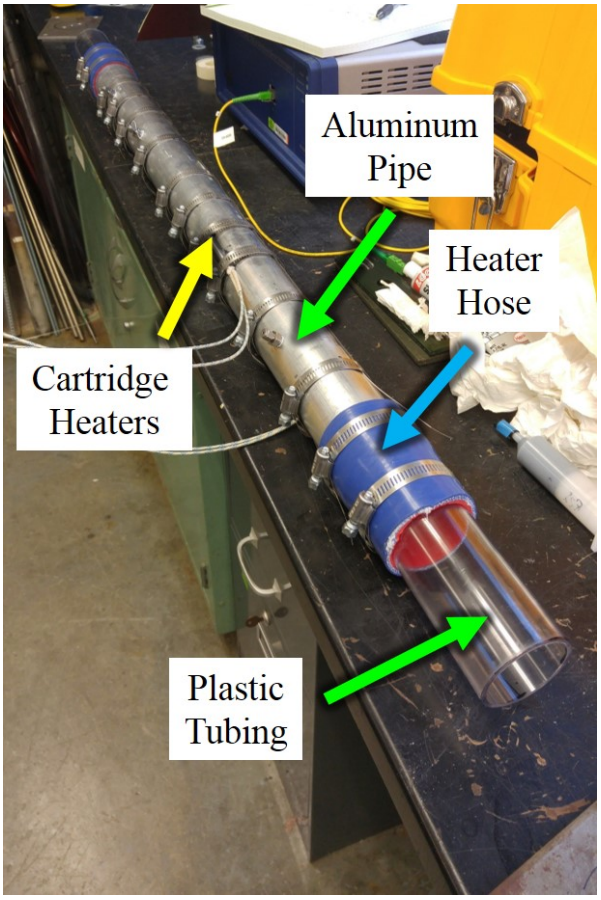

(a)

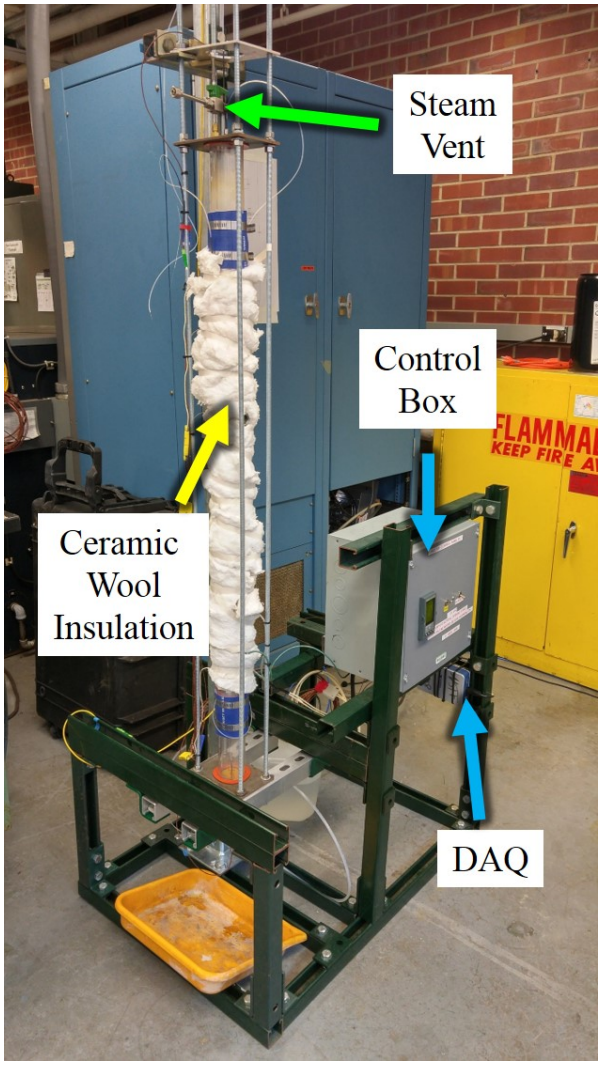

(b)

Figure 9.4: Heated pipe assembly before mounting (a) and completed apparatus with control and data acquisition system (b).

9.2 Fiber DTS Intallation

Two optic fiber DTS configurations were studied, both requiring unique methods of sensor installation:

1. Capillary tubing present - the optic fiber DTS was inside a stainless steel 21 RW tube, which isolated the sensor from the water (sheathed DTS);

2. No capillary present - the DTS was in full contact with the water (exposed DTS).

The sheathed DTS setup included a 155 μm diameter, polyimide coated fiber optic cable within 304 SS 21 RW capillary tube that was tensioned between the bottom and top support plates. At the bottom of the water column, the capillary was bonded inside a 1/16 inch stainless steel sleeve that was then sealed into a pipe fitting. At the top, a 1/16 inch drill bit stop collar was fastened to the capillary and held in place with a small spring, tensioning the capillary. This configuration is necessary to maintain a taught capillary as the liquid column is heated to temperature. Figure 9.15 shows the stop collar and spring configuration.

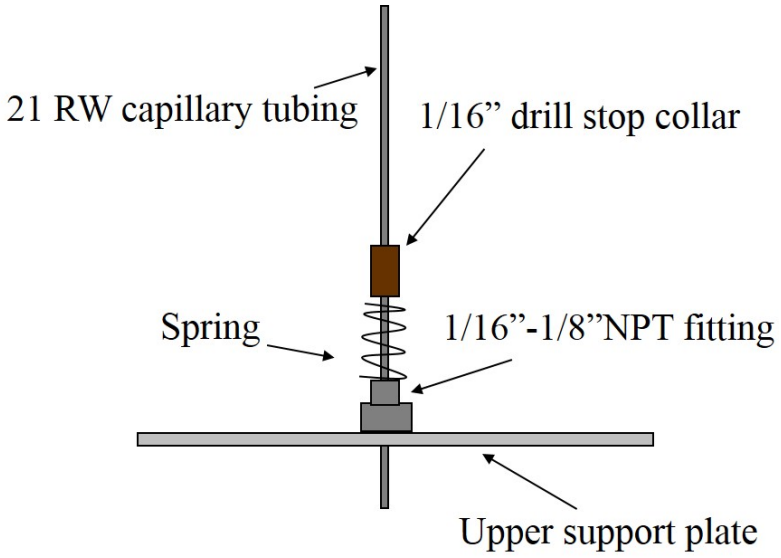

Figure 9.5: Protected (sheathed) DTS setup at top of water column.

The exposed optic fiber itself was bonded with short sections of 21 RW and 18 ga. stainless steel tubing arranged concentrically around the fiber, then sealed into a compression fitting at the bottom of the column. A pulley and weight were configured above the assembly to keep the exposed fiber under a small amount of tension. As with the sheathed configuration, this arrangement maintained spatial positioning of the DTS. Fig. 9.6 is a simple representation of the pulley and

weight installation. After the location of the weight was determined, a short section of 21 RW capillary was bonded to the DTS and the same 1/16 inch drill bit stop was used to hold the weight.

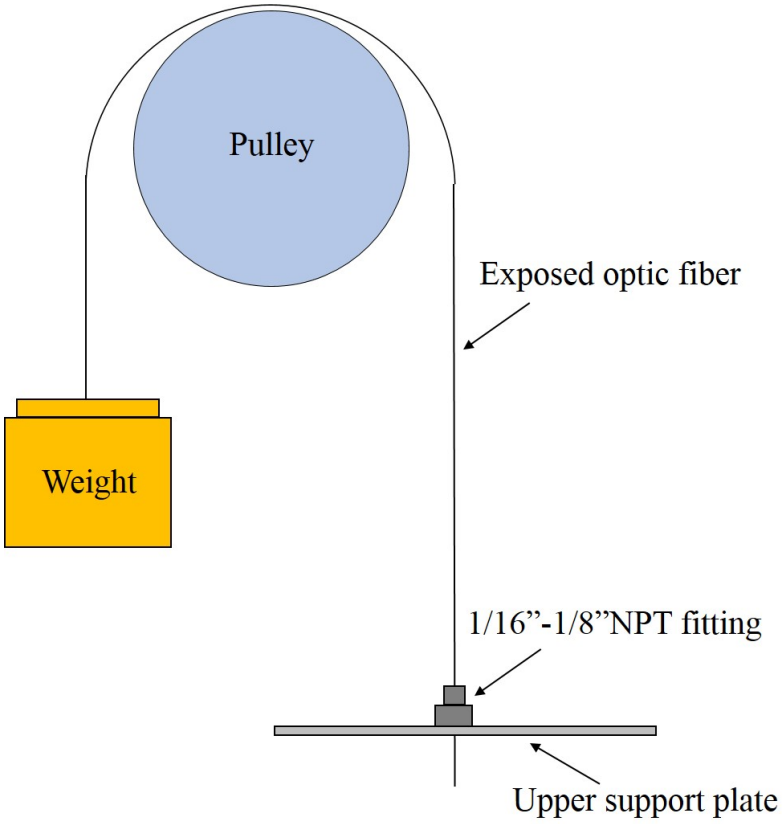

Figure 9.6: Unprotected (exposed) DTS setup at top of water column.

9.3 Facility Operation

The purpose of this study was to evaluate the use of optic fiber DTS in boiling conditions. At the time of this investigaion, two-phase conditions had not been thoroughly investigated with optic fiber DTS. This study investigated two testing conditions:

1. Varying heater power levels (20% - 50%, 5% increments) at saturation to achieve steady conditions;

2. Constant heater power (50%) applied, starting from room temperature and ending after full boiling was achieved.

The general procedure started with recording the date, time, temperature baselines (for both the thermocouples and DTS), and the cold liquid level. After the baselines were measured, thermocouple data recording and heating were begun. Steady-state testing produced 10-minute length optic fiber data sets, while transient testing produced 50-minute sets. Thermocouple recording was stopped after the highest region in the water column had cooled by approximately 20°C. Text logs were created and stored with their respective data sets.

Shakedown tests were performed to record heater surface temperature and verify the apparatus for actual boiling. The apparatus was then tested to find a cold liquid level that permitted safe operation at 50% heater power, which generated high intensity boiling with slug flow. When a safe cold liquid level was determined, the experiment was conducted at consecutively higher heater power levels between 20% and 50%. After these steady-state tests, the heaters were set to 50% power for transient testing.

9.4 Steady-State Testing

Detected temperature is plotted versus column height for heater power level of 20% in Figures 9.7 and 9.8. Both sheathed (9.7) and exposed (9.8) fiber configurations are plotted. The latter showed a slight dependency on heater power level. The column height has been normalized for simpler evaluation and presentation. Noise levels were observed to be 0.1°C. The general profiles of these plots were similar throughout steady-state testing. Additional comparisons for all other power levels can be found in Appendix D.

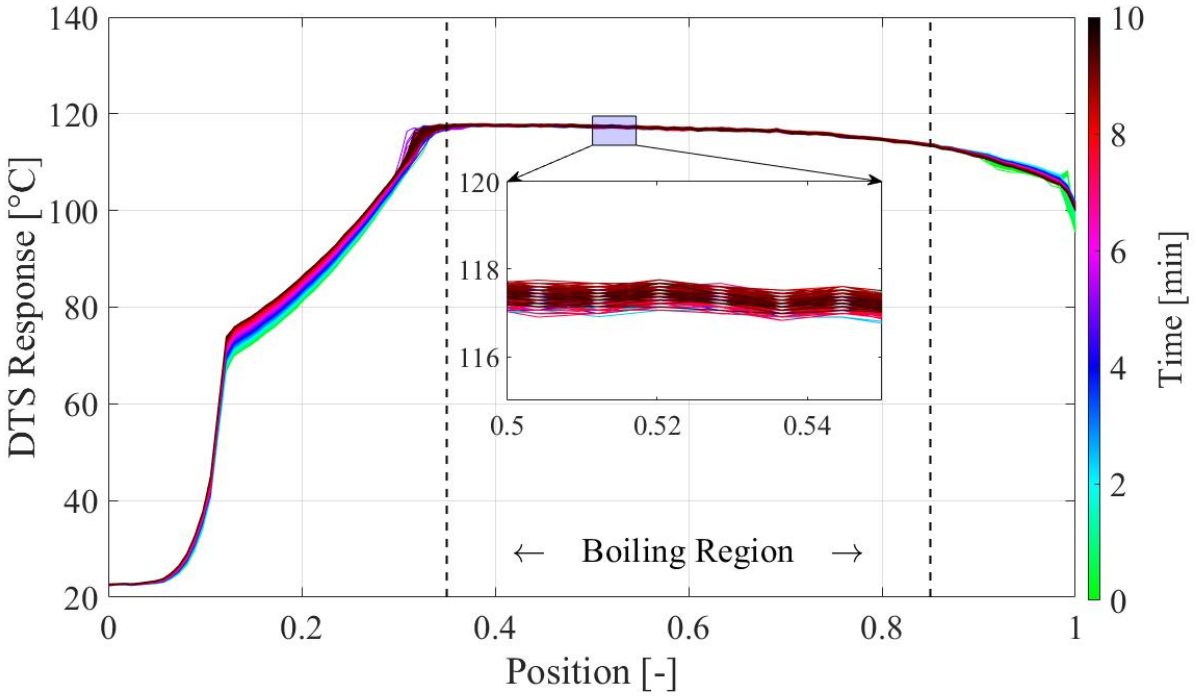

Figure 9.7: Time-averaged temperature recorded by sheathed DTS in two-phase heated vertical pipe.

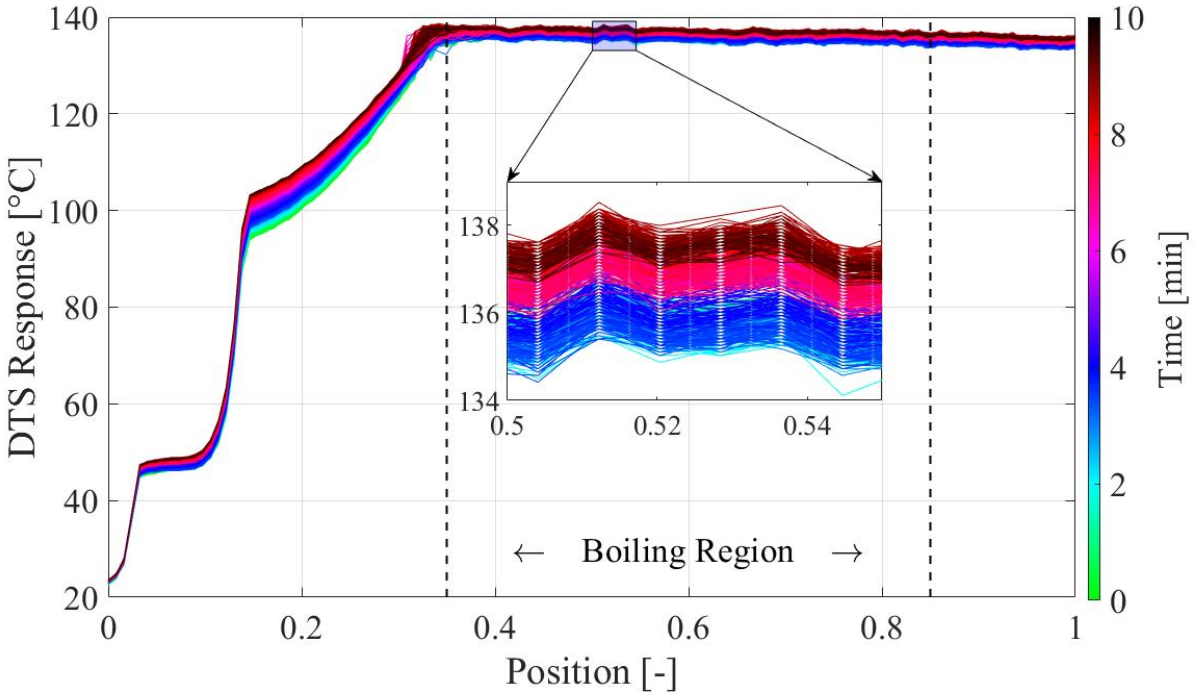

Figure 9.8: Time-averaged temperature recorded by exposed DTS in two-phase heated vertical pipe.

The higher recorded temperature of both DTS configurations in Figs. 9.7 and 9.8 are due to the absence of a correction curve for this data. An even higher response from the exposed DTS further verifies the usefulness of a calibration curve, but this was not the objective of this experiment. Calibrated data is necessary for measurement of absolute temperature, and this experiment was designed to test the feasibility of fiber DTS for boiling detection. The difference in temperature detected between fiber configurations is due to the additional strain imposed by water absorption of the fiber coating. This effect was analyzed in the previous chapter.

The time-averages of select steady-state data is presented next in Figure 9.9. As in Figs. 9.7 and 9.8, the exposed DTS shows a higher response to boiling conditions.

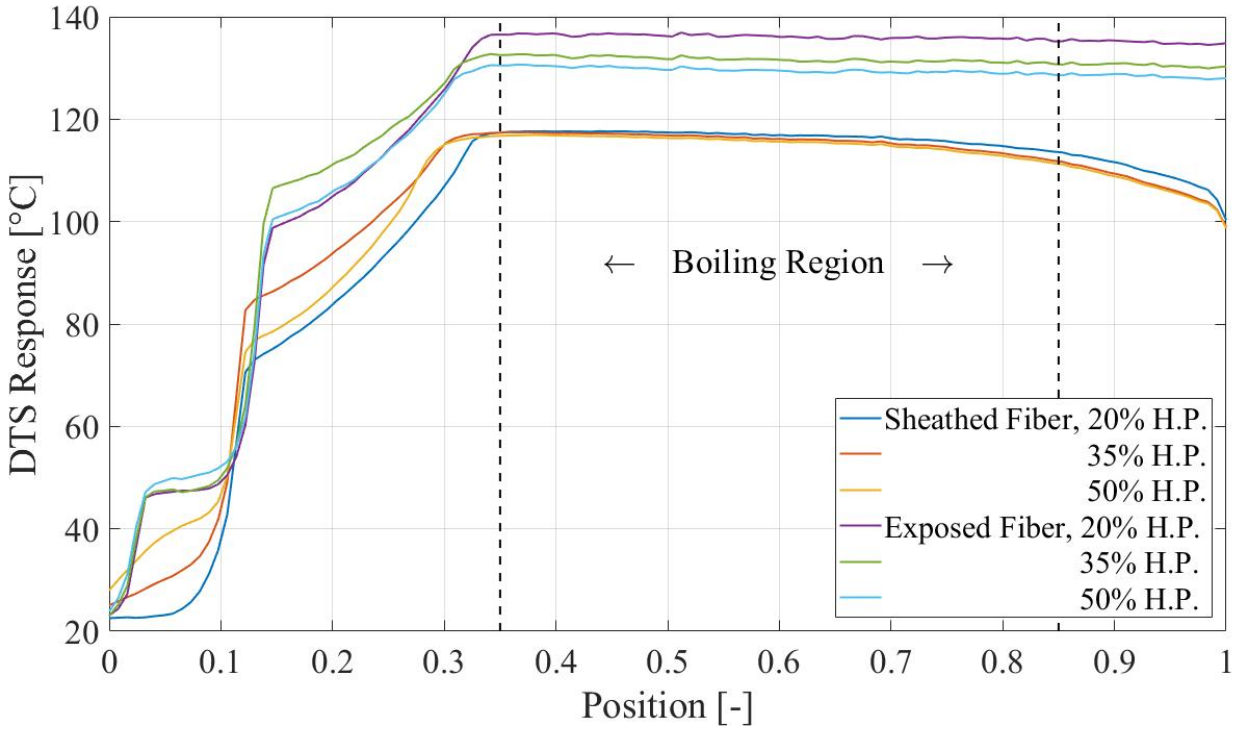

Figure 9.9: Time-averaged temperatures from boiling tests in heated pipe from both DTS configurations.

While the sheathed DTS measurement in the boiling region stayed relatively constant across boiling regimes, the exposed DTS displayed noticeable deviations between boiling regimes. The temperature detected by the exposed DTS in the boiling region decreases as heater power increases. This trend can partly be attributed to the presence of more water vapor in the water column at higher heater powers. A lower amount of water surrounding the exposed DTS would lower the swelling of the fiber coating and therefore lower DTS response.

The steady-state data was also space-averaged in the boiling region ($0.35 < Z < 0.85$) for all values of heater power. Figure 9.10 is a plot of time and space-averaged DTS response in the boiling region for both DTS configurations.

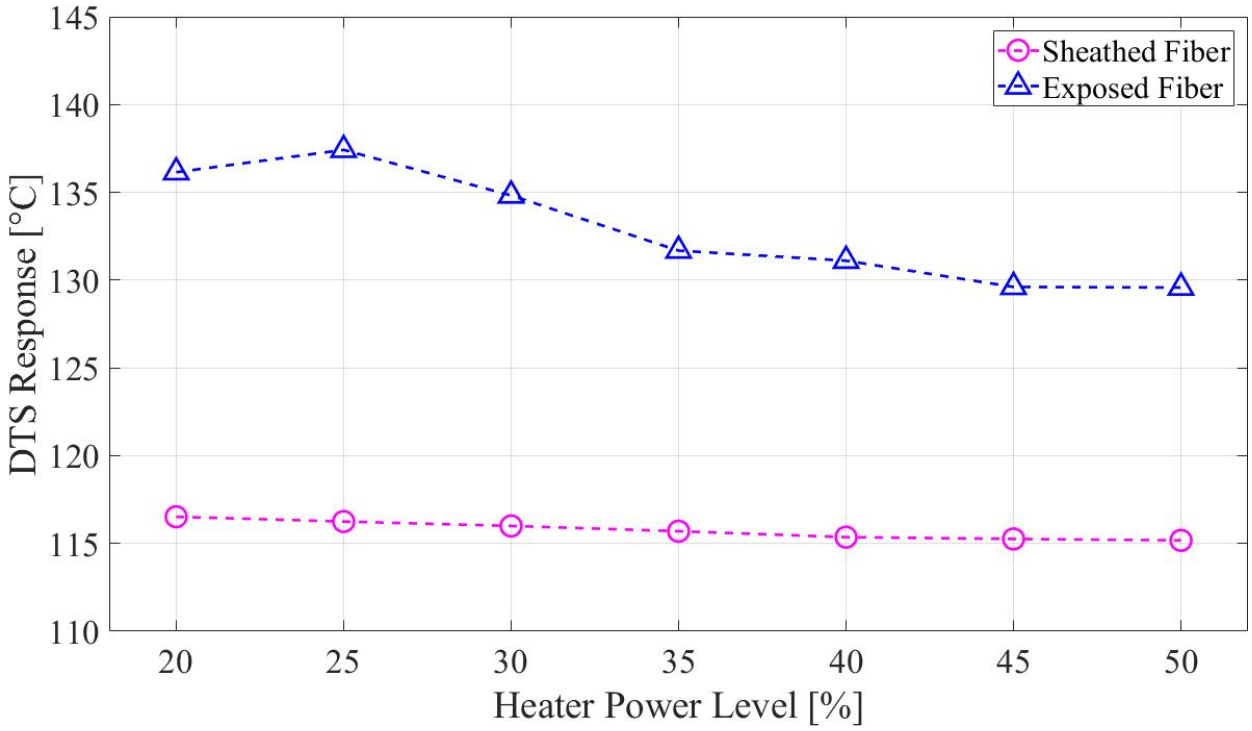

Figure 9.10: Time and spatial averaged temperatures in the boiling region for both DTS configurations.

Minimal differences in sheathed DTS response across boiling regimes are further confirmed by this plot. The complete trend of average boiling temperature detected by the exposed DTS suggests that this analysis could indicate the boiling regime present, as long as the region where boiling occurs is known.

The observed boiling regimes and the maximum fluctuations from the time-averaged response are listed in Table 9.2 as a function of heater power. The boiling regime observations were made with through the transparent section of polycarbonate tubing at the top of the water column. These fluctuations were found by comparing instantaneous data with time-averaged data, and then finding the maximum along the fiber inside the boiling region.

Table 9.2: Absolute maximum fluctuations (in °C) of each steady-state test.

H.P.[%]	*Boiling Regime*	*Protected Fiber*	*Unprotected Fiber*
20	Bubbly	6.85	7.64
25	Bubbly, transition to cap-bubbly	2.70	5.87
30	Cap-bubbly	4.52	4.58
35	Cap-bubbly, transition to slug	3.45	6.10
40	Transition to slug	7.91	6.20
45	Transition to slug	4.19	6.11
50	Slug	5.91	4.76

Figure 9.11 is a graphical representation of the data in Table 9.2. Neither configuration of DTS shows a dependence on heater power level. The values of fluctuations are large enough to suggest actual physical phenomena, but it is not clear why the system displayed this behavior. It is clear, however, that analyzing the data for these fluctuations is not sufficient to make any conclusions about system behavior, especially across multiple boiling regimes.

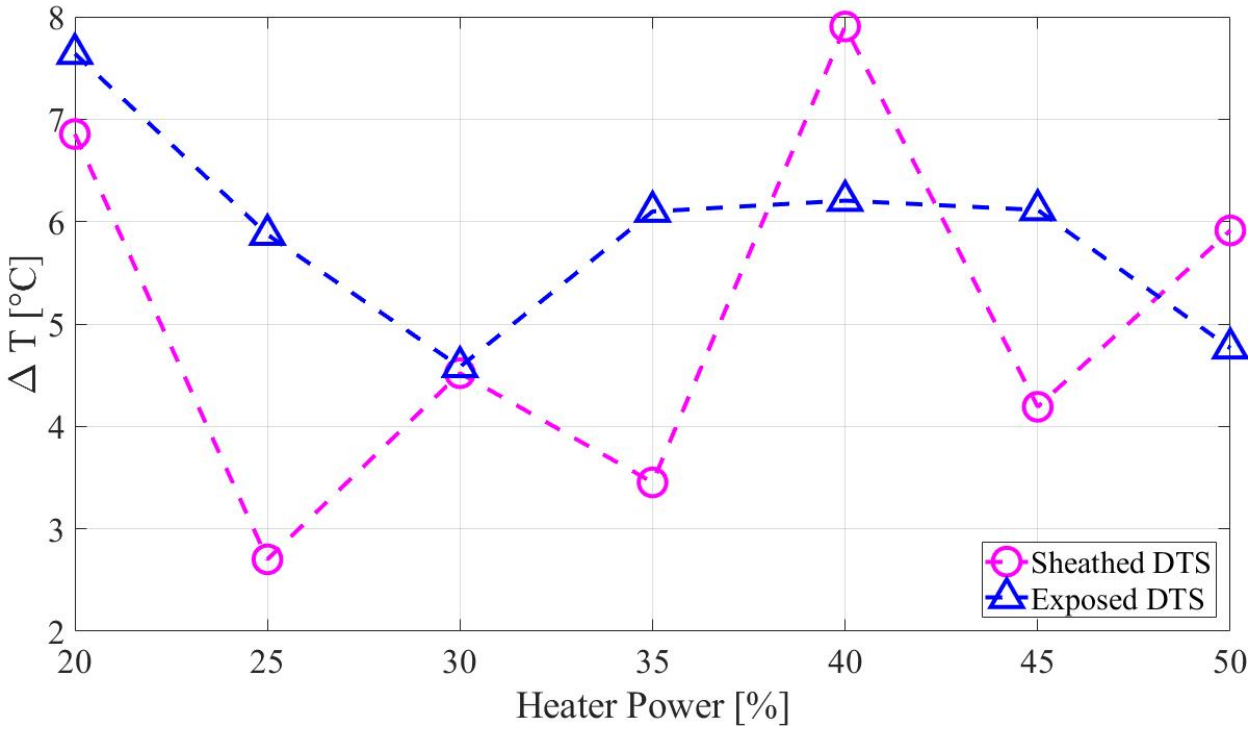

Figure 9.11: Maximum fluctuations from the mean detected temperature in the boiling region for both DTS configurations in steady boiling conditions.

The results of the previous comparisons warranted further analysis of space-averaged data from the steady-state testing performed. Figure 9.12 shows the space-averaged response (a) and average fluctuation (b) detected in the boiling region plotted against time. The spatial average was found by averaging the recorded temperature in the boiling region ($0.35 < Z < 0.85$) for each acquisition in time. The fluctuations were first found by comparing each data point in the boiling region to the spatial average, then averaging those differences.

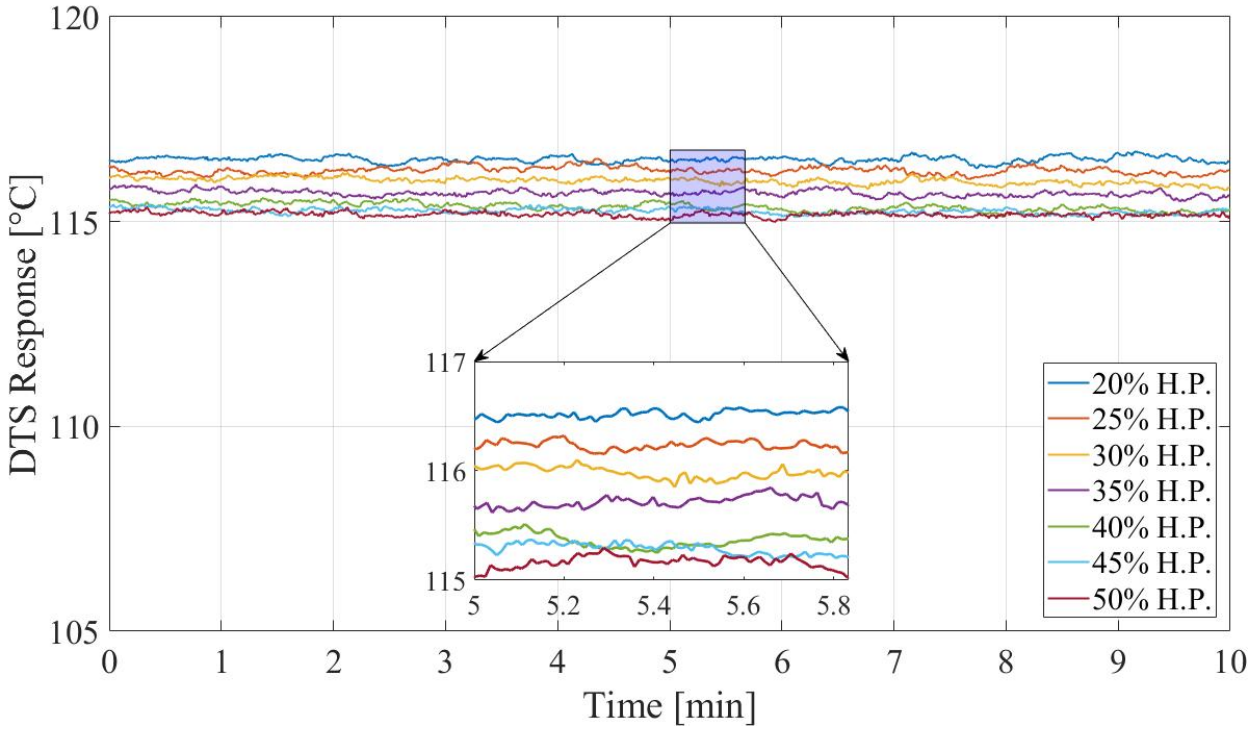

(a)

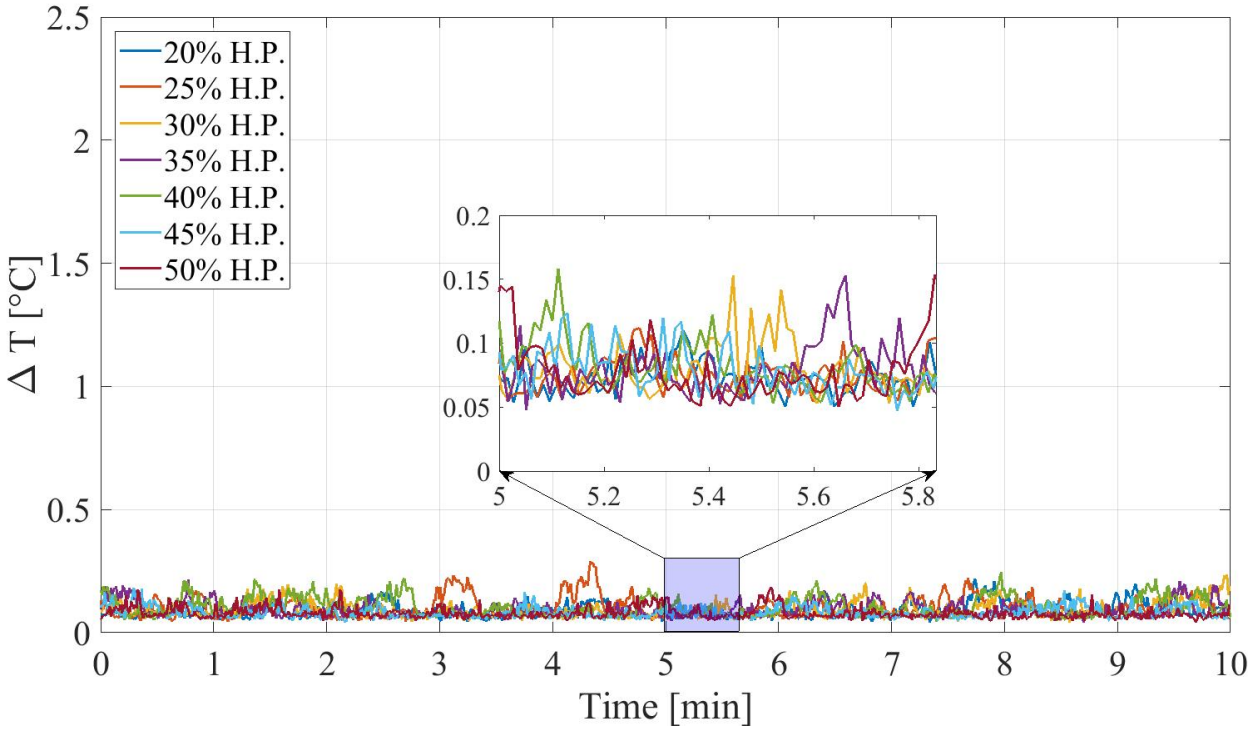

(b)

Figure 9.12: Space-averaged recorded boiling temperatures (a) and average spatial fluctuations (b) during steady-state testing with sheathed DTS.

These figures verify the stable response of sheathed DTS, even in chaotic boiling conditions. The inverse relationship between detected temperature and heater power level indicated in Fig. 9.12(a) suggest that the sheathed DTS also decrease in response to higher levels of boiling, but this result is within the uncertainty for sheathed DTS developed in Chapter 7 (2.2°C). The fluctuations in the boiling region are even lower, close to the noise levels observed.

Unlike the sheathed DTS, the space-averaged boiling temperature and fluctuations of the exposed DTS are not stable and do not have any discernible trend (see Figure 9.13). Averaging exposed DTS data in space and evaluating it in time seems to prevent any quantifiable trends from being observed. A slight dependence on heater power level is seen in Fig. 9.13(a), but the spread of the data is too wide to clearly indicate a trend.

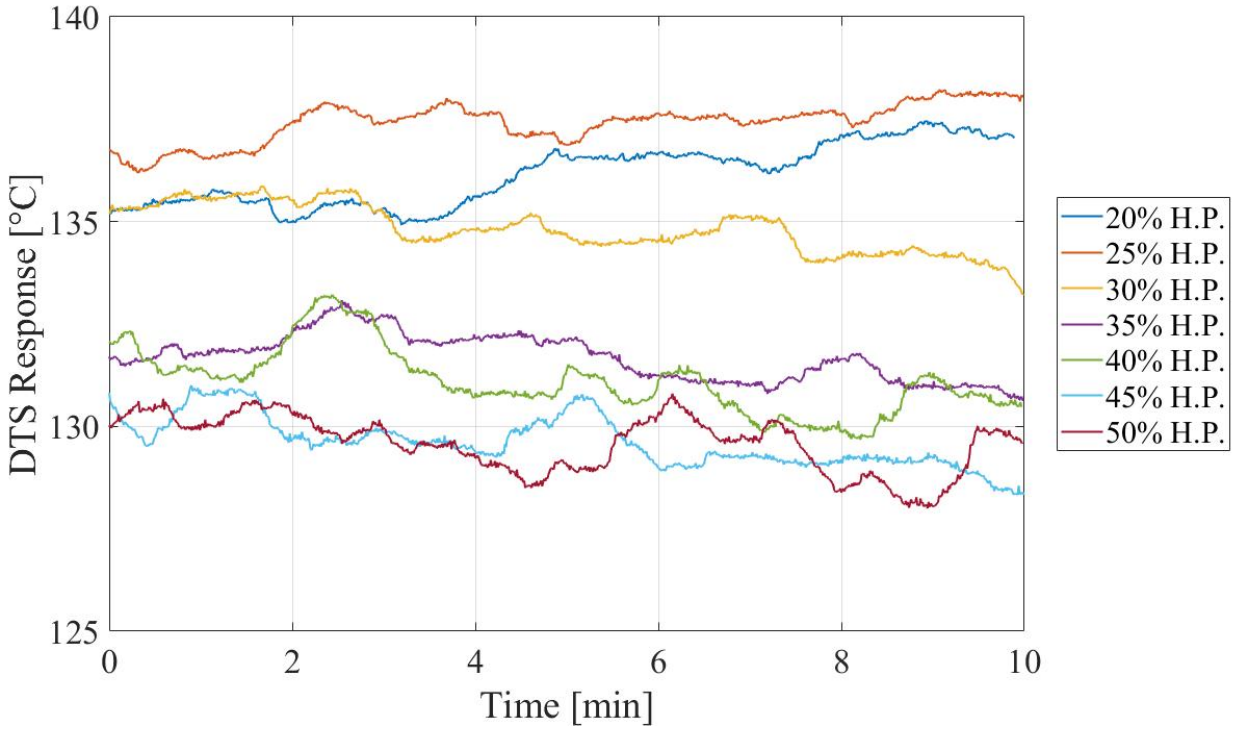

(a)

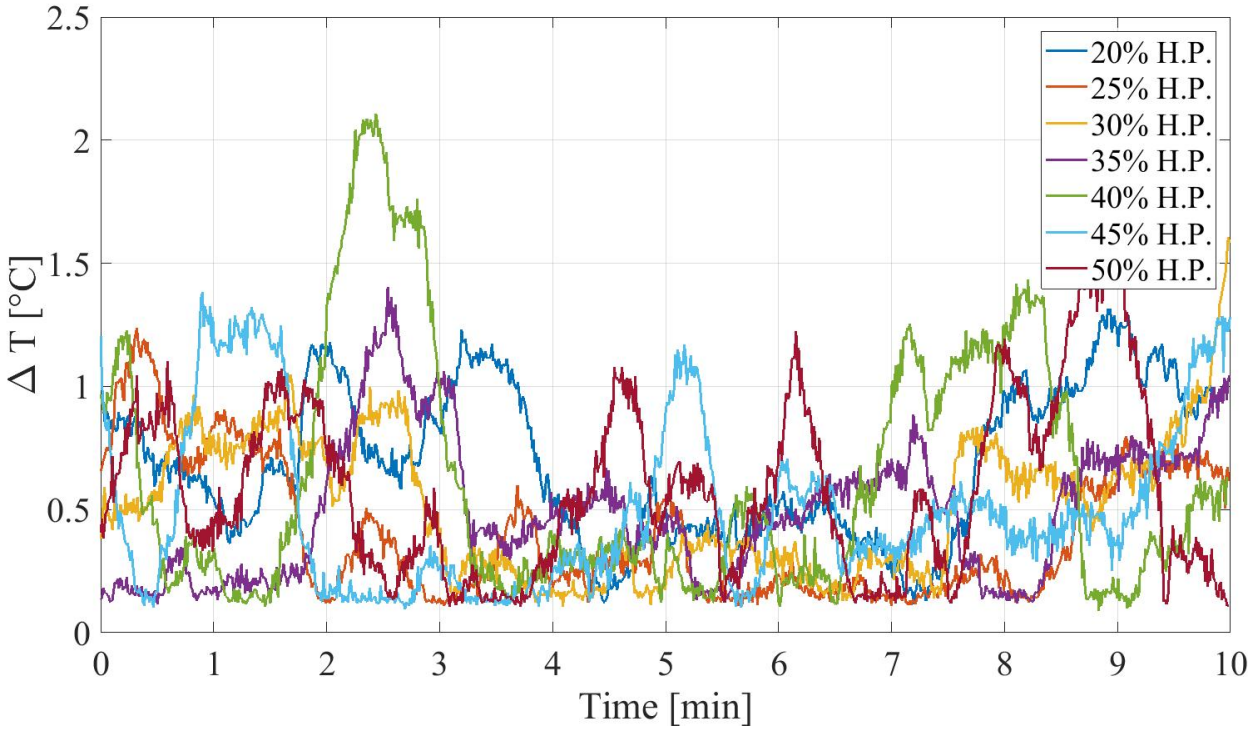

(b)

Figure 9.13: Space-averaged recorded boiling temperatures (a) and average spatial fluctuations (b) during steady-state testing with exposed DTS.

A comparison was then formulated to identify the average spatial variation in temperature measured by the protected and unprotected fibers. The average temperature change from one spatial location to its adjacent point in time-averaged data was calculated. Equation 9.1 summarizes this method, which was applied to the regions labeled in Figure 9.14. These regions were identified as having the most comparative results after applying Eqn. 9.1.

$$\Delta T_{avg} = \frac{1}{N} \sum_{i=1}^{N} (\overline{T_{i+1}} - \overline{T_i}) \tag{9.1}$$

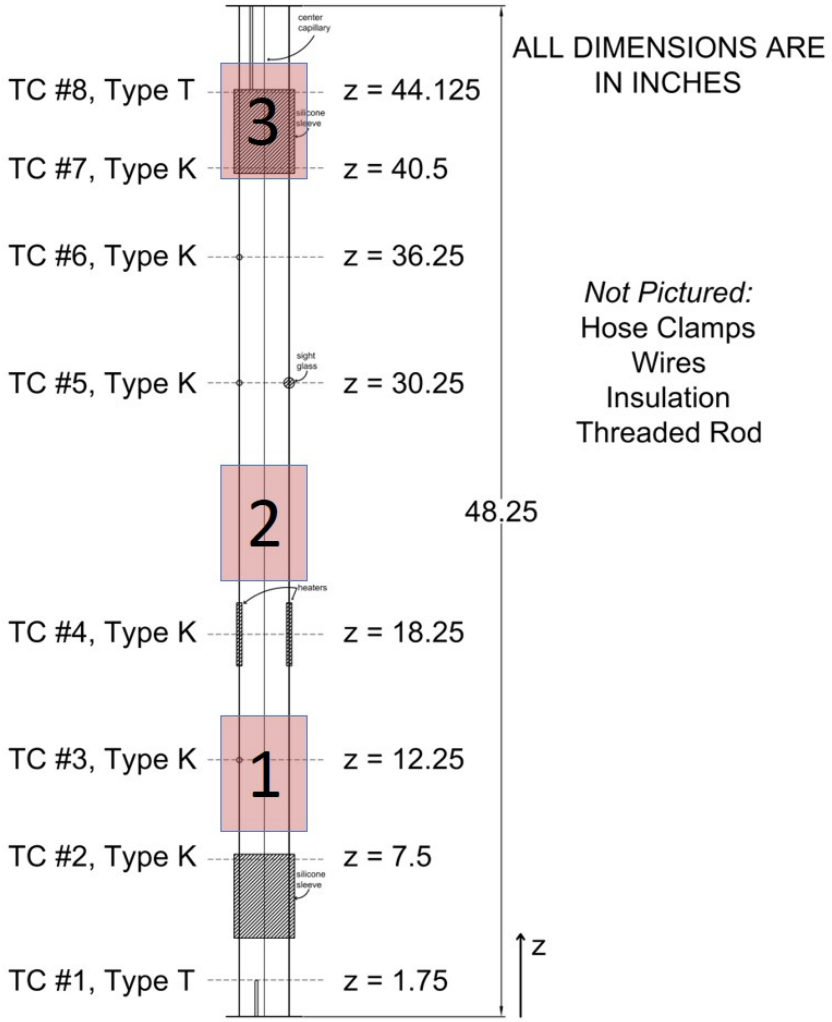

Figure 9.14: Labeled regions of interest for evaluation with Equation 9.1

The results (in absolute value form) are plotted as a function of heater power (i.e. boiling intensity) in Figure 9.15. Table 9.3 lists each region and corresponding plot and description.

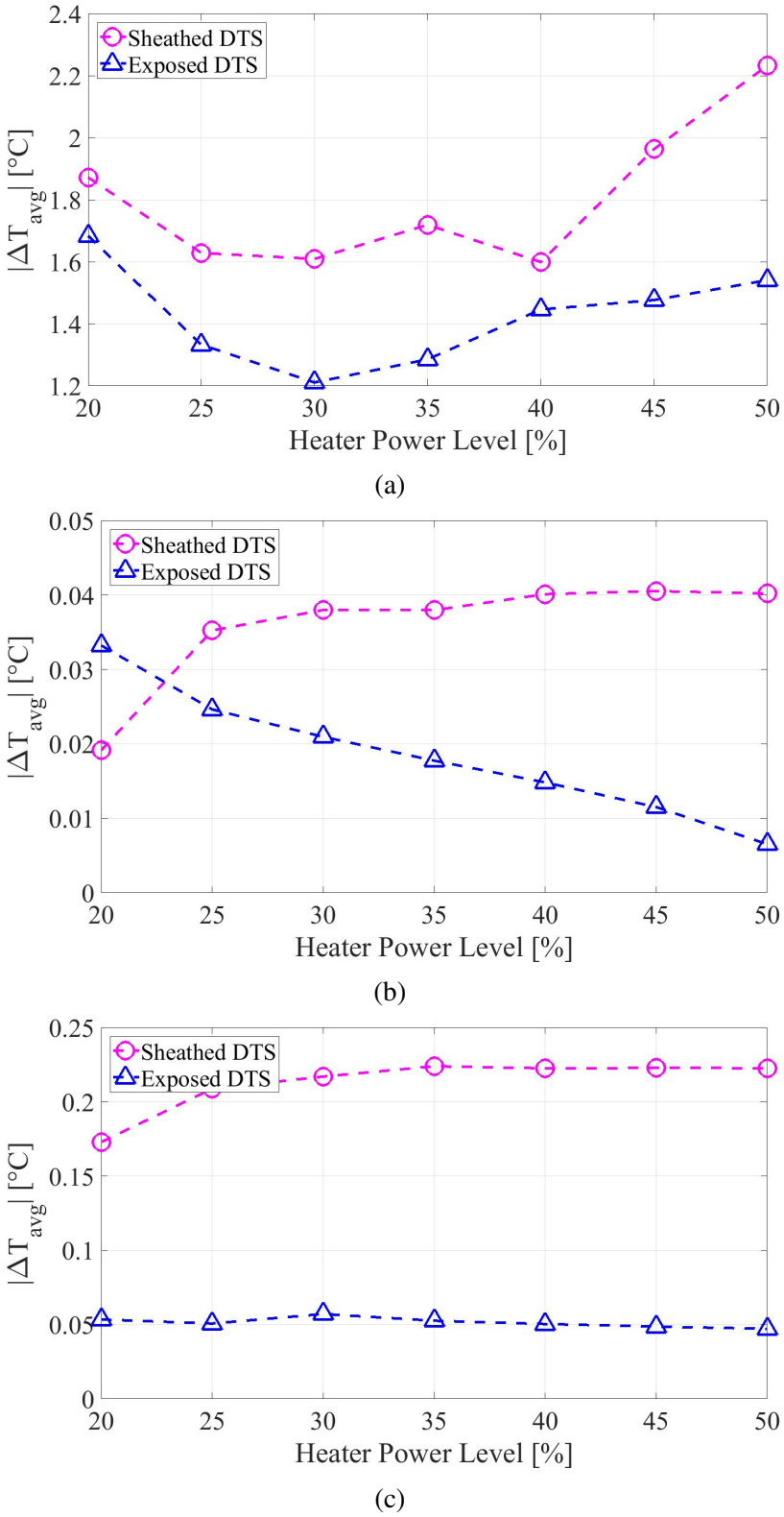

Figure 9.15: Average of differences along regions of time-averaged steady-state data. The analysis of region 1 is plotted in (a), region 2 is plotted in (b), and region 3 is plotted in (c).

Table 9.3: Selected sections along time-averaged data selected for boiling intensity analysis.

Region	*Figure*	*Normalized Range (-)*	*Description*
1	9.15(a)	$0.20 < Z < 0.30$	Immediately below heaters
2	9.15(b)	$0.41 < Z < 0.51$	Above heaters
3	9.15(c)	$0.75 < Z < 0.85$	Top of boiling region

Figure 9.15(b) suggests that the sheathed DTS is capable of indicating boiling intensity to a certain point, but the exposed DTS seems to have a continuous, discernible trend. However, the values along the vertical axis in 9.15(b) indicate that this comparison does not lead to any strong conclusions about the data presented.

9.5 Transient Testing

The purpose of transient testing was to create the most ideal conditions possible to capture boiling with the installed optic fiber DTS. Figures 9.16 and 9.17 show the response of the sheathed and exposed DTS during each transient test, which began from room temperature and lasted 50 minutes. Once the pipe was filled to a safe level, the heaters were turned to 50%, and the system was allowed to reach steady boiling conditions before being shut down. The time is indicated by color, and the time scales are indicated on the right of each figure.

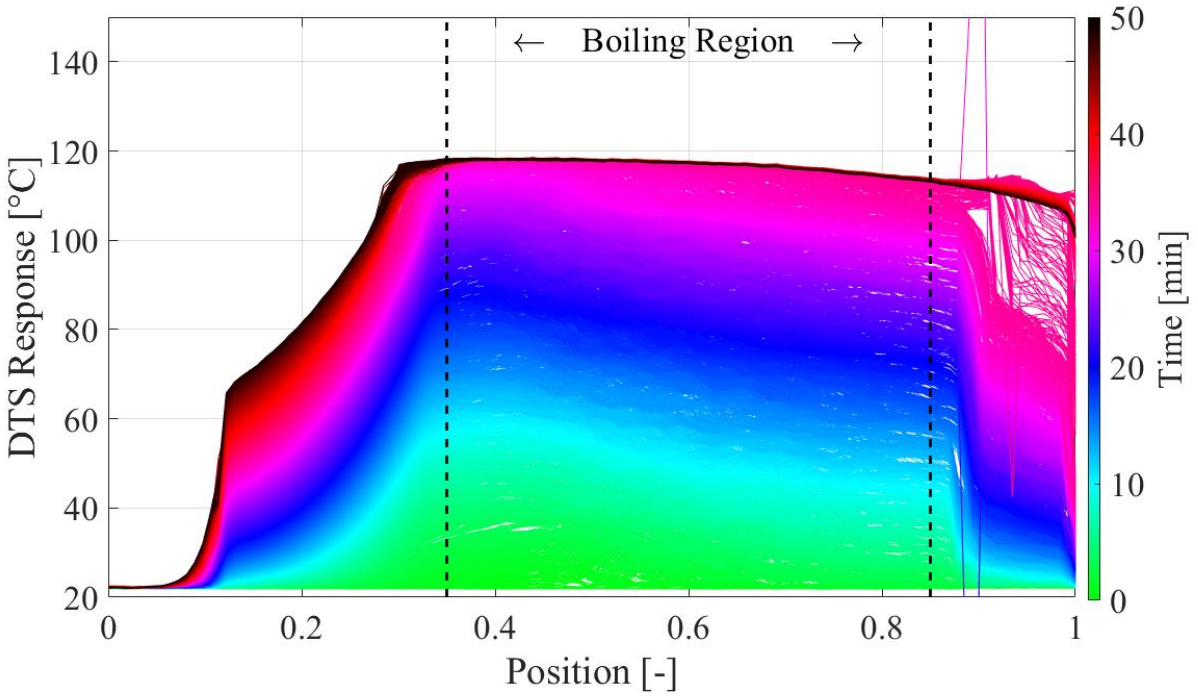

Figure 9.16: Temperature recorded by sheathed DTS during transient testing in two-phase heated vertical pipe.

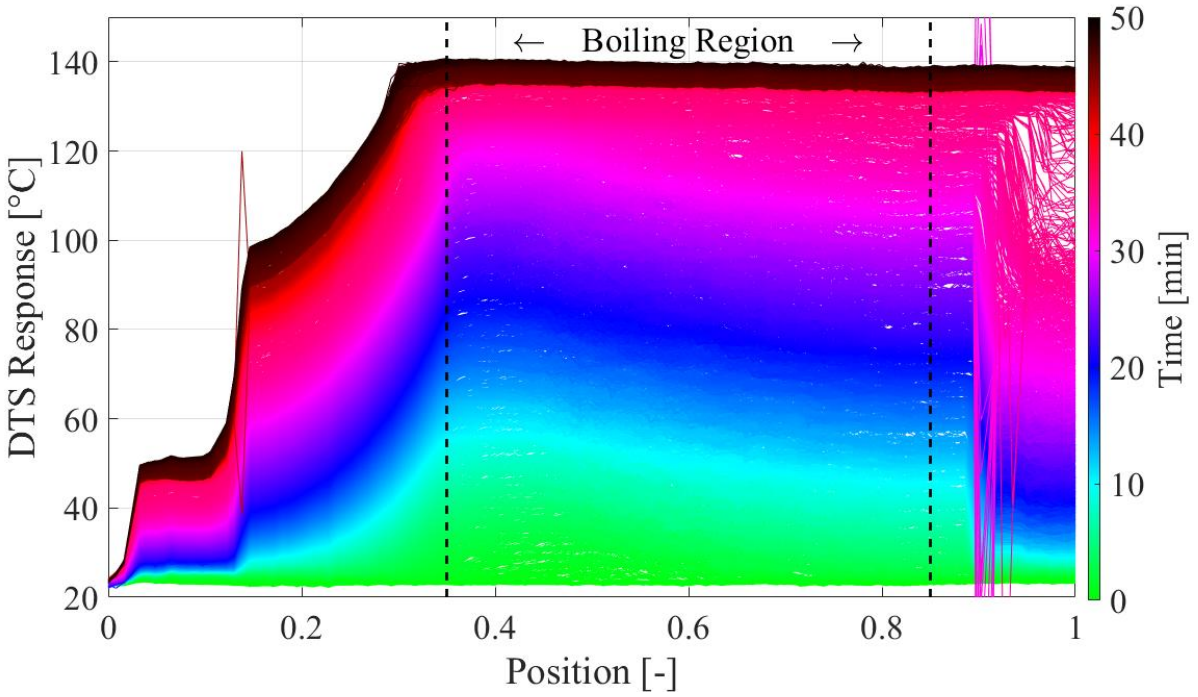

Figure 9.17: Temperature recorded by exposed DTS during transient testing in two-phase heated vertical pipe.

Higher temperatures were detected by both DTS in transient conditions, similar to the steady-state boiling analysis. Both DTS configurations allowed for a vague liquid level measurement, indicated by a sharp gradient in temperature near the right side of the plots. The sharp gradient here shifts to the right as it should, indicating the rising water level due to thermal expansion of the water. This concept was applied to liquid sodium level measurement by Gerardi et al [75] was described in Chapter 4.

The next figure, Figure 9.18, shows the difference in detected temperature during transient testing between sheathed and exposed DTS. Select points in time between 10 and 45 minutes are plotted in order to reveal any areas that may display trends. Discernible trends at Z-locations of $Z = 0.05$ and $Z = 0.16$ seem to be present, and are marked with dashed lines and labels.

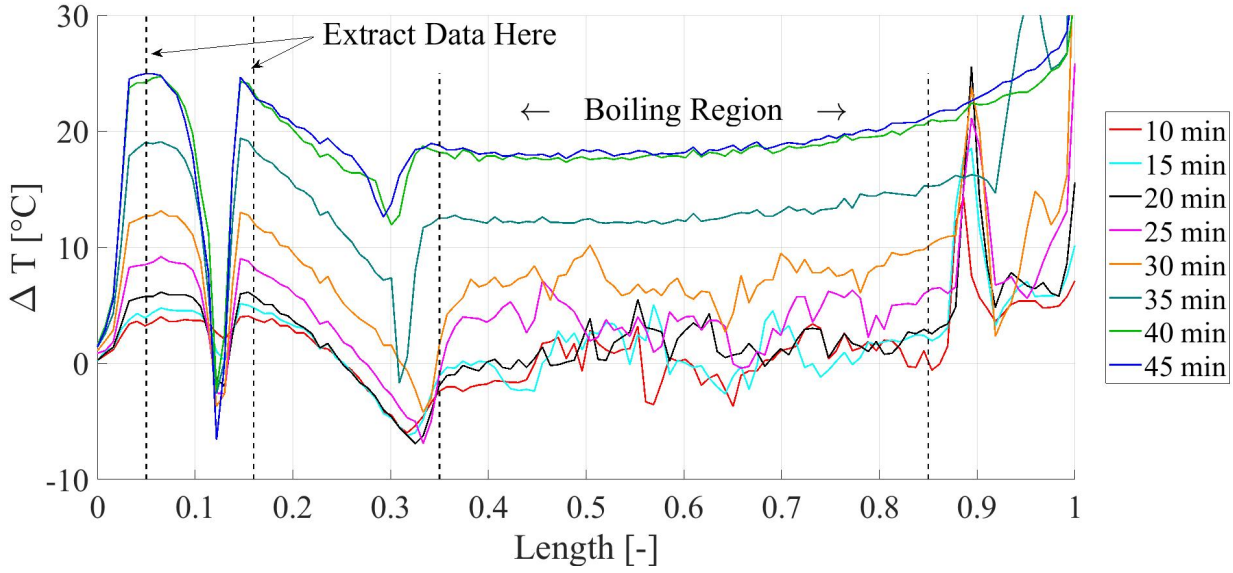

Figure 9.18: Difference in recorded temperature between DTS configurations at corresponding times during transient tests.

Data was extracted along the lines indicated by arrows and labels in Fig. 9.18 and formed into a correction curve. This curve is presented in Figure 9.19. It serves as a comparison between sheathed and exposed DTS, both immersed in water and brought to boiling conditions.

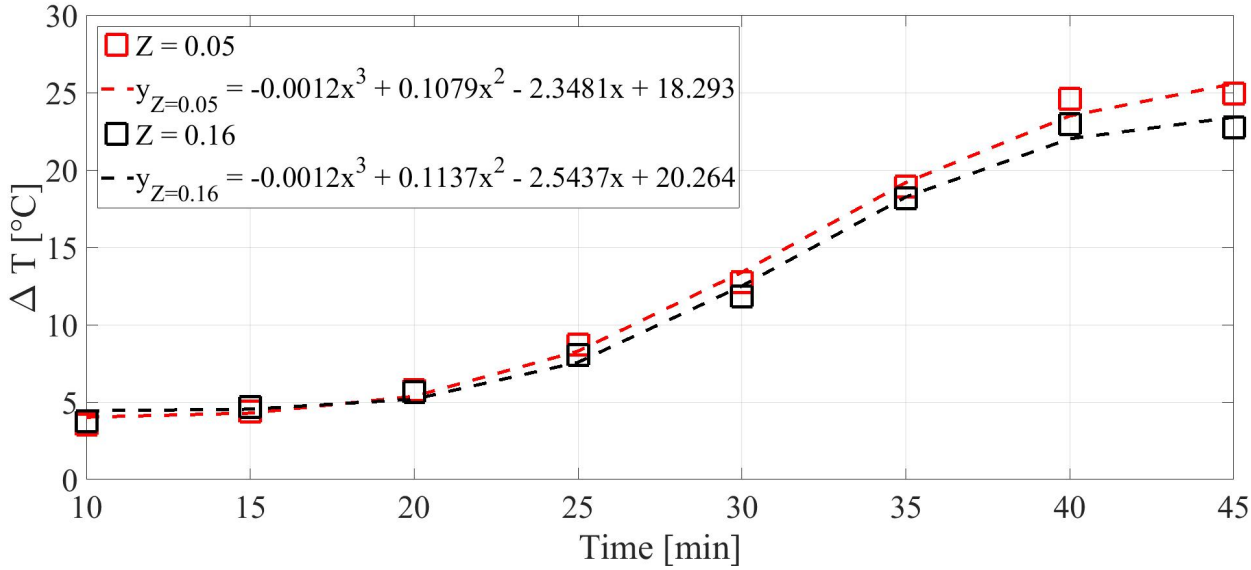

Figure 9.19: Curve fit for data extracted from Fig. 9.18.

The major change causing the trend in Fig. 9.19 is from sheathed to exposed DTS. The shape of this curve is similar to the absorption curve of water vapor into polyimide [141], but Fig. 9.19 should not be interpreted as such. This figure merely fits a curve to the difference in detected temperature between polyimide-coated DTS in air and water. In actuality, this curve is characterizing the difference between water vapor and liquid water effects on polyimide-coated DTS.

The average difference analysis performed on the steady-state data with Eqn. 9.1 was repeated on the transient data and is presented in Figure 9.20. The same vertical regions listed in Table 9.3 were used for these plots.

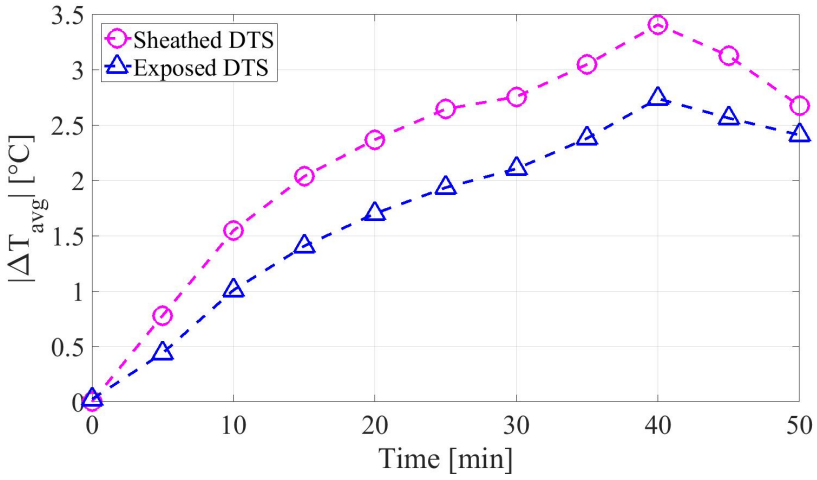

(a)

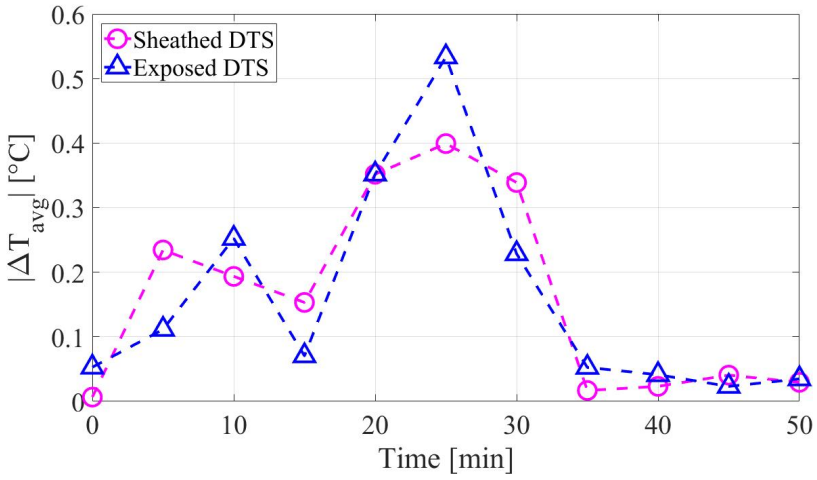

(b)

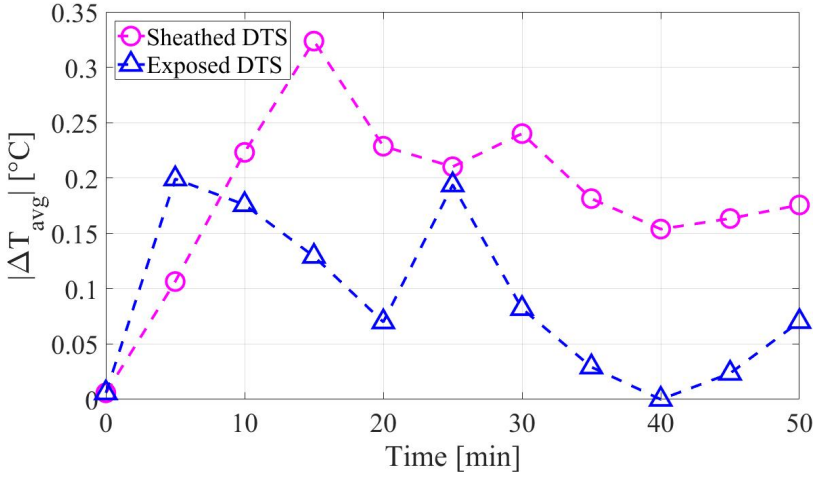

(c)

Figure 9.20: Average of differences along sections of instantaneous transient data. Region 1 is plotted in (a), 2 is plotted in (b), and 3 is plotted in (c).

Unlike the steady-state analysis, the transient analysis presents a few possibly verifiable trends with this analysis. The trends in Figs. 9.20(a) and (c) both indicate a change in sign at 40 minutes into the transient test, which is 5 minutes after boiling started to occur. The trend reversal displayed at 35 minutes in Fig. 9.20(b) could potentially be used to indicate the onset of boiling. Both DTS configurations display these trends and the magnitudes of these results are outside the noise and fluctuation levels of the sheathed DTS.

While not the objective of this analysis, several thermocouples were available for comparison with DTS. Figure 9.21 shows the difference in temperature between thermocouples #5 and #6, corresponding to Z-locations of 0.63 and 0.75, respectively.

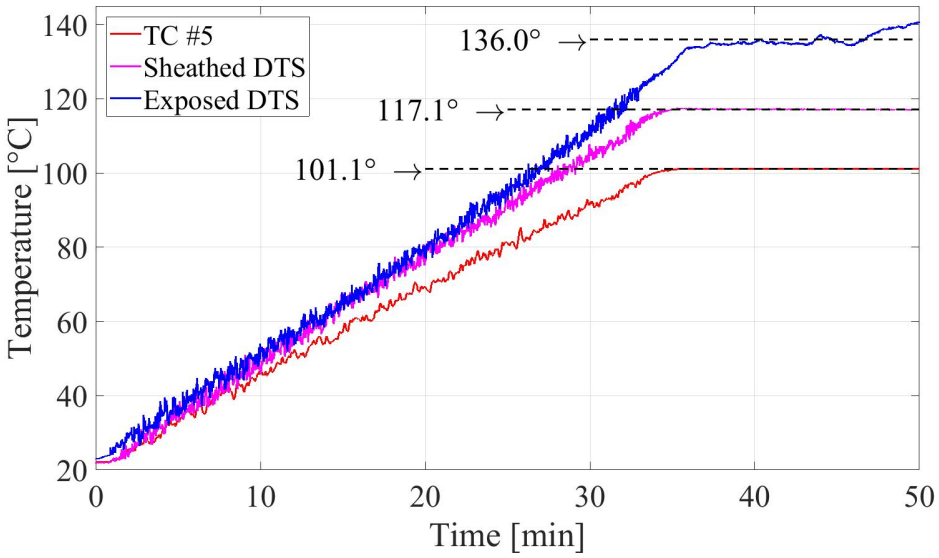

(a)

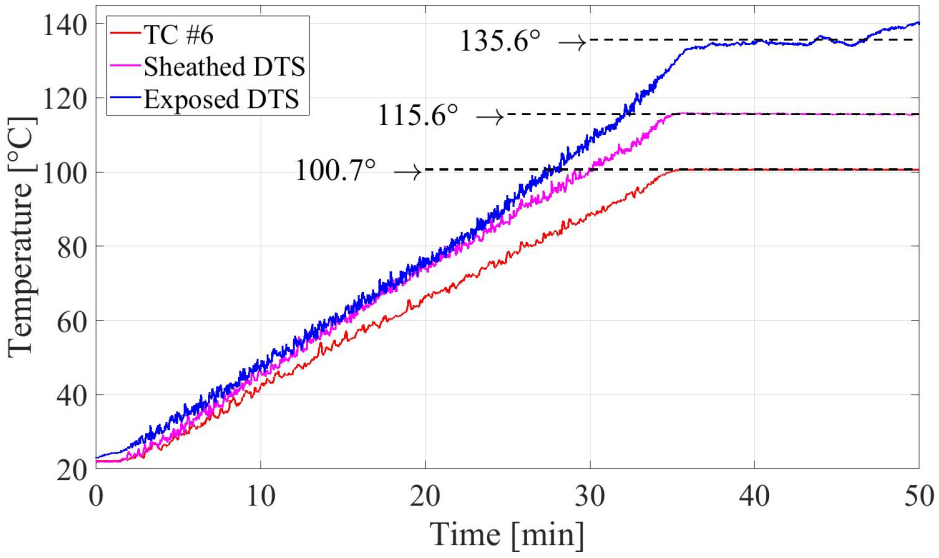

(b)

Figure 9.21: Comparison between temperature sensors during transient testing in two-phase heated vertical pipe.

These final plots highlight the difference observed between measurement techniques. If the DTS were not sensitive to humidity, then such a large difference would likely not be observed. Optic fiber sensors would still require calibration for accurate absolute measurements, but would display different behavior.

More importantly, these final time histories confirm that the system reached saturation at

approximately 35 minutes into testing. At this point in the transient tests, the data in Fig. 9.20(b) show a sharp change in value. This may be an indication of boiling detection. Inflection points are present at 35 minutes in Figs. 9.20(a) and (c), and they may also be indicative of the onset of boiling.

10. SUMMARY AND CONCLUSIONS

The need for higher resolution experimental data will continue to grow as theoretical results continue to increase in resolution and detail. Optic fiber DTS are a viable solution towards providing the high-resolution temperature and strain measurements in demand. Highly detailed temperature measurements in particular are difficult to obtain due to the complexity of the hardware and data processing involved.

In order to implement DTS to these experiments, new installation methods were developed. Surface temperature measurement was achieved with sheathed DTS where the protective capillary tubing was put under tension. New water column measurements were made with exposed DTS, and displayed correctable behavior.

This study has established and proved a methodology to install and perform high-resolution measurements of surface, air, and water temperatures using DTS. These methods can now be used to investigate temperature profiles in many other applications, possibly including those that cannot utilize other temperature measurement techniques.

The thermal behavior of the cooling panel in a natural-circulation facility has been found to be different from the flow behavior under same facility conditions. The surface temperature profile of the panel's heated side was found to be relatively insensitive to flow conditions. This finding is important for the safety system that this facility models.

Liquid water temperature measurements and effects have been studied and quantified with optic fiber DTS. The temperature profiles of a water column and a plume-mixing dome have been characterized with DTS. The heated length in the water column was clearly revealed, and the dome temperature profile showed more uniformity than expected.

Investigations of boiling water with DTS confirmed their integrity, but also their need for correction and potential in boiling detection measurement. With careful analysis and information about the fiber coating, meaningful two-phase measurements can be performed. Overall, these new measurements confirm the usefulness, repeatability, and sensitivity of optic fiber DTS.

Unique high-resolution temperature measurements have been generated. This data can support the validation of specialized high-fidelity computer codes. The measurement density and wide application range of fiber DTS makes it suitable for comparison with results from CFD and FEA. Two-phase boiling conditions were shown to not affect DTS integrity, and useful analyses can be performed. Fiber DTS in a mixing plenum show potential and can be verified with other high-resolution optical techniques.

10.1 Challenges

While the concepts and technology behind optic fiber DTS are fairly mature, a need for measurement verification still exists. This extra step is present in other areas of high-resolution measurement as well. It is also necessary if the users of DTS and other advance measurement techniques wish to convince others that the measurements are valid and trustworthy.

The most difficult challenges overcame in this study were using the optic fiber itself and installing it into facilities that were not initially designed to include fiber sensors. Although the fiber is small and relatively unobtrusive, it becomes difficult to handle in large quantities. Installation of DTS into closed or small spaces proved particularly difficult, but in the end, possible.

The hygroscopic effects of the polyimide-coated fibers must be accounted for in any environment containing water vapor or liquid water. This coating is useful because it displays negligible hysteresis through heat cycles after just one initial heat cycle, but it remains hygroscopic and adds a considerable amount of strain to the fiber sensors. There is potential for removing this coating for specific installations, but uncoated glass fiber becomes extremely fragile. This fiber is currently the best overall choice for most applications despite its coating effects.

Similar to other advanced measurement techniques, DTS measurements require adjustment and correction depending upon their application. The fiber coating and installation materials have considerable effects on the DTS response, and must be accounted for. The adverse effects of thermal expansion and fluid momentum on fiber DTS must be accounted for when making installation decisions. Correction curves can be formed with few collocated thermocouples or other point sensors. Many points of collocation are not necessary, and it is up to the user to determine how many

of these points are needed to justify a DTS measurement. Ideally, methods of fiber construction and installation would be standardized, but since each application of DTS is different in at least one way, this may not be practical.

Uncertainty estimation is always necessary for the proper reporting of any results. The uncertainty estimation performed in this study can be used for any sheathed DTS, which is the safest way to install these sensors.

Unlike the LUNA ODiSI-A50 unit, the ODiSI-B does not have the ability to overlay gages along the fiber sensor. This leads to considerably higher noise levels in the data, albeit with lower sampling rates.

10.2 Further Study

The short-term effects of immersing polyimide-coated DTS into water were accounted for, but long-term studies may be necessary in the future. While most experiments are drained and allowed to reach equilibrium with laboratory conditions between tests, some tests do not. If fiber DTS are to be used long-term in new environments, then any non-physical response must be accounted for.

Further refinements of thermocouple installation technique will benefit the WRCCS facility. Figure 10.1 shows unmasked views of the thermocouple data plotted for each steady flow condition indicated in Fig. 7.13. While some of the temperature gradients in the vertical direction seem reasonable, their values do not correlate well with DTS and are very inconsistent.

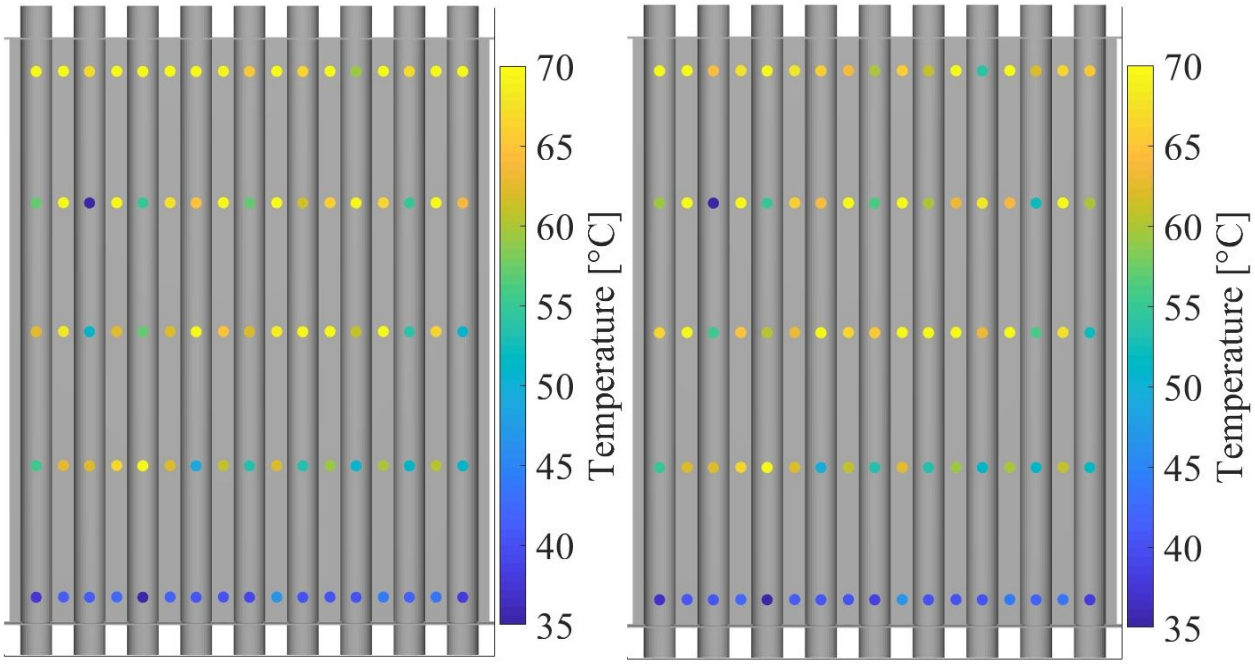

(a) (b)

Figure 10.1: Time-averaged thermocouple recordings of the WRCCS cooling panel wall at steady conditions with the tank valve at 25% (a) and 100% (b).

The implementation of DTS to the HTGR upper plenum facility requires further consideration in order to produce conclusive, reliable measurements. The advantage of this facility is that high-resolution optical techniques can be preformed alongside fiber DTS measurements. These data sets can be used to complement each other and provide more complete measurements of the facility.

Part of the difficulty of operating the HTGR upper plenum facility is its lack of chiller for achieving steady state conditions. Acquiring a chiller and updating the data acquisition software would greatly ease the operation of this facility.

The water and two-phase measurements performed were enough for response evaluation and quantification, but further study will be needed for verification with other sensors. Optic fiber probes and mesh sensors could prove to be useful for verification, and all verification requires collocation with DTS.

Other facilities than those used in this study can also benefit from use of fiber DTS. Molten

salt measurements are one particular application that can benefit greatly from fiber DTS. The high-temperature (up to 700°C), corrosive molten salt environment is not welcoming for many types of sensors. Fiber DTS have been shown to take reliable measurements at temperatures up to 650°C, and when stripped of coating, become inert. Bare glass fibers would need to be sheathed, but they would eliminate any coating effects.

REFERENCES

[1] D.A. Krohn, T.W. MacDougall, and A. Mendez. *Fiber Optic Sensors: Fundamentals and Applications*. SPIE Press, 4 edition, 2015. https://doi.org/10.1117/3.1002910.

[2] W. Allen. The use of fibre optics: A description of the various methods of employing fibre optics and an outline of future developments. *Aircraft Engineering and Aerospace Technology*, 41:33–36, 1969. https://doi.org/10.1108/eb034506.

[3] R.P. Main. Fibre optic sensors - future light. *Sensor Review*, 5:133–139, 1985.

[4] R.C. Hochberg. Fiber-optic sensors. *IEEE Transactions on Instrumentation and Measurement*, IM-35:447–450, 1986. https://doi.org/10.1109/TIM.1986.6499114.

[5] D.A. Jackson and J.D.C. Jones. Fibre optic sensors. *Optical Acta: International Journal of Optics*, 33:1469–1503, 1986. https://doi.org/10.1080/713821914.

[6] P.R. Orrell. Distributed fibre optic sensing. *Sensor Review*, 12:27–31, 1992. https://doi.org/10.1108/eb007876.

[7] G. Oscroft. Intrinsic fibre optic sensors. *Sensor Review*, 12:10–14, 1992. https://doi.org/10.1108/eb007872.

[8] J.P. Dakin. Distributed optical fiber sensors. volume 1797 of *Proceedings of SPIE*. Society of Photo-Optical Instrumentation Engineers, 1993. https://doi.org/10.1117/12.141304.

[9] W.V. Sorin. High-resolution optical fiber reflectometry techniques. volume 1797 of *Proceedings of SPIE*. Society of Photo-Optical Instrumentation Engineers, 1993. https://doi.org/10.1117/12.141281.

[10] R.R. Yamauchi and A.T. Shiota. Practical applications of temperature distribution sensing by raman backscattering in optical fibers. volume 1797 of *Proceedings of SPIE*. Society of Photo-Optical Instrumentation Engineers, 1993. https://doi.org/10.1117/12.141282.

[11] A. Hartog. Distributed fibre-optic temperature sensors: technology and applications in the power industry. *Power Engineering Journal*, 9:114–120, 1995.

[12] S. O'Keeffe, C. Fizpatrick, E. Lewis, and A.I. Al-Shamma'a. A review of optical fibre radiation dosimeters. *Sensor Review*, 28:136–142, 2008. https://doi.org/10.1108/02602280810856705.

[13] M. Jaaskelainen. Fiber optic distributed sensing applications in defense, security, and energy. volume 7316 of *Proceedings of SPIE*. Society of Photo-Optical Instrumentation Engineers, 2009. https://doi.org/10.1117/12.820327.

[14] R. Bogue. Fibre optic sensors: a review of today's applications. *Sensor Review*, 31:304–309, 2011. https://doi.org/10.1108/02602281111169703.

[15] H.M. Hashemian and W.C. Bean. Sensors for next-generation nuclear plants: fiber-optic and wireless. *Nuclear Science and Engineering*, 169:262–278, 2011. https://doi.org/10.13182/NSE10-48.

[16] X. Bao and L. Chen. Recent progress in distributed fiber optic sensors. *Sensors*, 12:8601–8639, 2012. https://doi.org/10.3390/s120708601.

[17] A.D. Kersey. Fiber optic sensors shine bright: industrial applications where fos bring differentiated performance / value. volume 8421 of *Proceedings of SPIE*. Society of Photo-Optical Instrumentation Engineers, 2012. https://doi.org/10.1117/12.2008245.

[18] W. Lin, C. Zhang, L. Li, and S. Liang. Review on development and applications of fiber-optic sensors. 2012 Symposium on Photonics and Optoelectronics. Institute of Electrical and Electronics Engineers, 2012. https://doi.org/10.1109/SOPO.2012.6270996.

[19] M. Willsch. Fiber optical sensors in power generation. volume 8351 of *Proceedings of SPIE*. Society of Photo-Optical Instrumentation Engineers, 2012. https://doi.org/10.1117/12.921746.

[20] H.S. Pradhan and P.K. Sahu. A survey on the performances of distributed fiber-optic sensors. ICMOCE 2015. Institute of Electrical and Electronics Engineers, 2015. https://doi.org/10.1109/ICMOCE.2015.7489736.

[21] R.T. Griffiths and A.A. Nicol. A fibre flowmeter suitable for very low flow rates. *Journal of Scientific Instruments*, 42(11):797–799, 1965. https://doi.org/10.1088/0950-7671/42/11/306.

[22] M.K. Barnoski and S.M. Jensen. Fiber waveguides: A novel technique for investigating attenuation characteristics. *Applied Optics*, 15:2112–2115, 1976. https://doi.org/10.1364/AO.15.002112.

[23] D. Marcuse and H.M. Presby. Optical fiber coating concentricity: measurement and analysis. *Applied Optics*, 16:2383–2390, 1977. https://doi.org/10.1364/AO.16.002383.

[24] G.B. Hocker. Fiber-optic sensing of pressure and temperature. *Applied Optics*, 18:1445–1448, 1979. https://doi.org/10.1364/AO.18.001445.

[25] J.H. Lyle and C.W. Pitt. Vortex shedding fluid flowmeter using optical fibre sensor. *Electronics Letters*, 17:244–245, 1981. https://doi.org/10.1049/el:19810173.

[26] M.K. Barnoski, M.D. Rourke, S.M. Jensen, and R.T. Melville. Optical time domain reflectometer. *Applied Optics*, 16:2375–2379, 1977. https://doi.org/10.1364/AO.16.002375.

[27] W. Eickhoff and R. Ulrich. Optical frequency domain reflectometry in single-mode fiber. *Applied Physics Letters*, 39:693–695, 1981. https://doi.org/10.1063/1.92872.

[28] A. Hartog. A distributed temperature sensor based on liquid-core optical fibers. *Journal of Lightwave Technology*, 1:498–509, 1983. https://doi.org/10.1109/JLT.1983.1072146.

[29] J.P. Dakin, D.J. Pratt, G.W. Bibby, and J.N. Ross. Distributed optical fibre raman temperature sensor using a semiconductor light source and detector. *Electronics Letters*, 21:569–570, 1985. https://doi.org/10.1049/el:19850402.

[30] R. Stierlin, J. Ricka, B. Zysset, R. Battig, H.P. Weber, T. Binkert, and W.J. Borer. Distributed fiber-optic temperature sensor using single photon counting detection. *Applied Optics*, 26:1368–1370, 1987. https://doi.org/10.1364/AO.26.001368.

[31] R. Juskaitis, A.M. Mamedov, V.T. Potapov, and S.V. Shatalin. Distributed interferometric fiber sensor system. *Optics Letters*, 17:1623–1625, 1992. https://doi.org/10.1364/OL.17.001623.

[32] T. Horiguchi, T. Kurashima, and Y. Koyamada. Measurement of temperature and strain distribution by brillouin frequency shift in silica optical fibers. volume 1797 of *Proceedings of SPIE*. Society of Photo-Optical Instrumentation Engineers, 1993. https://doi.org/10.1117/12.141280.

[33] J.P. Kurmer, S.A. Kingsley, J.S. Laudo, and S.J. Krak. Fiber optic acoustic sensor for leak detection. volume 1797 of *Proceedings of SPIE*. Society of Photo-Optical Instrumentation Engineers, 1993. https://doi.org/10.1117/12.141302.

[34] X. Bao, D.J. Webb, and D.A. Jackson. Combined distributed temperature and strain sensor based on brillouin loss in an optical fiber. *Optics Letters*, 19:141–143, 1994. https://doi.org/10.1364/OL.19.000141.

[35] R. Rathod, R.D. Pechstedt, D.A. Jackson, and D.J. Webb. Distributed temperature-change sensor based on rayleigh backscattering in an optical fiber. *Optics Letters*, 19:593–595, 1994. https://doi.org/10.1364/OL.19.000593.

[36] W.A. Gambling and A.H. Hartog. A distributed optical fibre temperature sensor - technology and applications. *HKIE Transactions*, 4:76–81, 1997. https://doi.org/10.1080/1023697X.1997.10667729.

[37] E. Hurtig, S. Grosswig, and K. Kuhn. Distributed fibre optic temperature sensing: a new tool for long-term and short-term temperature monitoring in boreholes. *Energy Sources*, 19:55–62, 1997. https://doi.org/10.1080/00908319708908832.

[38] M. Froggatt and J. Moore. Distributed measurement of static strain in an optical fiber with multiple bragg gratings at nominally equal wavelengths. *Applied Optics*, 37, 1998. https://doi.org/10.1364/AO.37.001741.

[39] C.M. Lawrence, D.V. Nelson, and E. Udd. A fiber optic sensor for transverse strain measurement. *Experimental Mechanics*, 39, 1999. https://doi.org/10.1007/BF02323553.

[40] S. Sakaguchi. Relaxation of rayleigh scattering in silica core optical fiber by heat treatment. *Electronics and Communications in Japan, Part 2*, 83(12):35–41, 2000. https://doi.org/10.1002/1520-6432(200012)83:12<35::AID-ECJB4>3.0.CO;2-U.

[41] K. De Souza and T.P. Newson. Improvement of signal-to-noise capabilities of a distributed temperature sensor using optical preamplification. *Measurement Science and Technology*, 12(7):952–957, 2001. https://doi.org/10.1088/0957-0233/12/7/336.

[42] A. Kimura, E. Takada, K. Fujita, M. Nakazawa, H. Takahashi, and S. Ichige. Application of a raman distributed temperature sensor to the experimental fast reactor joyo with correction techniques. *Measurement Science and Technology*, 12(7):966–973, 2001. https://doi.org/10.1088/0957-0233/12/7/338.

[43] S. Kher, G. Srikant, S. Chaube, A.L.Chakraborty, T.P.S. Nathan, and D.D. Bhawalkar. Design, development and studies on raman-based fibre-optic distributed temperature sensor. *Current Science*, 83(11):1365–1368, 2002.

[44] A. MacLean, C. Moran, W. Johnstone, B. Culshaw, D. Marsh, and P. Parker. Detection of solvents using distributed fibre optic sensor. *Electronics Letters*, 39:1237–1238, 2003. https://doi.org/10.1049/el:20030838.

[45] J.D. Weiss. Using fiber optics to detect moisture intrusion into a landfill cap consisting of a vegetative soil barrier. *Journal of the Air and Waste Management Association*, 53:1130–1148, 2003.

[46] Y. Zhu, P. Shum, C. Lu, M.B. Lacquet, P.L. Swart, A.A. Chtcherbakov, and S.J. Spammer. Temperature insensitive measurements of static displacements using a fiber bragg grating. *Optics Express*, 11:1918–1924, 2003. https://doi.org/10.1364/OE.11.001918.

[47] K.Y. Lee, B.-H. Kim, and J.P. Velas. Development of an intelligent monitoring system with high temperature distributed fiber-optic sensor for fossil-fuel power plants. IEEE Power Engineering Society General Meeting. Institute for Electrical and Electronics Engineers, 2004. https://doi.org/10.1109/PES.2004.1373225.

[48] B.J. Soller, D.K. Gifford, M.S. Wolfe, and M.E. Froggatt. High resolution optical frequency domain reflectometry for characterization of components and assemblies. *Optics Express*, 13(2):666–674, 2005. https://doi.org/10.1364/OPEX.13.000666.

[49] P.R. Stoddart, P.J. Cadusch, J.B. Pearce, D. Vukovic, C.R. Nagarajah, and D.J. Booth. Fibre optic distributed temperature sensor with an integrated background correction function. *Measurement Science and Technology*, 16(6):1299–1304, 2005. https://doi.org/10.1088/0957-0233/16/6/009.

[50] S. Caron, C. Pare, Patrick Paradis, J.-M. Trudeau, and A. Fougeres. Distributed fibre optics polarimetric chemical sensor. *Measurement Science and Technology*, 17(5):1075–1081, 2006. https://doi.org/10.1088/0957-0233/17/5/S23.

[51] L. Yuan and J. Yang. A fibre-optic low-coherence quasi-distributed strain sensing system with multi-configurations. *Measurement Science and Technology*, 18(9):2931–2937, 2007. https://doi.org/10.1088/0957-0233/18/9/024.

[52] D. Fan, D.-S. Jiang, and W.-L. Li. Experiment study of fiber optic sensing in railway security monitoring. 1st Asia-Pacific Optical Fiber Sensors Conference. Institute of Electrical and Electronics Engineers, 2008. https://doi.org/10.1109/APOS.2008.5226310.

[53] F. Matta, F. Bastianini, N. Galati, P. Casadei, and A. Nanni. Distributed strain measurement in steel bridge with fiber optic sensors: validation through diagnostic load test. *Journal of*

Performance of Constructed Facilities, 22(4):264–273, 2008. https://doi.org/10.1061/(ASCE)0887-3828(2008)22:4(264).

[54] A.K. Sang, M.E. Froggatt, D.K. Gifford, S.T. Kreger, and B.D. Dickerson. One centimeter spatial resolution temperature measurements in a nuclear reactor using rayleigh scatter in optical fiber. *IEEE Sensors Journal*, 8:1375–1380, 2008. https://doi.org/10.1109/JESN.2008.927247.

[55] A.A. Stolov, D.A. Simoff, and J. Li. Thermal stability of specialty optic fibers. *Journal of Lightwave Technology*, 26(20):3443–3451, 1008. https://doi.org/10.1109/JLT.2008.925698.

[56] Z. Dai, X. Zhang, Z. Peng, J. Li, Z. Ou, and Y. Liu. Distributed fiber optic stress sensor system based on P-OFDR. volume 7659 of *Proceedings of SPIE*. Society of Photo-Optical Instrumentation Engineers, 2010. https://doi.org/10.1117/12.866062.

[57] X. Feng, C. Sun, X. Zhang, and F. Ansari. Determination of the coefficient of thermal expansion with embedded long-gauge fiber optic sensors. *Measurement Science and Technology*, 21(6), 2010. https://doi.org/10.1088/0957-0233/21/6/065302.

[58] P.S. Hsu, A.K. Patnaik, J.R. Gord, T.R. Meyer, W.D. Kulatilaka, and S. Roy. Investigation of optical fibers for coherent anti-stokes raman scattering (CARS) spectroscopy in reacting flows. *Experiments in Fluids*, 49:969–984, 2010. https://doi.org/10.1007/s00348-010-0961-6.

[59] S. Liehr and K. Krebber. A novel quasi-distributed fibre optic displacement sensor for dynamic measurement. *Measurement Science and Technology*, 21(7), 2010. https://doi.org/10.1088/0957-0233/21/7/075205.

[60] T. Reinsch and J. Henninges. Temperature-dependent characterization of optical fibres for distributed temperature sensing in hot geothermal wells. *Measurement Science Technology*, 21(9), 2010. https://doi.org/10.1088/0957-0233/21/9/094022.

[61] M. Kasinathan, S. Sosamma, C. Pandian, V. Vijayakumar, S. Chandramouli, B.K. Nashine, C. Babu Rao, N. Murali, K.K. Rajan, and T. Jayakumar. Fiber optic sensors for monitoring

sodium circuits and power grid cables. ANIMMA 2. Institute for Electrical and Electronics Engineers, 2011. https://doi.org/10.1109/ANIMMA.2011.6172875.

[62] M. Kasinathan, S. Sosamma, C. Babu Rao, A. Kumar, B. Purna Chandra Rao, N. Murali, K.K. Rajan, and T. Jayakumar. Monitoring sodium circuits and acsr cables using fiber optic sensors. ANIMMA 3. Institute for Electrical and Electronics Engineers, 2013. https://doi.org/10.1109/ANIMMA.2011.6172875.

[63] M. Kasinathan, S. Sosamma, C. Babu Rao, A. Kumar, B. Purna Chandra Rao, N. Murali, and T. Jayakumar. Monitoring sodium circuits using fiber optic sensors. *IEEE Transactions on Nuclear Science*, 61(4):1971–1976, 2014. https://doi.org/10.1109/TNS.2014.2328355.

[64] M.T.V. Wylie, B.G. Colpitts, and A.W. Brown. Fiber optic distributed differential displacement sensor. *Journal of Lightwave Technology*, 29(18):2847–2852, 2011. https://doi.org/10.1109/JLT.2011.2165527.

[65] S. Lomperski, C. Gerardi, and D.W. Pointer. Distributed fiber optic temperature sensing for CFD code validation. NURETH 15, Pisa, Italy, 2013. American Nuclear Society.

[66] S. Lomperski, C. Gerardi, and W.D. Pointer. Fiber optic distributed temperature sensor mapping of a jet-mixing flow field. *Experiments in Fluids*, 56:1–16, 2015. https://doi.org/10.1007/s00348-015-1918-6.

[67] A. Mirzaei, A.R. Bahrampour, M. Taraz, A. Bahrampour, M.J. Bahrampour, and S.M. Ahmadi Foroushani. Transient response of buried oil pipelines fiber optic leak detector based on the distributed temperature measurement. *International Journal of Heat and Mass Transfer*, 65:110–122, 2013. https://doi.org/10.1016/j.ijheatmasstransfer.2013.05.062.

[68] Y. Wang, B. Yang, and L. Liang. Measurement and analysis of high temperature using distributed fiber optic sensor. *International Journal of Smart Sensing and Intelligent Systems*, 7(4):1596–1612, 2014. https://doi.org/10.21307/ijssis-2017-722.

[69] T.W. Wood, B. Blake, T.E. Blue, C.M. Petrie, and D. Hawn. Evaluation of the performance of distributed temperature measurements with single-mode fiber using rayleigh backscatter

up to 1000 c. *IEEE Sensors Journal*, 14:124–128, 2014. https://doi.org/10.1109/JSEN.2013.2280797.

[70] D.D. Lisowski, C.D. Gerardi, and S.W. Lomperski. Thermal cycling testing of distributed fiber optic temperature sensors for high-temperature applications. NURETH 16, Chicago, IL, 2015. American Nuclear Society.

[71] J. Jin, H. Zhang, J. Liu, and Y. Li. Distributed temperature sensing based on rayleigh scattering in irradiated optical fiber. *IEEE Sensors Journal*, 16(24):8928–8935, 2016. https://doi.org/10.1109/JSEN.2016.2615945.

[72] J. Xu, Y. Dong, Z. Zhang, S. Li, S. He, and H. Li. Full scale strain monitoring of a suspension bridge using high performance distributed fiber optic sensors. *Measurement Science and Technology*, 27(12), 2016. https://doi.org/10.1088/0957-0233/27/12/124017.

[73] H. Hoff. Using distributed fibre optic sensors for detecting fires and hot rollers on conveyor belts. IEEE Sensors Journal. Institute for Electrical and Electronics Engineers, 2017. https://doi.org/10.1109/OFSIS.2017.9.

[74] S. Lomperski, N. Bremer, and C. Gerardi. Distributed temperature sensing inside a 19-rod bundle. *Nuclear Engineering and Design*, 319:201–209, 2017. https://doi.org/10.1016/j.nucengdes.2017.05.008.

[75] C. Gerardi, N. Bremer, D. Lisowski, and S. Lomperski. Distributed temperature sensor testing in liquid sodium. *Nuclear Engineering and Design*, 312:59–65, 2017. https://doi.org/10.1016/j.nucengdes.2016.06.017.

[76] T. Ringel, M. Willsch, and T. Bosselmann. Rayleigh-based distributed temperature sensing and fiber bragg grating point temperature sensing with a single optical fiber on high electrical potential of 1 MV. OFS 25. Institute for Electrical and Electronics Engineers, 2017. https://doi.org/10.1117/12.2263288.

[77] P.J. Thomas and J.O. Hellevang. A fully distributed fibre optic sensor for relative humidity measurements. *Sensors and Actuators B: Chemical*, 247, 2017. https://doi.org/10.1016/j.snb.2017.02.027.

[78] C.A. Nixon, W.R. Marcum, and A.W. Weiss. On the fluid structure interactions of a wire-wrapped pin bundle. ATH 2018, pages 493–504. American Nuclear Society, 2018.

[79] B. Liu, X. Ma, X. Wang, C. Dang, Q. Wang, and R. Bennacer. Experimental study of the chimney effect in a solar hybrid double wall. *Solar Energy*, 115:1–9, 2015. https://doi.org/10.1016/j.solener.2015.02.012.

[80] Z. Zhang an dZ. Sun and C. Duan. A new type of passive solar energy utilization technology - the wall implanted with heat pipes. *Energy and Buildings*, 84:111–116, 2014. https://doi.org/10.1016/j.enbuild.2014.08.016.

[81] Z. Sun, Z. Zhang, and C. Duan. The applicability of the wall implanted with heat pipes in winter of china. *Energy and Buildings*, 104:36–46, 2015. https://doi.org/10.1016/j.enbuild.2015.06.082.

[82] R. Tan and Z. Zhang. Heat pipe structure on heat transfer and energy saving performance of the wall implanted with heat pipes during the heating season. *Applied Thermal Engineering*, 102:633–640, 2016. https://doi.org/10.1016/j.applthermaleng.2016.03.085.

[83] Z. Li and Z. Zhang. Dynamic heat transfer characteristics of wall implanted with heat pipes in summer. *Energy & Buildings*, 170:40–46, 2018. https://doi.org/10.1016/j.enbuild.2018.03.071.

[84] A.-J.N. Khalifa. Natural convective heat transfer coefficient - a review ii. surfaces in two- and three-dimensional enclosures. *Energy and Conversion Management*, 42:505–517, 2001. https://doi.org/10.1016/S0196-8904(00)00043-1.

[85] A. Bairi, E. Zarco-Pernia, and J.-M. Garcia de Maria. A review on natural convection in enclosures for engineering applications. the particular case of the parallelogrammic

diode cavity. *Applied Thermal Engineering*, 63:304–322, 2014. https://doi.org/10.1016/j.applthermaleng.2013.10.065.

[86] H. Karatas and T. Derbentli. Natural convection in rectangular cavities with one active vertical wall. *International Journal of Heat and Mass Transfer*, 105:305–315, 2017. https://doi.org/10.1016/j.ijheatmasstransfer.2016.09.100.

[87] H. Karatas and T. Derbentli. Natural convection and radiation in rectangular cavities with one active vertical wall. *International Journal of Thermal Sciences*, 123:129–139, 2018. https://doi.org/10.1016/j.ijthermalsci.2017.09.006.

[88] W.M. Lewandowski, M. Ryms, and H. Denda. Infrared techniques for natural convection investigations in channels between two vertical, parallel, isothermal and symmetrically heated plates. *International Journal of Heat and Mass Transfer*, 114:958–969, 2017. https://doi.org/10.1016/j.ijheatmasstransfer.2017.06.120.

[89] W.M. Lewandowski, M. Ryms, and H. Denda. Natural convection in symmetrically heated vertical channels. *International Journal of Thermal Sciences*, 134:530–540, 2018. https://doi.org/10.1016/j.ijthermalsci.2018.08.036.

[90] H. Yamaguchi, X.-R. Zhang, and K. Fujima. Basic study on new cryogenic refrigeration using CO_2 solid–gas two phase flow. *International Journal of Refrigeration*, 31:404–410, 2008. https://doi.org/10.1016/j.ijrefrig.2007.08.001.

[91] S. Sadhu, M. Ramgopal, and S. Bhattacharyya. Steady-state analysis of a high-temperature natural circulation loop based on water-cooled supercritical CO_2. *Journal of Heat Transfer*, 140, 2018. https://doi.org/10.1115/1.4038541.

[92] V.C. Thalange, E. Pal, N. Minocha, A.K. Nayak, S.M. Mahajani, S.V. Panse, and J.B. Joshi. Thermal hydraulics of natural circulation loop in beam-down solar power tower. *Energy*, 159:1088–1101, 2018. https://doi.org/10.1016/j.energy.2018.06.156.

[93] H. Bao, Y. Guo, S. Liu, and C. Peng. Experimental study on natural circulation heat transfer of square channel in water-cooled blanket. volume 46 of *IEEE Transactions on*

Plasma Science, pages 2291–2300. Institute for Electrical and Electronics Engineers, 2018. https://doi.org/10.1109/TPS.2018.2830643.

[94] R.C. Briant and A.M. Weinberg. Molten fluorides as power reactor fuels. *Nuclear Science and Engineering*, 2:797–803, 1957. https://doi.org/10.13182/NSE57-A35494.

[95] A.M. Weinberg. Some aspects of fluid fuel reactor development. *Nuclear Science and Engineering*, 8:346–360, 1960. https://doi.org/10.13182/NSE60-A28865.

[96] Jr. G.L. Yoder, D. Heatherly, and M. Caja. Natural convection heat transfer experiments in fluoride salt. *Journal of Heat Transfer*, 140(042501), 2018. https://doi.org/10.1115/1.4038132.

[97] K. Britsch, M. Anderson, P. Brooks, and K. Sridharan. Natural circulation flibe loop overview. *International Journal of Heat and Mass Transfer*, 134:970–983, 2019. https://doi.org/10.1016/j.ijheatmasstransfer.2018.12.180.

[98] J.Y. Kudariyawar, A.K. Srivastava, A.M. Vaidya, N.K. Maheshwari, and P. Satyamurthy. Computational and experimental investigation of steady state and transient characteristics of molten salt natural circulation loop. *Applied Thermal Engineering*, 99:560–571, 2016. https://doi.org/10.1016/j.applthermaleng.2015.12.114.

[99] A.K. Srivastava, J.Y. Kudariyawar, A. Borgohain, S.S. Jana, N.K. Maheshwari, and P.K. Vijayan. Experimental and theoretical studies on the natural circulation behavior of molten salt loop. *Applied Thermal Engineering*, 98:513–521, 2016. https://doi.org/10.1016/j.applthermaleng.2015.12.065.

[100] Z. Yang, Z. Meng, C. Yan, and K. Chen. Heat transfer and flow characteristics of a cooling thimble in a molten salt reactor residual heat removal system. *Nuclear Engineering and Technology*, 49:1617–1628, 2017. https://doi.org/10.1016/j.net.2017.07.026.

[101] K. Chen, Z. Meng, C. Yan, G. Fan, and T. Ding. Experimental study on start-up and steady state characteristics of passive residual heat removal system for 2 MW molten salt reactor. *Energy*, 147:826–838, 2018. https://doi.org/10.1016/j.energy.2018.01.057.

[102] D.D. Lisowski, C.D. Gerardi, D.J. Kilsdonk, N.C. Bremer, S.W. Lomperski, R. Hu, A.R. Kraus, M.D. Bucknor, Q. Lv, T. Lee, and M.T. Farmer. Final report on RCCS testing with the air-based NSTF. Technical Report ANL-ART-47, Argonne National Laboratory, United States, August 2016.

[103] D.D. Lisowski, A.R. Kraus, M.D. Bucknor, R. Hu, and M.T. Farmer. Experimental observations of natural circulation flow in the NSTF. *Nuclear Engineering and Design*, 306:124–132, 2016. https://doi.org/10.1016/j.nucengdes.2016.01.014.

[104] C. Tompkins, M. Corradini, and M. Anderson. Temperature profiles and mixing in a natural-circulation cooling facility via distributed optical sensors. *Nuclear Technology*, 196:346–354, 2016. https://doi.org/10.13182/NT16-26.

[105] T.Y.S.A.A. Alhashimi. Measurement of temperature profile in the reactor cavity cooling system. Master's thesis, Texas A&M University, 2014.

[106] S.A. Sulaiman, E.E. Dominguez-Ontiveros, T. Alhashimi, J.L. Budd, M.D. Matos, and Y.A. Hassan. Design considerations and experimental observations for the TAMU air-cooled reactor cavity cooling system for the VHTR. volume 1659 of *AIP Conference Proceedings*, 2015. https://doi.org/10.1063/1.4916850.

[107] A. Frisani, Y. Hassan, and V.M. Ugaz. Computational fluid dynamics analysis of very high temperature gas-cooled reactor cavity cooling system. *Nuclear Technology*, 176:238–259, 2011. https://doi.org/10.13182/NT11-A13299.

[108] D.D. Lisowski, T.C. Haskin, A. Tokuhiro, M.H. Anderson, and M.L. Corradini. Study on the behavior of an asymmetrically heated reactor cavity cooling system with water in single phase. *Nuclear Technology*, 183:75–87, 2013. https://doi.org/10.13182/NT13-A16993.

[109] R. Vaghetto and Y. Hassan. Experimental investigation of a scaled water-cooled reactor cavity cooling system. *Nuclear Technology*, 187:282–293, 2014. https://doi.org/10.13182/NT13-130.

[110] M. Corradini. Experimental studies of NGNP reactor cavity cooling system with water. Technical Report 09-781, U.S. Department of Energy Nuclear Engineering University Program, December 2012.

[111] D.D. Lisowski, O. Omotowa, M.A. Muci, A. Tokuhiro, M.H. Anderson, and M.L. Corradini. Influences of boil-off on the behavior of a two-phase natural circulation loop. *International Journal of Multiphase Flow*, 60:135–148, 2014. https://doi.org/10.1016/j.ijmultiphaseflow.2013.12.005.

[112] N. Quintanar, S. Yang, L. White, R. Vaghetto, and Y. Hassan. Temperature distribution in a scaled 9 riser water reactor cavity cooling system (WRCCS). volume 117 of *Transactions of ANS*, pages 1542–1545. American Nuclear Society, 2017.

[113] D. Holler, R. Vaghetto, and Y. Hassan. New plenum design for a reactor cavity cooling system experimental apparatus. volume 117 of *Transactions of ANS*, pages 104–107. American Nuclear Society, 2017.

[114] D. Holler, R. Vaghetto, and Y. Hassan. Distributed wall temperature measurements in a scaled water-cooled RCCS. volume 119 of *Transactions of ANS*, pages 146–148. American Nuclear Society, 2018.

[115] N.R. Quintanar, T. Nguyen, R. Vaghetto, and Y.A. Hassan. Natural circulation flow distribution within a multi-branch manifold. *International Journal of Heat and Mass Transfer*, 135:1–15, 2019. https://doi.org/10.1016/j.ijheatmasstransfer.2019.01.102.

[116] H.S. Lim, N. i. Tak, S.N. Lee, and C.K. Jo. Water-jacket reactor cavity cooling system concept to mitigate severe accident consequence of high temperature gas-cooled reactor. *Nuclear Engineering and Design*, 340:156–165, 2018. https://doi.org/10.1016/j.nucengdes.2018.09.029.

[117] I. Wygnanski and H. Fiedler. Some measurements in the self-preserving jet. *Journal of Fluid Mechanics*, 38(3):577–612, 1969. https://doi.org/10.1017/S0022112069000358.

[118] W.R. Quinn and J. Militzer. Effects of nonparallel exit flow on round turbulent free jets. *International Journal of Heat and Fluid Flow*, 10(2):139–145, 1989. https://doi.org/10.1016/0142-727X(89)90008-8.

[119] H.J. Hussein, S.P. Capp, and W.K. George. Velocity measurements in a high-reynolds-number, momentum-conserving, axisymmetric, turbulent jet. *Journal of Fluid Mechanics*, 258:31–75, 1994. https://doi.org/10.1017/S002211209400323X.

[120] H. Fellouah, C.G. Ball, and A. Pollard. Reynolds number effects within the development region of a turbulent round free jet. *International Journal of Heat and Mass Transfer*, 52(17-18):3943–3954, 2009. https://doi.org/10.1016/j.ijheatmasstransfer.2009.03.029.

[121] C.G. Ball, H. Fellouah, and A. Pollard. The flow field in turbulent round free jets. *Progress in Aerospace Sciences*, 50:126, 2012. https://doi.org/10.1016/j.paerosci.2011.10.002.

[122] I. Welling, H. Koskela, and T. Hautalampi. Experimental study of the natural-convection plume from a heated vertical plate. *Experimental Heat Transfer*, 11:135–149, 1998. https://doi.org/10.1080/08916159808946558.

[123] S. Grafsronningen, A. Jensen, and B.A.P. Reif. Piv investigation of buoyant plume from natural convection heat transfer above a horizontal heated cylinder. *International Journal of Heat and Mass Transfer*, 54:4975–4987, 2011. https://doi.org/10.1016/j.ijheatmasstransfer.2011.07.011.

[124] D.R. Webster, P.J.W. Roberts, and L. Ra'ad. Simultaneous DPTV/PLIF measurements of a turbulent jet. *Experiments in Fluids*, 30(1):65–72, 2001. https://doi.org/10.1007/s003480000137.

[125] J.B. Mi, P. Kalt, G.J. Nathan, and C.Y. Wong. PIV measurements of a turbulent jet issuing from round sharp-edged plate. *Experiments in Fluids*, 42(4):625–637, 2007. https://doi.org/10.1007/s00348-007-0271-9.

[126] I.M. Milanovic and K.J. Hammad. PIV study of the near-field region of a turbulent round jet. Third Joint US-European Fluids Engineering Summer Meeting, pages

1353–1361. American Society of Mechanical Engineers, 2010. https://doi.org/10.1115/FEDSM-ICNMM2010-31139.

[127] T. Guo, M.J. Rau, P.P. Vlachos, and S.V. Garimella. Axisymmetric wall jet development in confined jet impingement. *Physics of Fluids*, 29(2):025102, 2017. https://doi.org/10.1063/1.4975394.

[128] G.E. McCreery and K.G. Condie. Experimental modeling of VHTR plenum flows during normal operation and pressurized conduction cooldown. Technical Report INL/EXT-06-11760, September 2006.

[129] K.L. McVay, J.-H. Park, S. Lee, Y.A. Hassan, and N.K. Anand. Preliminary tests of particle image velocimetry for the upper plenum of a scaled model of a very high temperature gas cooled reactor. *Progress in Nuclear Energy*, 83:305–317, 2015. https://doi.org/10.1016/j.pnucene.2015.04.004.

[130] A. Alwafi, T. Nguyen, Y. Hassan, and N.K. Anand. Time-resolved particle image velocimetry measurements of a single impinging jet in the upper plenum of a scaled facility of high temperature gas-cooled reactors. *International Journal of Heat and Fluid Flow*, 76:113–129, 2019. https://doi.org/10.1016/j.ijheatfluidflow.2019.02.003.

[131] Ph. Graindorge, G. Le Boudec, D. Meyet, and H.J. Arditty. High bandwidth two-phase flow void fraction fiber optic sensor. volume 0586 of *Proceedings of SPIE*, pages 211–214, 1986. https://doi.org/10.1117/12.951167.

[132] H. Yan, W.W. Yuen, and T.G. Theofanous. The use of fluorescence in the measurement of local liquid content in transient multiphase flows. *Nuclear Engineering and Design*, 141:315–328, 1993. https://doi.org/10.1016/0029-5493(93)90109-M.

[133] J.W. Berthold, S.E. Reed, and C.A. Nash. Fibre optic sensor system for void fraction measurement in aqueous two-phase fluids. *Flow Measurement and Instrumentation*, 5:3–13, 1994. https://doi.org/10.1016/0955-5986(94)90003-5.

[134] M.K. El-Kamash, M.R. Loewen, and N. Rajaratnam. Measurements of void fraction and bubble properties on a stepped chute using a fiber-optic probe. *Canadian Journal of Civil Engineering*, 32:636–643, 2005. https://doi.org/10.1139/L05-014.

[135] G. Rojas and M.R. Loewen. Fiber-optic probe measurements of void fraction and bubble size distributions beneath breaking waves. *Experiments in Fluids*, 43:895–906, 2007. https://doi.org/10.1007/s00348-007-0356-5.

[136] M. Yamada and T. Saito. A newly developed photoelectric optical fiber probe for simultaneous measurements of a CO_2 bubble chord length, velocity, and void fraction and the local CO_2 concentration in the surrounding liquid. *Flow Measurement and Instrumentation*, 27:8–19, 2012. https://doi.org/10.1016/j.flowmeasinst.2012.04.004.

[137] K. Delwiche, S. Senft-Grupp, and H. Hemond. A novel optical sensor designed to measure methane bubble sizes in situ. *Limnology and Ocenography: Methods*, 13:712–721, 2015. https://doi.org/10.1002/lom3.10060.

[138] H. Ide, R. Kimura, and M. Kawaji. Optical measurement of void fraction and bubble size distributions in a microchannel. *Heat Transfer Engineering*, 28:713–719, 2007. https://doi.org/10.1080/01457630701328031.

[139] V.H.V. Baroncini, C. Martelli, M.J. Da Silva, and R.E.M. Morales. Single and two-phase flow characterization using optical fiber bragg gratings. *Sensors*, 15:6549–6559, 2015. https://doi.org/10.3390/s150306549.

[140] A.M. Aliyu, Y.K. Kim, S.H. Choi, J.H. Ahn, and K.C. Kim. Development of a dual optical fiber probe for the hydrodynamic investigation of a horizontal annular drive gas/liquid ejector. *Flow Measurement and Instrumentation*, 56:45–55, 2017. https://doi.org/10.1016/j.flowmeasinst.2017.07.005.

[141] Moisture absorption of polyimide mlbs. Technical report, ARLON Electronic Materials. http://www.arlonemd.com/wp-content/uploads/2016/05/Moisture-Absorption-of-Polyimide-MLBs-v1.1-2016.pdf.

[142] D. Hu and H. Chen. Humidity effect on polyimide film adhesion. *Journal of Materials Science*, 27:5262–5268, 1992. https://doi.org/10.1007/BF02403827.

[143] G.Q. Chen, C.A. Scholes, G.G. Qiao, and S.E. Kentish. Water vapor permeation in polyimide membranes. *Journal of Membrane Science*, 379:479–487, 2011. https://doi.org/10.1016/j.memsci.2011.06.023.

[144] M. Akram, K.M.B. Jansen, S. Bhowmik, and L.J. Ernst. Moisture absorption analysis of high performance polyimide adhesive. 10 2011. https://doi.org/10.13140/2.1.2671.6807.

[145] S. Lo, T. Eppinger, and R. Aglave. Cfd modelling of multi-regime multiphase flows. 2018 AIChE Annual Meeting. American Institute of Chemical Engineers, 2018.

APPENDIX A

OPTIC FIBER MATERIALS AND EQUIPMENT

A.1 Sensing Fiber Specifications

OFS Fitel, LLC
Headquarters
2000 Northeast Expressway
Norcross, GA 30071 USA
Phone:+1 770.798.5555
Phone:+1 888.342.3743 [USA and Canada]
Website: www.ofsoptics.com

Item # BF06160-02, ClearLite® POLY 1310 21 NA Photonic Fibers

These fibers are designed to operate efficiently at both 1310 and 1550 nm, and the higher NA significantly enhances bend performance. As a result, these fibers are ideal for harsh environment installations where fiber compression is a concern and where low-loss, small bend-radius coiling and winding performance is desired. Various coatings and buffer sizes are offered to meet environmental requirements and size constraints.

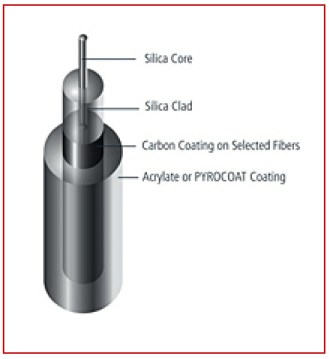

Optical Properties | Dimensions/Geometric Properties | Coating/Buffer Descriptions | Mechanical and Testing Data | How To Order: | Typical Applications | Options

Optical Properties

Type	Single-Mode
Operating Wavelength	1550 nm
Cutoff Wavelength	≤ 1290 nm
Mode Field Diameter	@ 1310 nm, 5.1 ± 1.0 µm @ 1550 nm, 5.8 ± 1.0 µm
Attenuation	@ 1310 nm, ≤ 1.2 dB/km @ 1550 nm, ≤ 0.9 dB/km
Numerical Aperture (Nominal)	0.21

Dimensions/Geometric Properties

Core Diameter (Nominal)	4.6 µm
Clad Diameter	125 ± 2 µm
Coating/Buffer Diameter	155 ± 5 µm
Clad Non-Circularity	≤ 2.0%
Core/Clad Offset	≤ 1.0 µm

Coating/Buffer Descriptions

Coating Material	PYROCOAT®
Operating Temperature	-65 to +300 ºC

Mechanical and Testing Data

Short-Term Bend Radius	≥ 10 mm
Long-Term Bend Radius	≥ 17 mm
Proof Test Level	≥ 100 kpsi 0.689 GPa

How To Order:

Product Description Code	SMB-G1310H
Order From Location	AVON LOCATION 1.888.438.9936 toll-free in the United States and Canada 1.860.678.0371 from outside the U.S.A. 55 Darling Drive Avon, CT 06001, USA
Order By Item #	BF06160-02
Note	OFS polyimide optical fibers are known to operate in environments up to 300 °C. Performance is application dependent. Contact our Technical Sales department to discuss your specific application requirements. 1-860-678-6636

Typical Applications

High Temperature Environments
High-Application-Stress and Tight-Coil Applications
Oil and Gas Applications

A.2 Termination (Coreless) Fiber Specifications

OFS Fitel, LLC
Headquarters
2000 Northeast Expressway
Norcross, GA 30071 USA
Phone:+1 770.798.5555
Phone:+1 888.342.3743 [USA and Canada]
Website: www.ofsoptics.com

Item # F26521, 125 µm Coreless/Polyimide Termination Optical Fiber

Termination optical fiber is a coreless silica fiber. It is useful for eliminating back reflections from unused branches of a multi-port device as well as performing return loss measurement.

A termination of better than 65 dB is achieved by splicing approximately 0.25 meters of this fiber to the desired component. A fusion splice also provides higher reliability and long-term stability over conventional termination methods.

There is excellent repeatability since there is no potential for subsurface damage, fiber breakage, or fiber contamination as with polished or angled cleaves. A quality termination using a patented method (U.S. Patent No. 5,263,103) is possible for all fiber designs including high delta fibers such as erbium-doped fiber.

less

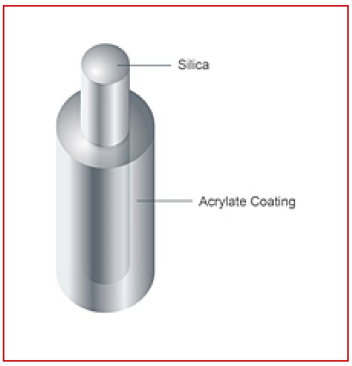

Coating/Buffer Descriptions | Dimensions/Geometric Properties | Mechanical and Testing Data | How To Order:

Coating/Buffer Descriptions

Coating Material	PYROCOAT®
Operating Temperature Range	-65 to +300 ºC

Dimensions/Geometric Properties

Glass Diameter (detail)	125 ± 2 µm
Core Non-Circularity	< 2 %
Coating Diameter (detail)	155 ± 5 µm
Coating Concentricity	≥ 80%

Mechanical and Testing Data

Proof Test Level	≥ 100 kpsi

How To Order:

Note	OFS polyimide optical fibers are known to operate in environments up to 300 °C. Performance is application dependent. Contact our Technical Sales department to discuss your specific application requirements. 1-860-678-6636

A.3 Fusion Splicer Specifications

Precision Rated Optics
Work with a PRO!

OFS-935C *Fusion Splicer*

With innovative design and precise manufacturing technology, the OFS-935C gives users an unparalleled experience. Cutting-edge splicing improvements and new technology greatly reduce splicing and heating time. Its advanced estimate method and core alignment technique ensure the accuracy of splice loss estimation. Additionally, its small size, compact design and reliable protection shell make it suitable for any operating environment. A dynamic operation interface and automatic splice mode gives the user added efficiency.

- 4.3" Touch Screen
- Waterproof, Dustproof, Anti-Shock
- SOC Compatible

OFS-935C Series Standard Package Includes:

Splicer, Power Cord, Stripper, AC Adapter, Battery, SOC Holder, SOC Heater Block, Cooling Tray, Electrode Set, Shoulder Strap, USB Cable, User Manual, Hard Carrying Case.

Ordering Information

OFS-935C-K1	Fusion Splicer Standard Package
OFS-935C-K2	Fusion Splicer Standard Package + Precision Cleaver
OFS-935C-K3	Fusion Splicer Standard Package + Precision Cleaver + Spare Battery + Car Charger + Spare Electrodes

SPECIFICATIONS

Splicing Method	Economical & High Performance Core Alignment Splicer
Average Loss	(SM)0.02dB, (MM)0.01dB, (DS)0.04dB, (NZDS)0.04dB, (G.657)0.02dB
Return Loss	>>60dB
Splice Time	9s average SM / SM 7s Quick mode
Electrode Lifespan	>3,500 arcs
Applicable Fiber	SM(ITU-TU.625. MM(ITU-TU.651), DS(ITU-T G.653). NZDS(ITU-T.655), G657A, G657B 0.25mm, 0.9mm, 2.0mm, 2.4mm, 3.0mm, FLAT(Indoor cable)
Cleaved Length	Coating Diameter< 0 .25mm ~ 8-16mm, Coating Diameter> 0.25mm = 16mm minimum
Coating Diameter	100~1,000 um
Cladding Diameter	80~150um
Heating Programs	Factory installed mode: 9, User Installable mode: 23
Heating Time	Typical 18s
Protection Sleeve	40mm, 60mm, SOC Connector
Data Output	HDMI
Splice Programs	Factory Installed Mode: 33, User Installable Mode: 70+-
Splice Memory	Up to 2,000 Records and 2,000 Splice Images
Battery	Typical 200 Cycles (Splice & Heat) / Single Battery
Power Supply	AC 100-240V Input or DC9-14V
Monitor	Color 4.3" LCD Monitor, with Touch Screen (Tempered Glass)
Cameras	2 CCD Camera System
Magnification	XY style: 150 Power, X/Y: 300 Power
Fiber Display	X /Y or XY, Single X.Y
Size/Weight (WxDxH)	5.47" x 4.84" x 5.11"in / 3.02lb (139 x 123 x 130mm / 1.37Kg w/o Battery)
Operating Environment	Elevation: 0-5,000 Meters,Temp: -40~176°F (-40~80°C), 0-95% Relative Humidity
Wind Protection	The Max Wind Speed 15m/s
Storage Conditions	Temp: -40~176°F (-40~80°C), 0-95% Relative Humidity, Battery: -4~86°F (-20-30°C)
Pull Test	1.96~2.25N (Standard)

P/N: OFS-935C v.10.06.15

www.PrecisionRatedOptics.com
Tel: (888) 545-1254 • Fax: (415) 358-4602 • Email: Sales@PrecisionRatedOptics.com

APPENDIX B

DATA ACQUISITION HARDWARE INFORMATION

Item	*SN*	*Item*	*SN*
NI SCXI-1001	162DA38	NI SCXI-1600	015E99E7
NI SCXI-1121	B7F09A	NI SCXI-1328	A902DD
NI SCXI-1100	162E3B8	NI SCXI-1303	1B78B84
NI SCXI-1102	162E40B	NI SCXI-1303	161F800
NI SCXI-1102	162E400	NI SCXI-1303	162564D
NI SCXI-1102	162E421	NI SCXI-1303	162563F
NI SCXI-1102	162E419	NI SCXI-1303	1625634
NI SCXI-1102	162E3F8	NI SCXI-1303	162565F
NI SCXI-1102	162E3EB	NI SCXI-1303	161F801
FLUKE 1524	3491393	FLUKE 5615	983335
OMEGA ITS-90 RTD	-	LUNA ODiSI-B	14119087
NI SCXI-1001	19097FD	NI SCXI-1600	18FA585
NI SCXI-1102	18E9687	NI SCXI-1303	18F7583
NI SCXI-1102	189E51A	NI SCXI-1303	18F7585
NI SCXI-1102	19E969D	NI SCXI-1303	18F7580
LUNA ODiSI-A50	12026006	NI cDAQ 9171	1B27FDA
NI 9214	1877246		
NI cDAQ 9137	1B033FF	NI 9214	1ADEA6D

B.1 ODiSI-A50 Specifications

OPTICAL DISTRIBUTED SENSOR INTERROGATOR
(Models ODiSI A10 and A50)

The Luna ODiSI A (Optical Distributed Sensor Interrogator) delivers fully distributed strain and temperature measurements with sub-cm spatial resolution.

KEY FEATURES AND PRODUCT HIGHLIGHTS

- Reduce material costs with inexpensive optical fiber sensors
- Save time and labor by instrumenting many sensing locations using a single optical fiber
- Interrogate entire fiber and all sensing locations with a single scan
- Control sensor locations and gage lengths in software
- Measure temperature or strain with a single fiber
- Realize industry-leading measurement range and repeatability with extraordinary spatial resolution
  - Measurement ranges of ± 13,000 µStrain, -50 to 300 °C
  - Repeatability of ± 2 µStrain, ± 0.2 °C
  - Sub-centimeter spatial resolution
  - Maximum sensing length of 50 meters

The Luna **ODiSI A** saves test time and cost while adding an unprecedented spatial resolution to sensing measurements. Utilizing swept-wavelength interferometry, the ODiSI A simultaneously interrogates thousands of sensing locations along a single unaltered, inexpensive optical fiber. With a 50 meter maximum sensing length and sub-centimeter spatial resolution, the ODiSI A is the paramount tool for a variety of applications.

APPLICATIONS

- Load, fatigue, and mechanical testing
- Composite manufacturing and engineering
- Embedded sensing
- Temperature profile characterization
- Structural Health Monitoring
- Model and simulation validation

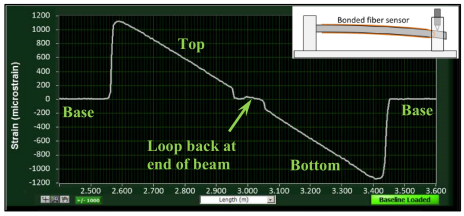

Demonstration of the ODiSI A recording distributed strain of an optical fiber bonded to the top and bottom surfaces of a cantilevered aluminum beam. Shown above with sensor spacing of 5 mm, each sensor with a 1-cm gage length.

www.lunainc.com
3157 State Street | Blacksburg, VA 24060
solutions@lunainc.com
Support phone: 1.866.586.2682

PARAMETER	SPECIFICATION		UNITS
Performance			
Model	**A10**	**A50**	
Maximum Sensing Length	10	50	meters
Acquisition Rate[1]	5	2.5	Hz
Minimum Sensor Spacing	0.4		mm
Minimum Gage Length[2]	1		mm
Wavelength Accuracy[3]	1.5		pm
Strain:			
Range	± 13,000		µStrain
Single-scan repeatability[1,4,5]	± 2		µStrain
Temperature:			
Range[6]	-50 to 300		°C
Single-scan repeatability[1,4,5]	± 0.2		°C
Physical			
Dimensions	14 x 12.5 x 6.75	(36 x 32 x 17)	in (cm)
Weight	17.5	(8)	lb (kg)
Power Consumption	50		W

1 For the default measurement range of ±1,250 µStrain or ±200 °C; see Page 3 for detailed timing information

2 Minimum gage length is achievable using the largest measurement range, having a single-scan repeatability of ±17.0 µStrain or ±2.0 °C

3 Accuracy maintained by an internal NIST-traceable HCN gas cell

4 Temperature and strain measurements are calculated from the spectral shift of scattered laser light. Using the default conversion coefficients of 1 GHz = 0.8 °C = 6.58 µStrain, the accuracy of temperature and strain are 0.15°C and 1.25 µStrain. [Othonos and K Kalli, Fiber Bragg Gratings (Artech House, Boston, 1999)].

5 For the default gage length of 1 cm

6 Based on material properties of the standard sensor: polyimide-coated, low-bend-loss optical fiber. For temperatures up to 800°C, contact Luna.

CLASS 1 LASER PRODUCT

©Luna Innovations Incorporated, Roanoke, VA
All rights reserved.

MEASUREMENT TIMING INFORMATION

In the figures below, the acquisition times versus measurement ranges are compared for the ODiSI A10 and A50 instruments. A single acquisition acquires all the data necessary to calculate strain or temperature anywhere along the fiber sensor.

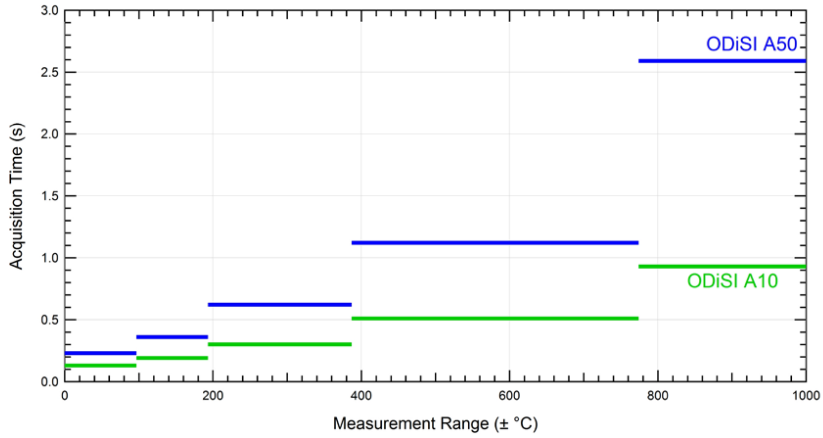

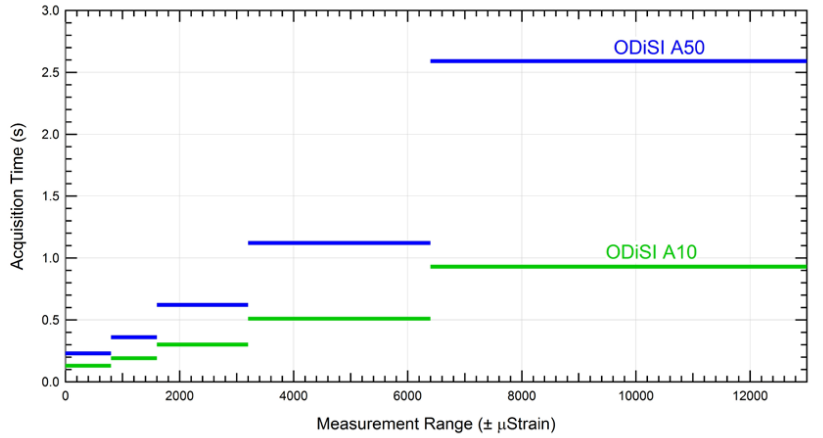

©Luna Innovations Incorporated, Roanoke, VA
All rights reserved.

B.2 ODiSI-B Specifications

LUNA

DEFYING IMPOSSIBLE

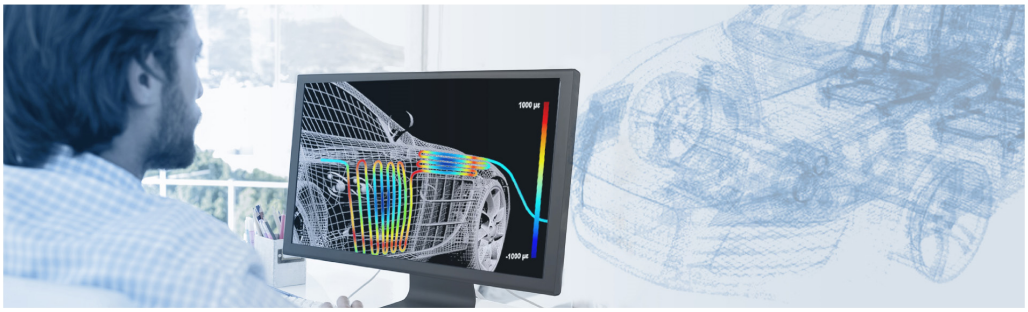

KEY ADVANTAGES

- High definition strain and temperature measurement system for unprecedented visibility into a design's performance
- Low profile and flexible sensor can be embedded within composite structures and points
- Corrosion resistant, dielectric and immune to EMI/RFI
- An economical alternative to replace traditional point sensing systems
- No degradation of measurement after high cycle count fatigue test

PRODUCT HIGHLIGHTS

- Sensor lengths up to 20 meters and gage lengths as low as 1.3 mm
- Two sensing options: High-Definition as standard and High-Speed Continuous Fiber Gratings (CFG) option for greater dynamic capability
- User selectable modes allow configuration of sensor length, resolution, and acquisition rate

ODiSI-B 5.0

Optical Distributed Sensor Interrogator

The ODiSI is a 21st century measurement system specifically designed to address the test challenges of 21st century advanced materials and systems.

The ODiSI provides more than 1000 strain or temperature measurements per meter of a single high definition fiber sensor. The high definition data can fully map the contour of strain or temperature for a structure under test.

The sensor is flexible, low profile, requires no electrical source, and can be bonded to sharply curved surfaces, embedded within structures, or mounted directly to electrical surfaces.

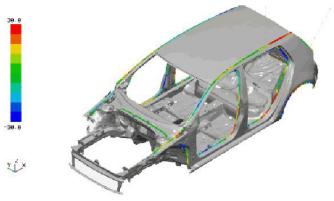

An automotive frame is instrumented with fiber and then tested under load. Test data is then superimposed on the CAD model.

www.lunainc.com | 3155 State Street, Blacksburg VA | Support phone: 1.866.586.2682 | solutions@lunainc.com

ODiSI-B 5.0

PARAMETER	SPECIFICATION								UNITS
Mode of Operation[1]	**100 Hz**		**250 Hz**		**23.8 Hz**		**50 Hz**		
Sensor Type	**HD**	**HS**	**HD**	**HS**	**HD**	**HS**	**HD**	**HS**	
Sensor Configurations									
Maximum Sensor Length	10	5	2	-	10	5	20	-	m
Gage Length	5.2	5.2	5.2	-	1.3	1.3	5.2	-	mm
Gage Pitch[2]	2.6	2.6	2.6	-	0.65	0.65	2.6	-	mm
Measurement Performance - Strain									
Range[3]	±10000	±1400	±10000	-	±10000	±7500	±10000	-	με
Resolution	< 1	< 1	< 1	-	< 1	< 1	< 1	-	με
Accuracy[4]	±30	±15	±30	-	±25	±35	±25	-	με
Repeatability at zero strain[5]	< ±5	< ±5	< ±10	-	< ±20	< ±10	< ±5	-	με
Repeatability across full strain range[6]	±0.15	±1.0	±0.15		±0.55	±0.35	±0.10		%
Dynamic Loading Rate HD (Based on 2m sensor legnth at ±1000με)[7]	1.8	-	4	-	0.4	-	0.8	-	Hz
Dynamic Loading Rate HS (based on 2m sensor length @ ± 600με)[8]	-	> 10	-		-	> 10	-		Hz
Measurement Performance - Temperature									
Maximum Temperature[9] (Based on standard sensor. Custom sensors available upon request.)	220	200	220	-	220	200	220	-	°C
Minimum Temperature (Based on standard sensor. Custom sensors available upon request.)	-40	-40	-40	-	-40	-40	-40	-	°C
Resolution	< 0.1	-	< 0.1	-	< 0.1	-	< 0.1	-	°C
Accuracy (consult factory)	-	-	-	-	-	-	-	-	°C
Repeatability	±0.01	-	±0.01	-	±0.06	-	±0.01	-	%
Data Acquisition / Processing Rate									
Data Acquisition Rate[10]	100	100	250	-	23.8	23.8	50	-	Hz
Data Processing Rate[11]	5	100	22	-	1.25	23.8	2.5	-	Hz
Physical & Environment	**ODiSI-B**				**PC Controller**				
Standoff	50				-				m
Dimensions	14.42 (36.6) x 13.60 (34.5) x 6.55 (16.6)				11.4(29) x 3.7(9.3) x 12.3(31.2)				In (cm)
Weight	17.1 (7.8)				11.7(5.3)				Lb (Kg)
Power Consumption	45				255				W
Operating Temperature Range	10 - 35				5 - 35				°C
Storage Temperature Range	0 - 40				-40 - 65				°C
Relative Humidity (non-condensing)	< 80 non-condensing				5 - 95 non-condensing				%RH
Laser	Class 1 Laser				-				

APPLICATION NOTES

1. Base configuration includes one mode of operation. Additional modes are upgrade options.
2. Gage pitch refers to distance between centers of consecutive gages.
3. Based on an effective spectral range of +/-12000 pm, and practical limitations of fused silica sensor fibers.
4. Accuracy reflects ODiSI measurements compared to NIST traceable extensiometer meaurements. Data based on average of 150 scans at each of seven increments of strain, from 0 to maximum strain.
5. Repeatability at zero strain refers to offset from zero with no strain applied. NO filtering is applied.
6. Repeatability across strain range refers to average repeatability over full strain range. Repeatability is measured and reflects 2σ standard deviation from the mean with sample size of 150 scans. NO filtering is applied.
7. HD dynamic performance based on 2 meter HD sensor bonded to coupon and tested in load machine programmed for range of amplitude vs oscillating frequency. Data shown is oscillating frequency limit for ±1000 με amplitude. Limitation determined by HD sensing.
8. HS dynamic performance based on 2 meter HS CFG sensor bonded to coupon and tested in load machine programmed for range of amplitude vs oscillating frequency. Data shown is oscillating frequency limit for ±600 με amplitude. Limitation shown is determined by load machine amplitude vs frequency capability. Expected dynamic performance is ½ sampling frequency depending on strain amplitude.
9. Based on material properties of standard sensor construction. For extended temperature ranges consult factory.
10. Data acquisition rate refers to the rate at which the underlying optical data supporting strain and temperature measurements is acquired.
11. Data processing rate refers to the rate at which the conversion of optical data to strain or temperature measurements occurs and can be displayed or logged.

APPENDIX C

PANEL THERMOCOUPLE CALIBRATION POINTS

C.1 Water Probe Thermocouple Calibration Points

Sensor	*Point 1 (°C)*	*Point 2 (°C)*		
Reference	19.793	99.685	99.730	99.647
R1WP1	20.449	-	-	99.796
R1WP2	20.763	-	-	99.755
R1WP3	20.816	-	-	100.187
R1WP4	20.281	101.016	-	-
R1WP5	20.043	100.077	-	-
R2WP1	20.626	-	-	100.170
R2WP2	20.555	-	-	99.977
R2WP3	20.655	-	-	99.817
R2WP4	20.399	100.467	-	-
R2WP5	20.852	100.634	-	-
R3WP1	20.125	-	-	99.400
R3WP2	20.646	-	-	99.602
R3WP3	20.882	-	-	99.146
R3WP4	20.521	100.494	-	-
R3WP5	20.537	100.885	-	-

Sensor	*Point 1 (°C)*		*Point 2 (°C)*	
R4WP1	20.707	-	-	99.958
R4WP2	20.729	-	-	100.108
R4WP3	20.752	100.745	-	-
R4WP4	20.560	100.471	-	-
R4WP5	20.625	101.455	-	-
R5WP1	20.467	-	-	100.117
R5WP2	20.833	-	-	100.426
R5WP3	20.505	-	-	99.943
R5WP4	20.522	100.314	-	-
R5WP5	20.489	100.226	-	-
R6WP1	20.915	-	100.056	-
R6WP2	20.976	-	100.159	-
R6WP3	20.863	-	100.046	-
R6WP4	21.040	-	100.076	-
R6WP5	20.707	-	100.998	-
R7WP1	20.861	-	100.250	-
R7WP2	20.752	-	99.825	-
R7WP3	20.494	-	99.769	-
R7WP4	20.283	-	100.700	-
R7WP5	20.443	-	100.740	-

Sensor	*Point 1 (°C)*	*Point 2 (°C)*
R8WP1	20.873 -	100.118 -
R8WP2	20.605 -	99.810 -
R8WP3	20.567 -	100.101 -
R8WP4	20.568 -	100.323 -
R8WP5	20.339 -	99.968 -
R9WP1	20.679 -	100.204 -
R9WP2	20.841 -	99.998 -
R9WP3	20.546 -	100.181 -
R9WP4	20.455 -	100.866 -
R9WP5	20.331 -	100.257 -

C.2 Riser Wall Thermocouple Calibration Points

Sensor	*Point 1 (°C)*	*Point 2 (°C)*	*Sensor*	*Point 1 (°C)*	*Point 2 (°C)*
Ref.	19.793	99.690			
R1P1	20.220	100.419	R2P1	20.287	100.186
R1P2	20.295	99.703	R2P2	20.286	100.253
R1P3	20.572	101.280	R2P3	20.329	100.069
R1P4	20.596	101.275	R2P4	20.235	100.660
R1P5	20.414	99.344	R2P5	19.738	100.566

Sensor	*Point 1 (°C)*	*Point 2 (°C)*	*Sensor*	*Point 1 (°C)*	*Point 2 (°C)*
R3P1	20.328	97.943	R7P1	20.020	100.681
R3P2	20.113	100.533	R7P2	20.102	100.730
R3P3	19.939	99.255	R7P3	19.991	99.777
R3P4	20.259	100.579	R7P4	20.108	100.904
R3P5	19.673	100.097	R7P5	19.989	100.762
R4P1	19.793	100.259	R8P1	19.951	100.624
R4P2	20.065	100.475	R8P2	19.491	100.216
R4P3	19.986	100.623	R8P3	19.893	102.920
R4P4	20.036	100.337	R8P4	20.268	100.925
R4P5	20.055	100.698	R8P5	20.007	100.841
R5P1	20.181	100.263	R9P1	20.237	99.969
R5P2	20.000	100.413	R9P2	19.963	100.768
R5P3	20.111	100.475	R9P3	20.247	100.099
R5P4	20.113	100.606	R9P4	20.036	99.920
R5P5	20.107	100.357	R9P5	20.065	101.078
R6P1	19.874	100.587			
R6P2	20.502	101.144			
R6P3	19.894	100.532			
R6P4	19.931	99.546			
R6P5	20.003	100.933			

C.3 Fin Wall Thermocouple Calibration Points

Sensor	*Point 1 (°C)*	*Point 2 (°C)*	*Sensor*	*Point 1 (°C)*	*Point 2 (°C)*
Ref.	19.793	99.690			
F1P1	20.377	100.530	F5P1	20.336	100.929
F1P2	20.388	100.775	F5P2	20.566	101.185
F1P3	20.458	101.000	F5P3	20.253	99.719
F1P4	20.346	100.840	F5P4	20.076	100.884
F1P5	20.617	101.378	F5P5	20.626	101.463
F2P1	20.433	100.911	F6P1	20.072	100.746
F2P2	20.305	100.435	F6P2	19.890	100.594
F2P3	20.575	101.240	F6P3	20.348	101.133
F2P4	20.413	100.888	F6P4	20.454	100.170
F2P5	20.244	99.910	F6P5	20.535	101.207
F3P1	20.025	99.572	F7P1	19.940	100.805
F3P2	20.273	100.820	F7P2	19.744	100.528
F3P3	20.462	101.048	F7P3	20.620	100.401
F3P4	20.741	101.080	F7P4	21.117	100.677
F3P5	20.669	101.181	F7P5	20.773	101.350
F4P1	20.025	99.601	F8P1	20.440	100.531
F4P2	20.022	100.492	F8P2	19.956	100.991
F4P3	20.746	101.197	F8P3	20.730	100.424
F4P4	20.891	101.413	F8P4	20.734	101.476
F4P5	20.323	100.828	F8P5	20.764	101.548

APPENDIX D

ADDITIONAL COMPARISONS FROM TWO-PHASE HEATED PIPE TESTING

D.1 Steady-State Boiling Data

These plots contain data obtained from steady boiling at heater power levels of 25 - 45%. Each row corresponds to an increase in heater power level of 5%. Sheathed DTS configurations are in the left column, and exposed DTS are in the right.

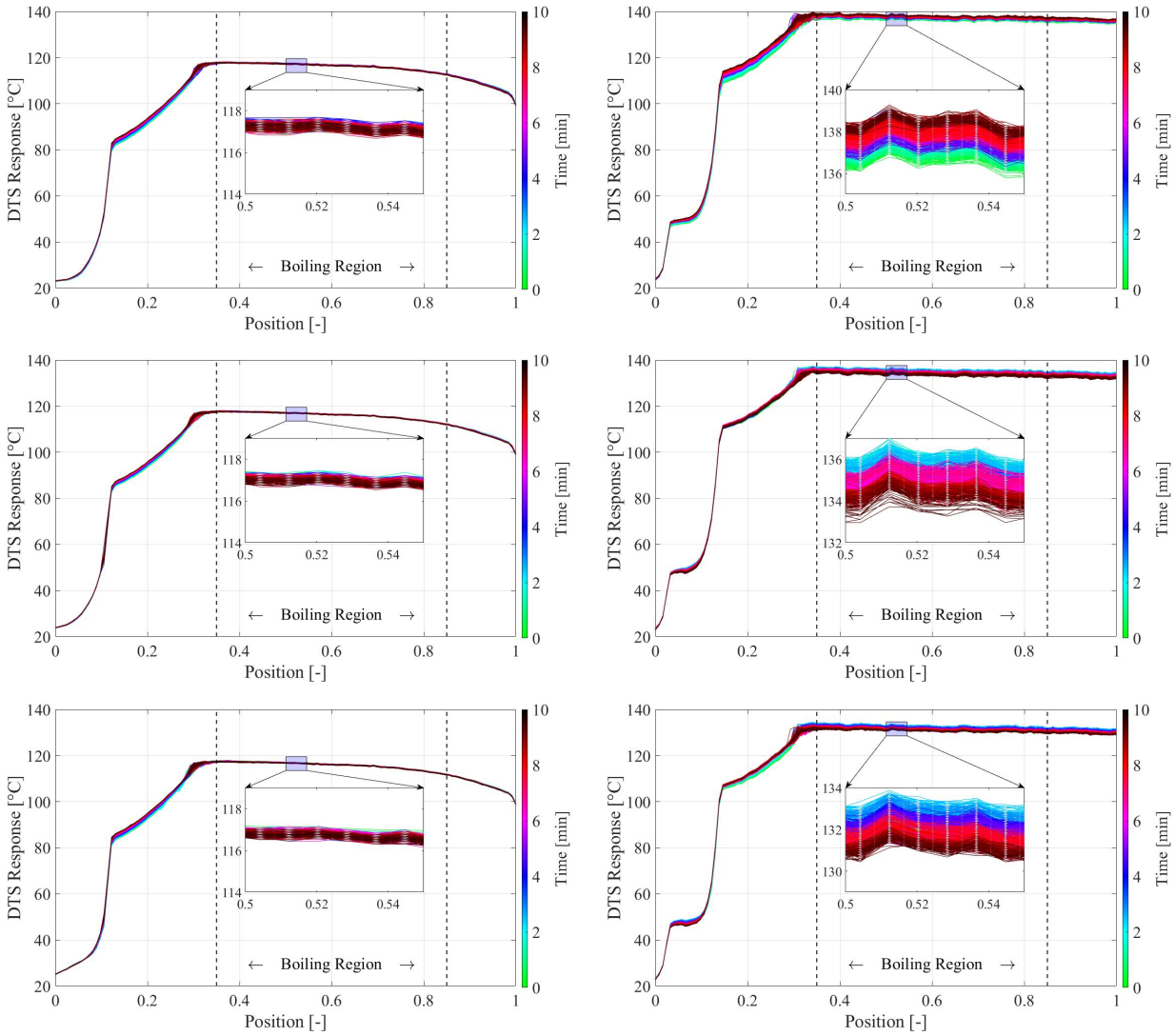

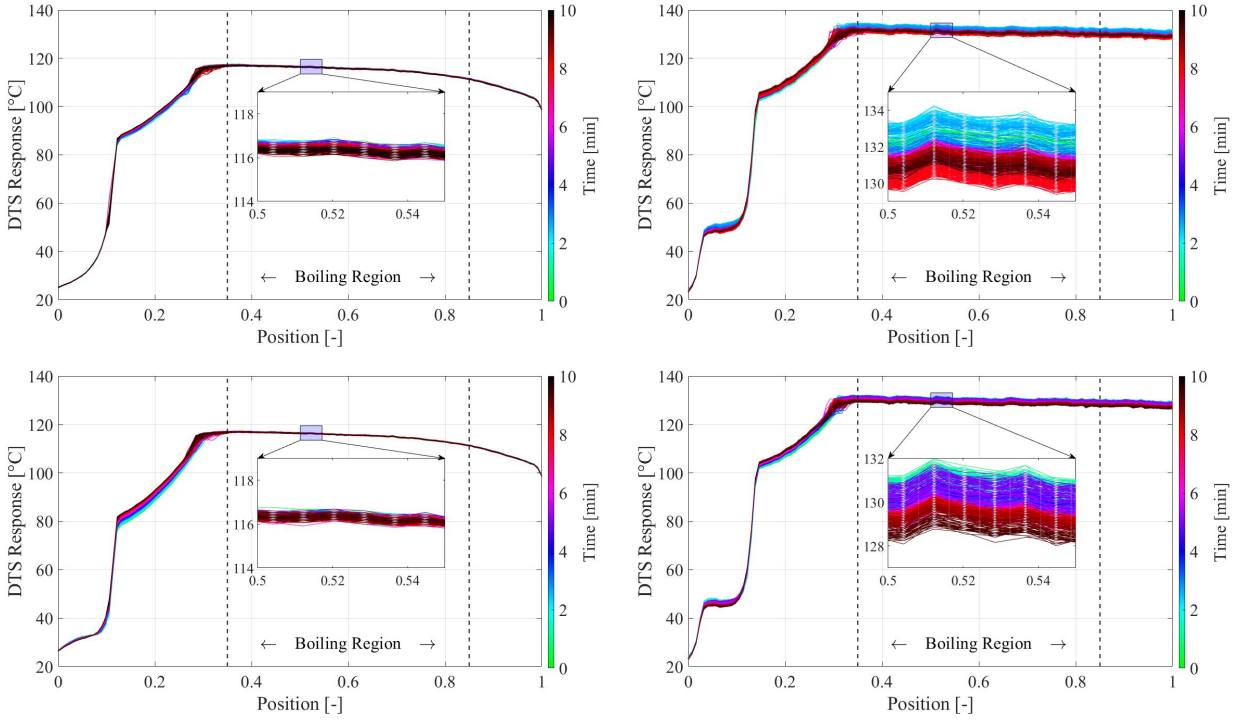
DTS Response [°C]
Position [-]
Time [min]
← Boiling Region →